THESIS FOR THE DEGREE OF DOCTOR OF PHILOSOPHY IN
MATERIALS SCIENCE

Multi-Scale Characterization of White Layer Evolution in Martensitic Steels after Hard Turning

SAHITH KOKKIRALA

Department of Mechanical Engineering
CHALMERS UNIVERSITY OF TECHNOLOGY
Gothenburg, Sweden, 2026

Multi-Scale Characterization of White Layer Evolution in Martensitic Steels after Hard Turning

SAHITH KOKKIRALA

ISBN: 978-91-8103-340-3

Doktorsavhandlingar vid Chalmers tekniska högskola
Ny serie nr 5797
ISSN 0346-718X
https://doi.org/10.63959/chalmers.dt/5797

Department of Mechanical Engineering
Chalmers University of Technology
SE-412 96 Gothenburg, Sweden
Telephone + 46 (0)31-772 1000

Cover: Bright field-STEM images together with transmission Kikuchi diffraction (TKD) inverse pole figure (IPF) orientation maps of mechanically and thermally induced white layers, highlighting the formation of nanocrystalline (NC) grains through different mechanisms in Hybrid 60 steel.

Chalmers Digitaltryck
Gothenburg, Sweden 2026

Dedicated to my fiancée, Sophia;
my mom, Srilatha; my father, Sanjeeva Rao; and my brother, Rohith.

Multi-Scale Characterization of White Layer Evolution in Martensitic Steels after Hard Turning

SAHITH KOKKIRALA
Department of Mechanical Engineering
Chalmers University of Technology

Abstract

The advancement in machining processes demands that components exhibit superior surface integrity and functional performance. Hard turning is an efficient machining process that requires precise process control, especially with hardened steels, to achieve the desired surface integrity. However, the intense thermo-mechanical interactions between the workpiece and the cutting tool often lead to the formation of a white layer (WL) on the hard-turned surface, which typically extends from a few hundred nanometers to few micrometers below the surface. WLs are microstructural alterations characterized by nanocrystalline (NC) grains, appearing featureless and white in the light optical microscopy. Based on established literature, often WLs are detrimental because they consist of brittle, untempered martensite with tensile residual stresses, leading to premature component failure. These typically refers to thermally induced WLs (T-WLs), which form through continuous dynamic recrystallization (CDRX) and reverse martensitic transformation and are often accompanied by the formation of a softer dark layer. However, if the process parameters are carefully controlled, a fundamentally different type of WL is formed below the austenitization temperature, known as mechanically induced white layer (M-WL), which exhibits beneficial compressive residual stresses without the presence of a dark layer. These properties make M-WLs a promising process-induced NC surface for demanding engineering applications. Despite its potential, a detailed understanding of the influence of process parameters, tool geometry, initial microstructure on the formation of M-WL with improved surface integrity is currently lacking. In particular, the underlying mechanisms that control microstructure development in M-WL remain unclear.

This thesis investigates the formation and properties of M-WLs and compares them with T-WLs in AISI 52100 and Hybrid 60 steels after hard turning using a multi-scale characterization approach. The results show that the microstructure development of the M-WL in AISI 52100 steel is primarily initiated by grain subdivision process that lead to lamellar grain formation from the initial lath martensite. This is followed by a mechanically assisted triple junction motion, a dynamic recovery mechanism that leads to the formation of NC grains. Furthermore, compared to T-WL, the M-WL exhibited higher compressive residual stresses, lower surface roughness, and improved nanohardness. A similar M-WL mechanism was observed in Hybrid 60 steel, but in this case, it was associated with the dissolution of nanoprecipitates. Nevertheless, this led to an increase in nanohardness due to enhanced grain boundary, dislocation, and solid solution strengthening. Hence, the inherent ability of hard turning to generate severe plastic strain below the phase transformation temperature enables the formation of a tailored microstructure. Achieving this within a single, cost-efficient manufacturing step offers a significant advantage for the production of high-performance surfaces.

Keywords: hard turning, martensite, AISI 52100, Hybrid 60, white layer, nanocrystalline grains, steel, microscopy

Preface

The doctoral thesis was based on the work performed at the Division of Materials and Manufacture, Department of Mechanical Engineering, Chalmers University of Technology, in the period between October 2021 and February 2026. The work has been carried out under the supervision of Professor Uta Klement and Dr. Seyed B. Hosseini (AB SKF) with Professor Peter Krajnik acting as the examiner. This research is part of the projects "*Flexible and sustainable production of high-performance rolling bearings (Turn2Flex)*" under the production 2030 strategic innovation program, funded by the Sweden's Innovation Agency (VINNOVA) (Grant number: 2021-01274) and "*Ultrahigh-strength surfaces on novel corrosion resistant hybrid steel"* funded by the Swedish Research Council (Grant number: 2023-04410). Parts of the work presented in this doctoral thesis have been previously published in a licentiate thesis by the same author.

List of appended papers:

Paper I ***Effect of cutting parameters on the generated surface integrity of hard-turned martensitic AISI 52100 bearing steel***
S. Kokkirala, J. Holmberg, U. Klement, R. Lundstrom, H. Iwasaki,
S. B. Hosseini
Procedia CIRP, Vol. 115, 10th CIRP Global Web Conference – Material Aspects of Manufacturing Processes, (2022), pp: 154-159
https://doi.org/10.1016/j.procir.2022.10.066

Paper II ***The role of retained austenite on the formation of the nanostructured hard-turned induced white layer in AISI 52100 bearing steel***
S. Kokkirala, K. Osman, J. Holmberg, S. Kimming, H. Iwasaki, U. Klement,
S.B. Hosseini
Procedia CIRP, Vol. 123, 7th CIRP Conference on Surface Integrity, (2024), pp:292-297
https://doi.org/10.1016/j.procir.2024.05.052

Paper III ***Understanding the development of mechanically and thermally induced white layers in AISI 52100 steel during hard turning: Process-microstructure-property relationship***
S. Kokkirala, U. Klement, J. Holmberg, H. Iwasaki, J. M. B. Bermejo,
S. Kimming, S. B. Hosseini
Journal of Materials Research and Technology, Vol. 38, (2025), pp: 1185-1197
https://doi.org/10.1016/j.jmrt.2025.07.293

Paper IV ***Revealing grain subdivision initiated nanocrystalline white layer evolution in AISI 52100 steel via hard turning using transmission Kikuchi diffraction pattern matching***
S. Kokkirala, S. B. Hosseini, U. Klement
Submitted for journal publication

Paper V ***Nanocrystalline microstructure evolution and behavior of nanoprecipitates in dual-hardening Hybrid 60 steel under high strain rate deformation induced by hard turning***
S. Kokkirala, S. Jakob, M. Thuvander, S. B. Hosseini, U. Klement
Submitted for journal publication

Contribution to appended papers:

My contributions to the appended papers are listed below and overall, the work was planned in collaboration with the supervisors.

Paper I The author carried out the X-ray diffraction measurements, and LOM, SEM imaging. The hard turning tests were performed by Michael Spahr at Sumitomo Electric Hardmetal Corp., and the surface roughness measurements were carried out by Dr. Jonas Holmberg at RISE AB. The author analyzed the data and wrote the paper in collaboration with the co-authors.

Paper II The work was executed by Karim Osman as his MSc thesis work under the author's supervision. The hard turning tests were carried out at AB SKF, and the SEM imaging was performed by the author. The author analyzed the data and wrote the paper in collaboration with the co-authors.

Paper III The author performed the X-ray diffraction measurements, the sample preparation by FIB-SEM, and the LOM, SEM, and STEM-in-SEM imaging. The hard turning tests were performed by Michael Spahr at Sumitomo Electric Hardmetal Corp. and surface roughness measurements were carried out by Dr. Jonas Holmberg at RISE AB. Nanoindentation was performed at Micro Materials Ltd, UK, and the initial test parameters were determined collaboratively by Juan Manuel Bello Bermejo (Lund University) and the author. The author analyzed the data and wrote the paper in collaboration with the co-authors.

Paper IV The author performed the LOM, SEM, EBSD, STEM-in-SEM and TKD measurements and prepared samples using FIB-SEM. The hard turning tests were performed by Michael Spahr at Sumitomo Electric Hardmetal Corp. The author analyzed the data and wrote the paper in collaboration with the co-authors.

Paper V The author performed the sample preparation by FIB-SEM and carried out the SEM, EBSD, STEM-in-SEM, TKD, and nanoindentation measurements. The TEM investigations were carried out with the support of Dr. Stefan Gustafsson. The APT measurements and data analysis were performed by Dr. Severin Jakob, with the author contributing to APT sample preparation using FIB-SEM in collaboration with Dr. Severin Jakob. The hard turning tests were performed by Michael Spahr at Sumitomo Electric Hardmetal Corp. The author analyzed the data and wrote the paper in collaboration with the co-authors.

Table of contents

Nomenclature

List of symbols

Y	Chamfer angle (°)
A_{c1}	Critical transformation temperature (°C)
a_p	Depth of cut (mm)
f	Feed rate (mm/rev)
M_s	Martensite start temperature (°C)
M_f	Martensite finish temperature (°C)
P	Coolant pressure (bar)
R_a	1D - Arithmetic mean value of the surface roughness (µm)
V_c	Cutting speed (m/min)
VB	Tool flank wear (mm)

List of abbreviations

APT	Atom probe tomography
ARB	Accumulative roll bonding
ASB	Adiabatic shear bands
BCC	Body centered cubic
BCT	Body centered tetragonal
BF	Bright field
BSE	Backscattered electron
CDRX	Continuous dynamic recrystallization
CSM	Continuous stiffness measurement
DDRX	Discontinuous dynamic recrystallization
DL	Dark layer
DRV	Dynamic recovery
DRX	Dynamic recrystallization
EBSD	Electron backscattered diffraction
ECAP	Equal-channel angular pressing
FCC	Face centered cubic
FEG	Field emission gun
FIB	Focused ion beam
GIS	Gas injection system
GNB	Geometrically necessary boundaries
HAGBs	High-angle grain boundaries
HPT	High-pressure torsion
IDB	Incidental dislocation boundaries
IPF	Inverse pole figure
LAGBs	Low-angle grain boundaries
LOM	Light optical microscopy
M-WL	Mechanically induced white layer
NC	Nanocrystalline

OPS	Oxide polishing suspension
PCBN	Polycrystalline cubic boron nitride
RA	Retained austenite
SE	Secondary electron
SEM	Scanning electron microscopy
SFE	Stacking fault energy
SPD	Severe plastic deformation
STEM	Scanning transmission electron microscopy
TEM	Transmission electron microscopy
TKD	Transmission Kikuchi diffraction
TMIs	Thermo-mechanical interactions
T-WL	Thermally induced white layer
UFG	Ultrafine-grained
VSI	Vertical scanning interferometry
WL	White layer
XRD	X-ray diffraction

CHAPTER 1

Introduction

1.1 Motivation

High-quality steel components with superior dimensional accuracy and surface integrity are essential for achieving reliable functional performance in demanding applications. The key value-adding step to achieve precise component specifications is machining, a subtractive process that removes material via the shearing action of a cutting tool. Continuous advancements in machining knowledge are driven by the ongoing demand for better component performance, reliability, and durability [1]. Machining of hardened steels is increasingly important due to their extensive use, for example in the bearing and automotive sectors. While traditional final finishing relied on grinding and honing, hard turning has emerged as a competitive alternative employing polycrystalline cubic boron nitride (PCBN) cutting tools. Hard turning offers reduced energy consumption, greater process flexibility, and the capability to machine complex geometries, aligning perfectly with the push for efficient and sustainable manufacturing motivated by economic profit and global environmental regulations [2,3].

During hard turning, the thermo-mechanical interaction between the tool and the workpiece can be extremely intense. This interaction involves intense plastic strains, high strain rates ($\sim 10^4$-10^5 s^{-1}), and elevated temperatures, within short intervals often occurring under adiabatic conditions [4,5]. These extreme thermo-mechanical loads accelerate tool flank wear, limiting the wider implementation of hard turning and leading to severe deterioration of the component's surface integrity. Consequently, production costs increase due to more frequent tool changes and higher scrap rates, affecting the machining efficiency. Furthermore, these severe conditions including rapid tool degradation can cause significant microstructural alterations on the machined surface, leading to the formation of a white layer (WL) [6–9]. This layer appears featureless and white in the light optical microscopy (LOM), characterized by a nanocrystalline (NC) grain structure [7]. Prior studies have extensively examined the mechanisms behind machining induced WLs in alloys such as AISI 52100 tempered martensitic steel [6,10], Inconel 718 [11], Ti-6Al-4V [12], and copper [13]. Focusing on hardened steels with a tempered martensitic microstructure, Hosseini et al. [14] reported the formation of two distinct types of WL resulting after hard turning. These were the mechanically induced WL (M-WL), generated below the austenitization temperature and associated with beneficial compressive residual stresses, and thermally induced WL (T-WL), formed above the austenitization temperature and typically characterized by detrimental tensile residual stresses, often accompanied by a soft dark layer. Despite these differences, both types of WLs are significantly harder than the bulk material [7].

Historically, the NC microstructure of the WL has been regarded as purely detrimental as it is often associated with brittle untempered martensite that can lead to premature failure [15,16]. However, understanding the grain refinement mechanism leading to nanostructured materials has challenged this conventional view. Although the concept of severe plastic deformation (SPD) dates back more than 2,700 years, the fundamental scientific understanding emerged in the 20th century [17]. In the 1930s, Percy W. Bridgman provided the first documented evidence that applying large plastic strains could successfully refine grains down to the nanometer scale, a technique now known as high-pressure torsion (HPT) [18,19]. Following this principle, and particularly since the early 1990s, significant research has focused on producing NC (<100 nm) and ultrafine-grained (100 nm - 1 μm) microstructures through SPD due to their superior mechanical and functional properties [17]. Since then, numerous specialized SPD techniques, such as accumulative roll bonding (ARB) [20] and equal-channel angular pressing (ECAP) [21], have been extensively studied for producing bulk nanostructured materials (BNMs). Building upon the enhanced properties achieved from BNMs, research quickly led to the development of surface-SPD techniques such as ultrasonic surface peening (USP) and surface mechanical attrition treatment (SMAT) [22,23]. They have gained prominence for enhancing wear resistance while preserving bulk toughness by confining the grain refinement to the surface layer, and thereby generating a gradient microstructure.

Machining offers a unique advantage in this context as it has the inherent potential of generating large plastic strain in a single-pass. This capability means that hard turning during final finishing processes can directly lead to the formation of process-induced NC grains on the workpiece surface, commonly known as WL. Depending on the specific formation mechanism, the WL can be leveraged as an advantage, enabling the creation of functional, high-performance surfaces within a cost-efficient manufacturing step. The present thesis therefore investigates the possibility of tailoring the M-WL formation to achieve a single-pass, large plastic strain deformation that consistently generates NC grains with beneficial surface compressive residual stresses. A key focus of this work is the post-mortem analysis of WL evolution and its properties in martensitic steels using multi-scale characterization techniques. This is critical because the underlying mechanisms that govern M-WL formation are still not fully understood, partly due to the difficulty in resolving the severely strained NC grains in these materials.

1.2 Aim of the study

The main objective of the study is to investigate the development of M-WL and to compare it with T-WL in two martensitic steels that has undergone hard turning: AISI 52100 (a conventional steel grade) and Hybrid 60 (a newly developed steel grade). Insights from this multi-scale characterization are essential for expanding the fundamental knowledge of WL formation. This knowledge will guide the optimization of cutting conditions during the final finishing process by hard turning. Specifically, the findings will help to achieve the desired M-WLs, beneficial for surface integrity, and provide a detailed understanding of the gradient microstructure behavior from the bulk to the NC microstructure. This doctoral thesis project is designed to investigate the following research questions:

Research questions (RQs):

- ***RQ1: What influence do process parameters, the geometry of the cutting tool, and the initial retained austenite content have on the formation of WLs in AISI 52100 steel after hard turning?***

The fundamental objective of hard turning AISI 52100 martensitic steel is to achieve the required functional surface integrity by improving surface roughness, enhancing compressive residual stresses, and promoting beneficial M-WL formation. Achieving these outcomes requires a systematic understanding of how process parameters, tool geometry and tool wear influence WL development. Although most studies report that WLs typically form as a result of tool flank wear (*VB*) progression, the possibility of intentionally generating M-WL using fresh inserts through optimized cutting conditions remains largely unexplored and required detailed investigation. At the same time, since flank wear inevitably progresses during machining, this research also examines how *VB* of ~0.2 mm can be effectively utilized to maintain or even improve surface integrity. Ultimately, the research seeks to establish a detailed process-structure-property relationship governing both M-WL and T-WL formation. Since the AISI 52100 steel is also subjected to different heat treatment processes, which leads to different retained austenite contents, the role of this retained austenite in WL formation remains unclear and requires further investigation (***Paper I, Paper II and Paper III***).

- ***RQ2: What is the governing formation mechanism of M-WL in AISI 52100 steel?***

Despite the promising characteristics of M-WL, comprehensive studies detailing its underlying mechanisms of extreme grain refinement leading to NC microstructure remain insufficiently understood. This investigation will systematically compare the M-WL evolution with the characteristics of the well-established T-WL. Addressing this requires overcoming significant technical challenges related to specialized specimen preparation and the use of advanced microscopy techniques necessary to resolve the severely strained NC grains. Overcoming these limitations is essential for elucidating the gradient microstructure that transitions from the unaffected bulk region to the machined surface in AISI 52100 martensitic steel (***Paper III and Paper IV***).

- ***RQ3: Does hard turning on Hybrid 60 dual-hardening steel lead to WL formation and how does this affect the nanoprecipitates?***

Hybrid 60 is a dual-hardening steel strengthened by Cr-rich secondary carbides and NiAl intermetallic precipitates. Building on the understanding of WL formation mechanisms established for AISI 52100 steel, this study seeks to investigate how WLs evolve in Hybrid 60, a material for which hard turning has not yet been explored. A central question is whether WLs can be generated at all in this alloy under hard turning conditions. Additionally, this investigation is crucial for understanding the unexplored thermo-mechanical interaction with the nanometer-sized Cr-rich secondary carbides and NiAl intermetallic precipitates that occurs under the high strain rate deformation inherent to the hard turning process (***Paper V***).

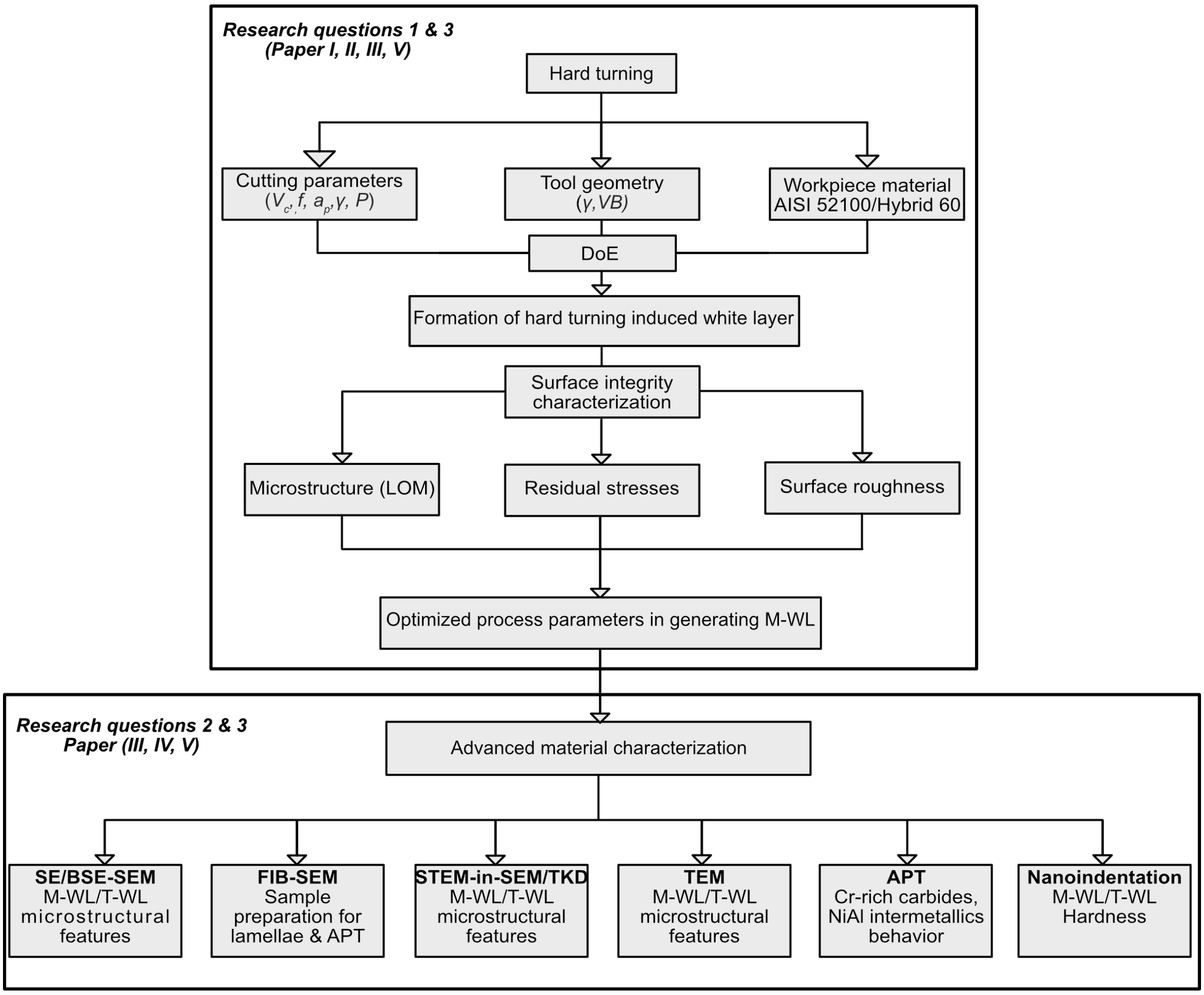

Fig.1: Schematic of the research approach used in this thesis.

CHAPTER 2

Martensitic Steels

Steel, an alloy of iron (Fe) and carbon (C) with C <2.1 wt.%, is the most important man-made engineering material. In addition to carbon, the inclusion of various alloying elements allows its properties to be strategically tailored for applications ranging from kitchen cutlery to aerospace components. To meet the demanding performance requirements of critical applications, such as bearings, steel components are subjected to hardening, followed by tempering heat treatments, producing hardened steels. The resulting tempered martensite phase provides exceptional high strength and superior wear resistance to withstand high rolling contact fatigue loads [24]. This chapter begins with an overview of martensite, tempering stages, and dual-hardening behavior, followed by an introduction to the materials under investigation. The work presented in this thesis focuses on two martensitic steel grades: AISI 52100 (a conventional steel grade) and Hybrid 60 (a newly developed steel grade).

2.1 Martensite

The term martensite was introduced in 1895 in honor of the German metallurgist Adolf Martens, originally describing the hard microconstituent formed in quenched steels [25]. In modern materials science, the definition has expanded to describe a broader class of diffusionless transformations that occur during rapid cooling or deformation in ferrous and non-ferrous alloys, as well as in certain ceramics [26]. In steels, martensite (α') is a metastable phase formed from austenite (γ) and consists of a supersaturated solid solution of carbon in iron. The phase transformation occurs via diffusionless, lattice-distortion, and shear dominance by nucleation and growth mechanism [24]. As atomic diffusion is suppressed, the chemical composition of the parent austenite and the resulting martensite remains unchanged. This characteristic behaviour places the transformation firmly within the category of solid-state diffusionless phase transformations, commonly referred to as martensitic transformations. The formation of martensite requires cooling from the austenitic state at a rate sufficiently rapid to prevent other solid-state transformations such as ferrite and pearlite [27,28]. The minimum cooling rate necessary to achieve this, known as the critical cooling rate, is strongly dependent on alloy composition, which governs the hardenability of the steel. While conventional quenched steels rely on high cooling rates, the addition of substantial amounts of diffusion-inhibiting alloying elements can significantly reduce the critical cooling rate, enabling martensitic transformation to occur even during air cooling [29,30]. When diffusion is effectively suppressed, carbon atoms become trapped within the octahedral interstitial sites of the face centered cubic (FCC) austenite lattice. This entrapment drives the transformation to a body centered tetragonal (BCT) martensitic lattice via a coordinated shear process, in which atomic displacements are smaller than the interatomic spacing. Due to the lower solubility of carbon in the BCT structure compared with the FCC structure, martensite becomes highly supersaturated with carbon, resulting in significant lattice distortion. The degree of tetragonality in martensite increases with carbon content and is commonly expressed by the ratio of the lattice parameters c/a, as shown in Equation (1) [27].

$$\frac{c}{a} = 1 + 0.045 * wt.\%\,C \qquad (1)$$

where c and a represent the lattice parameters of the BCT unit cell.

Martensitic transformation is both diffusionless and athermal, meaning that the extent of transformation is governed primarily by the degree of undercooling rather than time. The temperature at which martensite first forms is known as the martensite start temperature (M_s), while the martensite finish temperature (M_f) denotes the point at which the transformation is complete. Increasing carbon content lowers both M_s and M_f, as carbon stabilizes austenite and increases its resistance to shear. As a result, complete martensitic transformation may not occur at room temperature in high-carbon steels, leading to the formation of retained austenite (RA) [24].

Martensite in steels generally appears in two distinct morphologies: lath martensite and plate martensite, with the dominant form largely determined by carbon content. Lath martensite typically forms in steels containing ≤ 0.6 wt.% C, whereas plate martensite is commonly observed at carbon contents ≥ 1 wt.% C. Intermediate carbon levels may result in a mixed morphology [27]. Lath martensite exhibits a hierarchical microstructure spanning multiple length scales, consisting of packets, blocks, and laths in decreasing order of size. A prior austenite grain contains several martensite packets sharing a common habit plane. Each packet is subdivided into blocks composed of laths with similar crystallographic orientations, with the block size often considered the effective grain size governing mechanical behavior [31]. The prior austenite grain size strongly influences this substructure: larger grains promote the formation of coarser packets and blocks, whereas finer austenite grains lead to a more refined martensitic hierarchy [32]. In contrast, plate martensite is characterized by larger, plate-shaped features that frequently extend across the entire austenite grain and contain a central midrib, surrounded by partially twinned and subsequently untwinned regions [33].

2.1.1 Tempering stages

Following rapid cooling, martensite exhibits very high hardness but is inherently brittle, resulting in limited toughness and ductility. To mitigate these drawbacks, bearing steels are typically subjected to a subsequent tempering treatment. Tempering involves reheating the hardened steel to a temperature above room temperature but below the critical austenite start temperature (A_{C1}) for a certain period of time. Under these conditions, martensite undergoes a sequence of thermally activated phase transformations. These transformations occur in distinct stages that are governed by both tempering temperature and time, and are associated with specific microstructural changes [34,35].

- Segregation (T < 100 °C): Carbon atoms diffuse towards dislocations, with up to approximately 0.2 wt.% C participating in this redistribution.
- First stage (100 °C < T < 200 °C): Nanoscale transition carbides, primarily ε-carbides and η-carbides, precipitate within the martensitic matrix, accompanied by a partial reduction in lattice tetragonality.
- Second stage (200 °C < T < 300 °C): Retained austenite becomes unstable and decomposes into ferrite and cementite.
- Third stage (250 °C < T < 350 °C): Cementite (Fe_3C) precipitates at the expense of existing transition carbides, and the tetragonality of the martensitic matrix is eliminated, although shape deformation effects may persist.
- Fourth stage (350 °C < T < A_{C1}): Recovery processes dominate, including cementite coarsening and spheroidization, martensite lath coarsening, and the onset of recrystallization.

By carefully controlling the austenitization and tempering parameters, a tempered martensitic microstructure can be obtained that preserves much of the high strength associated with martensite while significantly improving ductility and toughness.

2.1.2 Dual-hardening steel

Dual-hardening steels were first introduced by Garrison and Bhat in 1988 [36] with the objective of developing high-strength martensitic steels that exhibit enhanced toughness while maintaining a reduced carbon content. The concept of dual hardening refers to achieving high strength through the simultaneous contribution of two distinct strengthening mechanisms: precipitation of intermetallics, as observed in maraging steels, and precipitation of secondary carbides, which is characteristic of secondary hardening in tool steels [37]. Intermetallic precipitation strengthening is a defining feature of maraging steels, which consist of a martensitic matrix containing a fine dispersion of nanoscale precipitates. In these steels, strength is derived not from carbon, but from the ageing of low-carbon martensite, during which intermetallic phases form. At ageing temperatures, typically in the range of 400-500 °C, intermetallic precipitation occurs and is significantly accelerated by the high dislocation density of the martensitic matrix, which enhances the diffusion of substitutional alloying elements. The resulting high volume fraction of finely distributed intermetallic precipitates enables the achievement of very high strength [38]. In contrast, secondary hardening arises during the tempering of alloy steels at higher temperatures, generally between 500 and 600 °C (4th stage tempering). At lower temperatures, the diffusion of substitutional alloying elements is insufficient to permit the nucleation of alloy carbides. As tempering temperature increases, metallic alloying elements diffuse substitutionally and combine with carbon to form thermodynamically stable secondary carbides. This mechanism differs fundamentally from the behavior of carbon and nitrogen, which diffuse interstitially through the iron lattice. Strong carbide-forming elements such as Cr, Mo, W, V, and Nb promote the formation of carbides including M_2C, M_6C, M_7C_3, $M_{23}C_6$, and MC. The fine dispersion of these carbides within the martensitic matrix is responsible for the secondary hardening effect [34].

2.2 AISI 52100 steel

The work addressing **research questions 1 and 2** is primarily focused on this steel. SAE/ASTM/AISI 52100 steel also designated as DIN 100Cr6, SUJ2, and EN31 is a high-carbon, chromium-alloyed bearing steel. Its nominal chemical composition is listed in Table 1. In its initial condition, AISI 52100 is supplied in a spheroidized annealed state, characterized by finely dispersed, nearly spherical $(Fe,Cr)_3C$ cementite particles embedded within a ferritic matrix. This microstructure typically exhibits a hardness of ~200 HV. During spheroidization, chromium preferentially partitions into the cementite phase, forming $(Fe,Cr)_3C$, which contributes to the stability and morphology of the carbide particles and is well suited for machining operations [38]. The hardness requirement for bearing components is typically around 700 HV (58 HRC - 62 HRC) [39]. To attain these final properties, the steel undergoes a through-hardening heat treatment process. This process begins with austenitization at 840 °C, during which ~3-4% of $(Fe,Cr)_3C$ remains undissolved, followed by rapid quenching in oil to achieve a martensitic microstructure. Subsequently, tempering is carried out at about 240 °C (2nd stage) to reduce the RA content to <2%.

Table 1: Chemical composition of 52100 steel used in the current study, Fe-bal.

Element	C	Mn	Cr	Si	S	P
Wt.%	0.95	0.32	1.42	0.26	0.001	0.009

Following through-hardening, the microstructure consists mainly of lath or plate martensite with a fine dispersion of nano-sized tempered cementite (θ) and µm-sized nearly spherical $(Fe, Cr)_3C$ cementite (Figs. 2a,b). The resulting tempered martensitic microstructure exhibits a hardness of 58-60 HRC. Quantitative electron backscattered diffraction (EBSD) analysis shows that the volume fraction of µm-sized $(Fe, Cr)_3C$ cementite precipitates is 3.6% (Fig. 2d), with an average equivalent diameter of 0.8 ± 0.2 µm and an average aspect ratio of 1.5 ± 0.4, confirming their nearly spherical morphology.

The EBSD inverse pole figure (IPF) map along the x-axis (Fig. 2c), reveals random crystallographic orientation distribution. Analysis of martensite block boundaries indicates a weighted-average block size of 1.9 ± 0.6 μm with a fitted ellipse aspect ratio of 3 ± 1.4, considering high-angle grain boundaries (HAGBs) of >10°. Reconstruction of the prior austenite grain structure from EBSD data (Fig. 2c) gives an average grain size of 10.1 ± 2.3 μm.

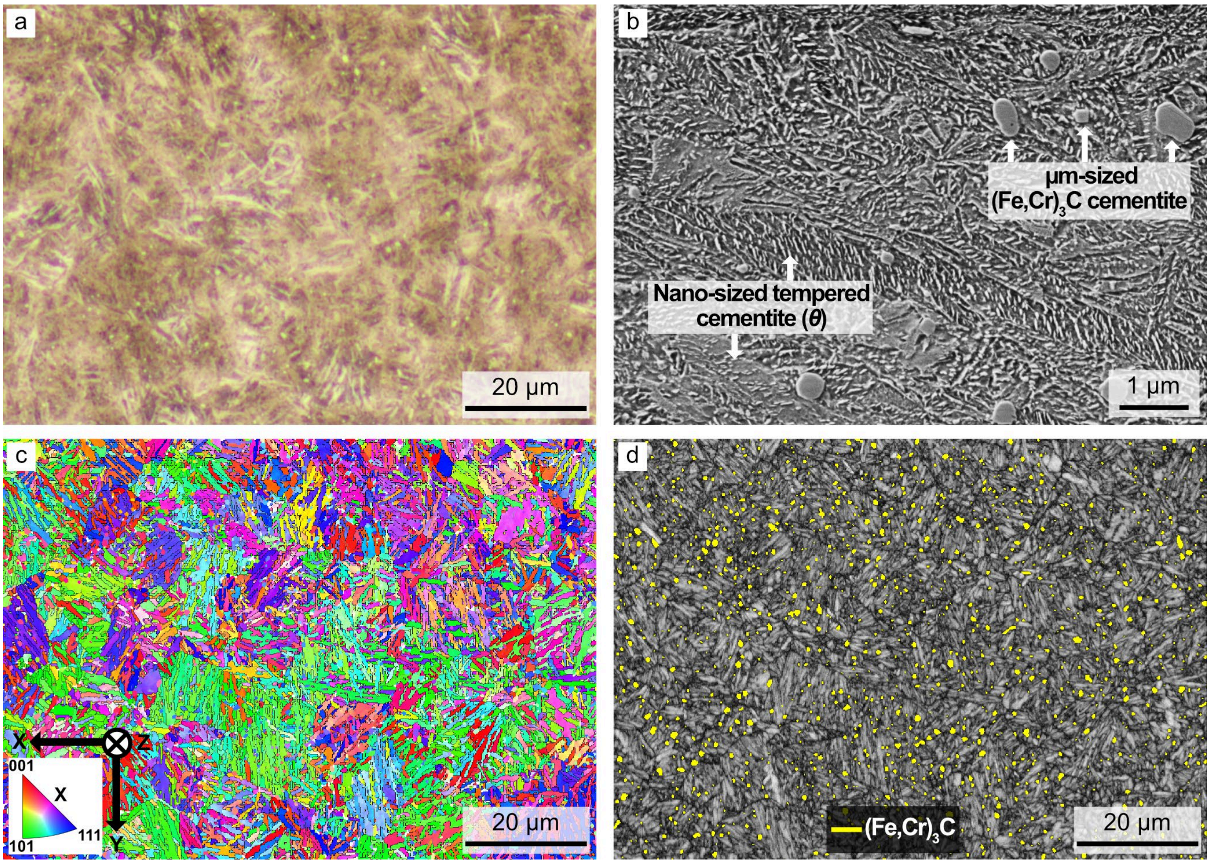

Fig.2: Through-hardened AISI 52100 steel microstructure. (a) LOM image of the tempered martensite etched with 2% Nital. (b) SE-SEM image of the tempered martensitic microstructure showing tempered cementite (θ) and (Fe, Cr)$_3$C cementite. (c) EBSD IPF orientation map. (d) EBSD band contrast image with (Fe, Cr)$_3$C cementite particles phase map.

Depending on the application, the microstructure of bearing steels is optimized with respect to RA content and carbide distribution. In this thesis, particular emphasis is placed on the role of RA in WL formation. Two RA levels, ~12% and ~25%, were produced in AISI 52100 steel by modifying the heat-treatment parameters, and the resulting microstructures are shown in Fig. 3 [39]. Batch 1 specimens were austenitized at 860 °C for 120 minutes with a furnace carbon potential of 0.75%, resulting in ~12% RA. Batch 2 specimens were austenitized at 920 °C for the same duration with an increased carbon potential of 0.8%, producing ~25% RA. Maintaining the carbon potential was essential to prevent decarburization at the higher temperature. All specimens were oil-quenched at 80 °C and subsequently tempered at 160 °C for 60 minutes. Owing to the higher austenitization temperature and carbon potential, batch 2 exhibited a predominantly plate martensitic microstructure (Fig. 3b), in contrast to the lath dominated structure in batch 1 (Fig. 3a). Both conditions achieved a final hardness of 61 ± 2 HRC. The increase in RA content with higher austenitization temperature is primarily attributed to the enhanced carbon enrichment of the austenite phase from the (Fe, Cr)$_3$C cementite particles. The higher carbon levels stabilize austenite by lowering the M_s temperature, thereby suppressing its transformation during quenching. Consequently, by adjusting the austenitization temperature and carbon potential, controlled variations in RA volume fraction can be achieved [40].

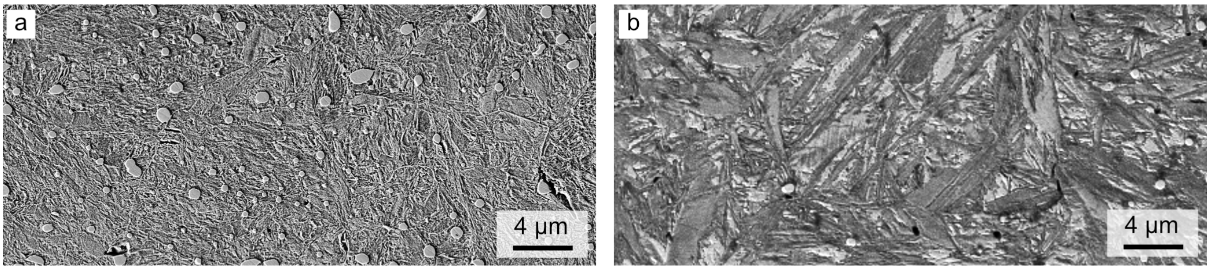

Fig.3: AISI 52100 steel microstructure with (a) ~12% RA and (b) ~25% RA.

2.3 Hybrid 60 steel

The material investigated in **research question 3** was a dual-hardening Hybrid 60 steel (Ovako 397A), supplied by Ovako AB. Hybrid 60 steel has been developed by Ovako AB to integrate advantageous characteristics of tool steels, maraging steels, stainless steels, and low-carbon engineering steels [41,42]. It is classified as a dual-hardening steel, as its strength is achieved during ageing at 500-600 °C through the combined precipitation of nanometer-scale, incoherent chromium-rich (Cr-rich) secondary carbides and coherent intermetallic phases [43–45]. According to EN 10027 designation rules, Hybrid 60 corresponds to X30NiCrAlMoV6-5-2-1, however, it is not currently recognized as an official EN standard grade. The chemical composition of the steel, expressed in weight percent (wt.%), is provided in Table 2. The as-rolled, soft annealed steel bar with dimensions of 114 mm diameter and 200 mm length was subjected to a heat treatment process to achieve the desired final microstructure. Austenitization was carried out at 1020 °C for 1 h, followed by air cooling to room temperature, which resulted in martensite formation due to the presence of substantial amounts of diffusion-inhibiting alloying elements, lowering the critical cooling rate. Subsequently, the material was tempered/aged at 520 °C for 4 h to promote the precipitation of intermetallic phases and secondary carbides. This treatment resulted in a final hardness of 683 ± 7 HV1, corresponding to ~60 HRC.

Table 2. Hybrid 60 steel chemical composition (wt.%) as provided by Ovako AB.

Hybrid 60	C	Si	Mn	Cr	Ni	Mo	V	Al	Fe
wt.%	0.28	0.1	0.3	5.61	5.94	0.69	0.49	2.41	Bal.

The initial microstructure of the heat-treated Hybrid 60 steel was characterized using EBSD, Bright field-scanning transmission electron microscopy (BF-STEM), and atom probe tomography (APT), as shown in Fig. 4. The EBSD band contrast image (Fig. 4a) reveals a tempered martensitic microstructure, while the corresponding IPF map (Fig. 4b) indicates a homogeneous distribution of crystallographic orientations. BF-STEM imaging (Fig. 4c) further confirms that the microstructure consists predominantly of lath martensite with an average lath width of ~1 μm, consistent with the low carbon content of the alloy. In addition, spherical vanadium-rich (V-rich) primary MC carbides are observed dispersed throughout the matrix (Fig. 4c). Quantitative EBSD analysis yields an average area-weighted martensite block width of 4 ± 2 μm, with a fitted ellipse aspect ratio of 3.4 ± 1.5. Nanoscale precipitates formed during tempering at 520 °C for 4 h could not be resolved by electron microscopy and were therefore examined using APT. The APT reconstruction (Fig. 4d) reveals a high number density of uniformly distributed NiAl intermetallic precipitates (green) and Cr-rich secondary carbides (blue), identified using 17 at.% (Ni + Al) and 8 at.% Cr isoconcentration surfaces. Further APT analysis indicates that the Cr-rich secondary carbides correspond to either M_7C_3 or $M_{23}C_6$ carbides. Proximity histograms (proxigrams) for the Cr-rich carbides and NiAl intermetallics are presented in Fig. 4d1 and Fig. 4d2, respectively. The APT proxigram of the Cr-rich secondary carbides averaged over both carbide types, shows a closer match of the stoichiometry to that of $M_{23}C_6$ (21 at.% C) rather than M_7C_3 (30 at.% C), suggesting that $M_{23}C_6$ is the more prevalent phase. However, definitive identification of such nanoscale carbides remains challenging. Overall, the resulting microstructure of Hybrid 60 steel comprises lath tempered martensite strengthened by a combination of Cr-rich M_7C_3/$M_{23}C_6$ secondary carbides, NiAl intermetallic precipitates, and undissolved V-rich primary MC carbides.

2.4 Phase fractions of AISI 52100 and Hybrid 60 steels

The equilibrium phase fractions were calculated as a function of temperature for the compositions of AISI 52100 steel and Hybrid 60 steel used in this study using Thermo-Calc software. A comparison of the calculated phase fractions is shown in Fig. 5. The results indicate that the required austenitization temperatures differ between the two steels, with Hybrid 60 requiring higher austenitization temperatures. According to the Thermo-Calc predictions, the Cr-rich secondary carbides present at 520 °C are of the $M_{23}C_6$ type. The equilibrium phase diagram suggests that NiAl intermetallics are not thermodynamically stable above ~550 °C. In contrast, a recent study by Jakob et al. [45] reported the presence of NiAl intermetallics at 650 °C with coarsening behavior. This discrepancy highlights the limitations of equilibrium thermodynamic calculations in fully capturing the experimentally observed phase stability and precipitation behavior in Hybrid 60 steel.

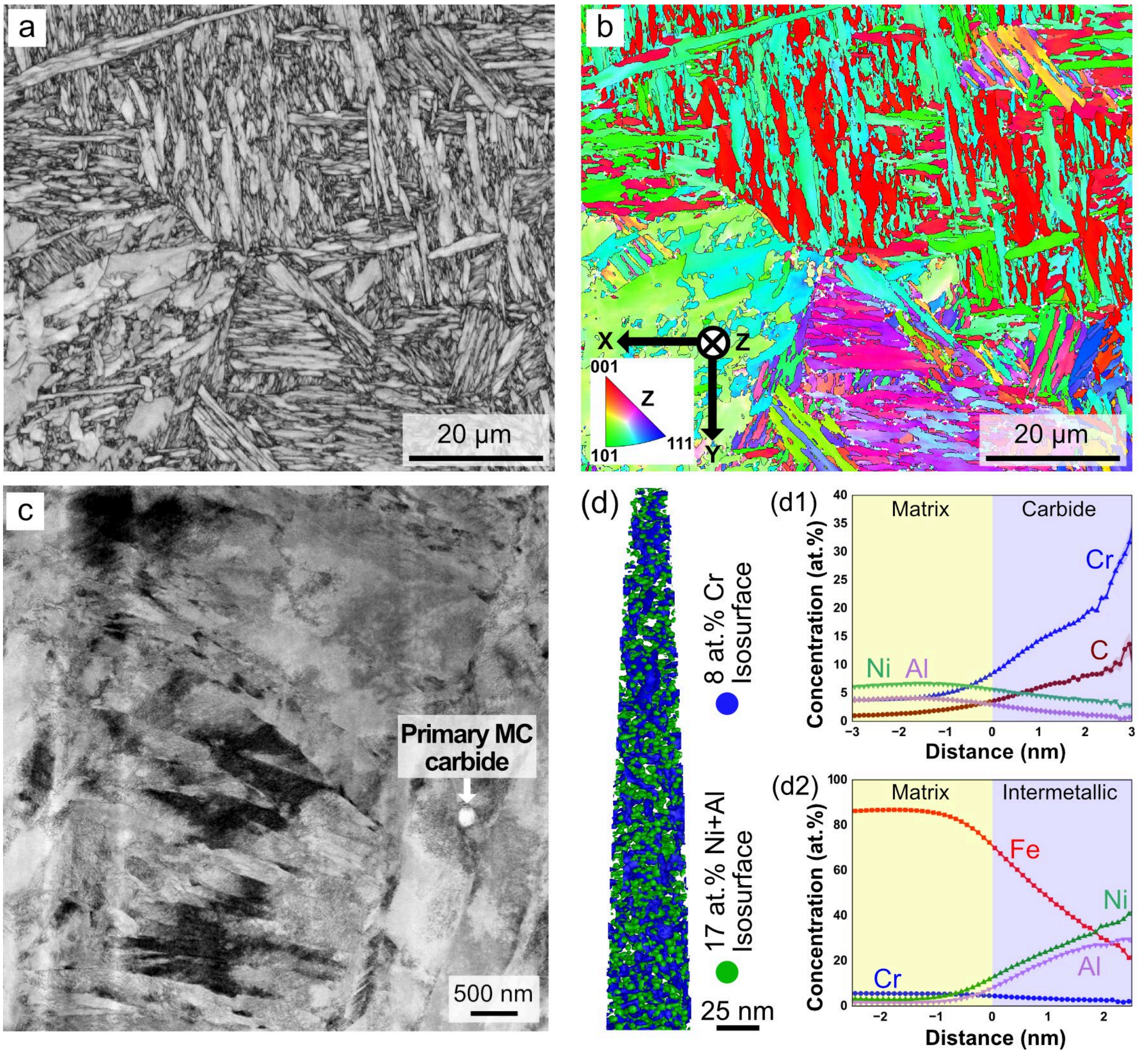

Fig. 4: Initial microstructure of Hybrid 60 steel. (a) EBSD band contrast image revealing tempered martensite. (b) EBSD IPF orientation map. (c) BF-STEM image showing the lath martensite structure. (d) APT reconstruction with 8 at.% Cr (blue) and 17 at.% Ni+Al (green) iso-surfaces to highlight the precipitates. (d1,d2) APT proxigrams showing the compositional variations across Cr-rich secondary carbides and NiAl intermetallic precipitates.

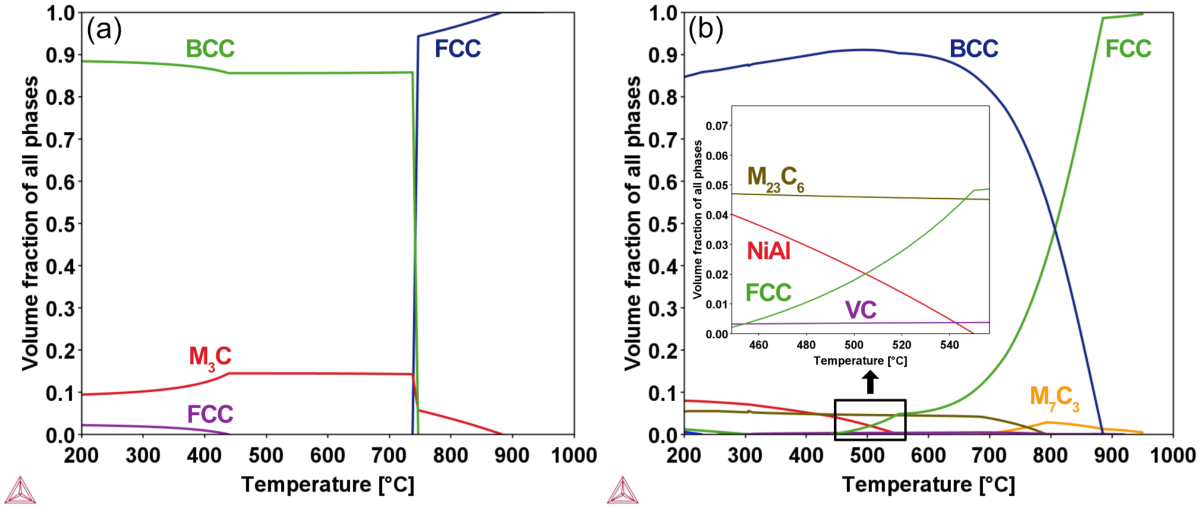

Fig. 5: One axis equilibrium phase fractions (Thermo-Calc) for (a) AISI 52100 steel and (b) Hybrid 60 steel.

CHAPTER 3

Hard Turning

This chapter provides an overview of hard turning and its surface integrity, followed by a critical review of the existing literature. Particular emphasis is placed on the influence of cutting parameters and tool geometry on surface integrity, with specific focus on residual stresses and surface roughness.

3.1 Introduction to metal cutting

The fundamental objective of traditional metal cutting processes is to generate a new surface with specified surface integrity on a workpiece by mechanically removing excess material in the form of chips. It is a subtractive process, and this objective can be achieved using tools with single-point (turning) or multi-point (milling) geometrically well-defined cutting edges, as well as tools with geometrically undefined cutting edges, such as grinding [46]. This thesis focuses specifically on hard turning, which employs a single-point, geometrically well-defined cutting edge. Hard turning is defined by its application to machine metallic materials with hardness exceeding 45 HRC [47]. Historically, such materials required grinding, but the advancement of hard turning offers a more flexible and efficient alternative for producing high precision components [2,48].

3.2 Fundamentals of hard turning

3.2.1 Cutting parameters

The generation of a machined surface is fundamentally based on establishing an appropriate relative motion between the workpiece and the cutting tool. In hard turning, the workpiece is clamped to a rotating chuck, while the opposite end is supported by a tailstock and the cutting tool moves along its surface, leading to chip formation as a result of this relative motion. When the tool is fed parallel to the workpiece's axis of rotation to reduce its diameter over a specific length, the process is classified as longitudinal turning, as illustrated in Fig. 6 [49].

The key cutting parameters governing machining processes are the cutting speed (V_c), feed rate (f), and depth of cut (a_p). Cutting speed denotes the relative velocity between the workpiece and the cutting tool and is typically expressed in meters per minute (m/min). The feed rate represents the distance travelled by the cutting tool per revolution of the workpiece and is measured in millimeters per revolution (mm/rev), whereas the depth of cut corresponds to the thickness of material removed and is expressed in millimeters (mm). The process parameters are schematically illustrated in Fig. 6.

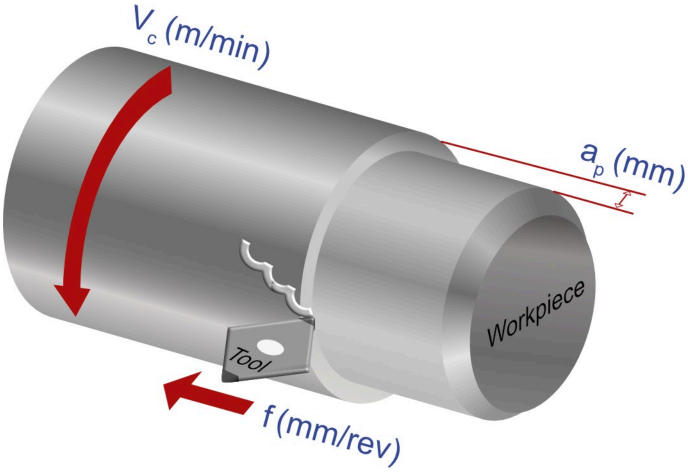

Fig. 6: Schematic illustration of the longitudinal hard turning process, showing the workpiece and tool motion, along with the key process parameters: cutting speed (V_c), feed rate (f), and depth of cut (a_p).

3.2.2 Cutting tool

Cutting tools employed in hard turning are subjected to severe mechanical loads and elevated temperatures. Furthermore, significant frictional forces occur at both the tool-chip interface and the tool-workpiece interface. To perform hard turning effectively, cutting tools must therefore possess high wear resistance, superior hot hardness, sufficient toughness to resist fracture, and chemical stability as well as physical stability at high temperatures [50]. The introduction of polycrystalline cubic boron nitride (PCBN) cutting tools, consisting of sintered CBN grains bonded with a binder phase, has significantly advanced hard turning technology. Furthermore, the application of coatings to PCBN inserts and the optimization of tool geometry have enhanced cutting performance by reducing tool wear, thereby extending tool life and ensuring the desired surface quality of the machined workpiece [51].

Tool geometry

Cutting tool geometry has a significant influence on the hard turning process. A critical aspect of hard turning is the selection of an appropriate rake angle and the proper preparation of the cutting edge. When machining hardened steels, a negative rake angle is commonly employed and in addition, a positive clearance angle is maintained between the tool and the workpiece to prevent rubbing during cutting. This configuration promotes a robust cutting edge, thereby reducing the risk of edge chipping under high cutting forces. To further withstand the severe stresses generated during machining, a chamfer is often incorporated into the cutting-edge design [51,52]. Tool geometry parameters including tool nose radius, edge radius, and chamfer angle, when combined with cutting parameters such as cutting speed, feed rate, and depth of cut, play a crucial role in governing residual stress formation, surface roughness, and microstructural evolution on the machined surface after hard turning. The influence of these parameters on surface integrity is further discussed in Section 3.3. Figure 7 presents a schematic representation of the cutting tool geometry with important features.

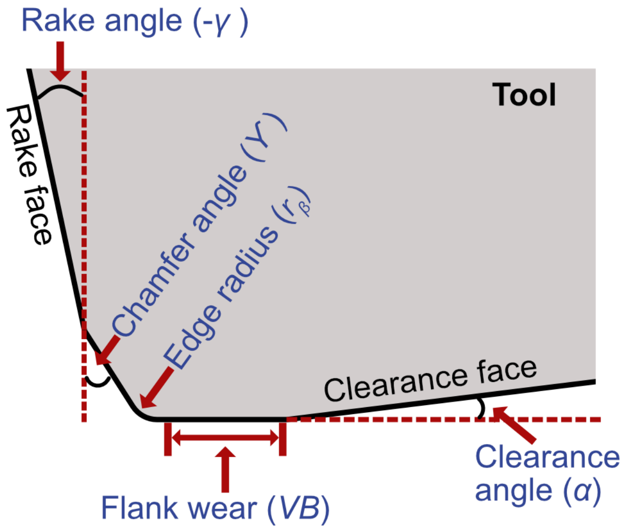

Fig. 7: Cutting tool geometry with important features.

Tool wear

Despite its capacity to produce surface integrity comparable to grinding in significantly shorter production cycles, hard turning is not yet widely adopted as a final finishing process. This limitation is primarily attributed to the continuous deterioration of the cutting tool, which results in progressive tool wear and directly influences the surface integrity of the machined workpiece. As tool wear advances, cutting forces and temperatures increase due to the enlarged contact length between the tool and workpiece during machining. Tool degradation can be broadly classified, based on its progression at the micro and macro-scale, into two main categories: wear and fracture [53].

The wear mechanisms active within the cutting zone are highly complex, driven by the simultaneous influence of mechanical, thermal, and chemical interactions. Consequently, tool wear may arise from multiple mechanisms acting concurrently or from a dominant mechanism depending on the prevailing cutting conditions. The principal wear mechanisms are commonly classified as: (a) abrasive wear, (b) adhesive wear, (c) diffusion wear, and (d) chemical wear. At low to moderate cutting speeds, mechanically driven abrasive and adhesive wear mechanisms tend to predominate. In contrast, at high cutting speeds, thermally activated mechanisms such as diffusion wear, thermal wear resulting from plastic deformation due to thermal softening, and chemical wear caused by oxidation and corrosion become dominant [51,53]. Due to the continuous chip removal process, tool wear is typically observed in two distinct regions of the cutting tool. Wear on the rake face is characterized by the formation of a crater or a built-up edge, resulting from the interaction between the flowing chip and the rake face, with adhesion and diffusion being the primary contributing mechanisms. In contrast, wear on the flank (clearance) face arises from intense friction between the cutting edge and the newly machined surface, where abrasion is the dominant wear mechanism [53].

Figure 8a shows a fresh cutting insert with a 15° chamfer angle after machining, exhibiting a flank wear width (*VB*) of ~0.04 mm, while Fig. 8b shows a pre-worn insert with a 35° chamfer angle after machining, with a *VB* of ~0.21 mm. The presence of both flank wear and crater wear on the worn insert is evident and has a pronounced effect on the resulting surface integrity. In hard turning operations, *VB* is generally regarded as the preferred and most relevant wear mode, as its gradual progression allows for better monitoring and control while having a direct impact on surface quality. Accordingly, this thesis focuses on investigating the influence of tool flank wear on residual stress distribution, surface roughness, and microstructure, in comparison with machining performed using fresh cutting inserts.

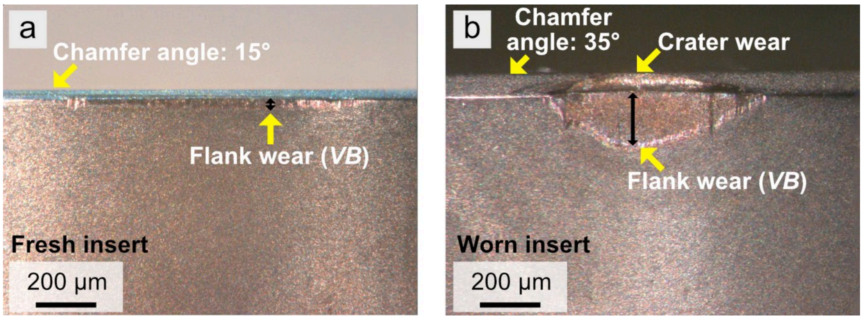

Fig. 8: (a) Fresh insert after machining, exhibiting a flank wear (VB) width of ~0.04 mm with a 15° chamfer angle. (b) Pre-worn cutting insert after machining, showing a flank wear (VB) width of ~0.21 mm with a 35° chamfer angle, along with evident crater wear on the rake face [54].

3.2.3 Heat generation and deformation zones

During hard turning, ~97% of the mechanical energy is converted into thermal energy as a result of plastic deformation of the workpiece material and frictional work at the tool-workpiece and tool-chip interfaces. Heat generation occurs within three distinct shear zones namely the primary, secondary, and tertiary zones and is subsequently distributed among the workpiece, cutting tool, and chip, as illustrated in Fig. 9. The primary shear zone (zone I) is the region where material from the workpiece undergoes severe plastic deformation and is sheared to form the chip. This zone extends from the cutting tool tip to the point where the undeformed workpiece surface intersects the deformed chip. Heat generation in this region is primarily due to plastic deformation, which leads to material softening and increased strain. Approximately 80% of the total heat is generated in the primary shear zone, of which nearly 75% is carried away by the chip, while about 5% is conducted into the workpiece. The secondary shear zone (zone II) is located at the interface between the tool rake face and the flowing chip. Heat in this zone is generated by both plastic deformation of the chip and friction at the tool-chip interface. Of the remaining 20% of thermal energy, approximately 18% is produced within this secondary zone. The tertiary shear zone (zone III) develops beneath the tool clearance face on the freshly machined surface, where the material is subjected to compressive and tensile stresses. The remaining 2% of the heat is generated in this zone due to plastic deformation of the newly formed surface and frictional interaction between the clearance face and the machined surface [51,55].

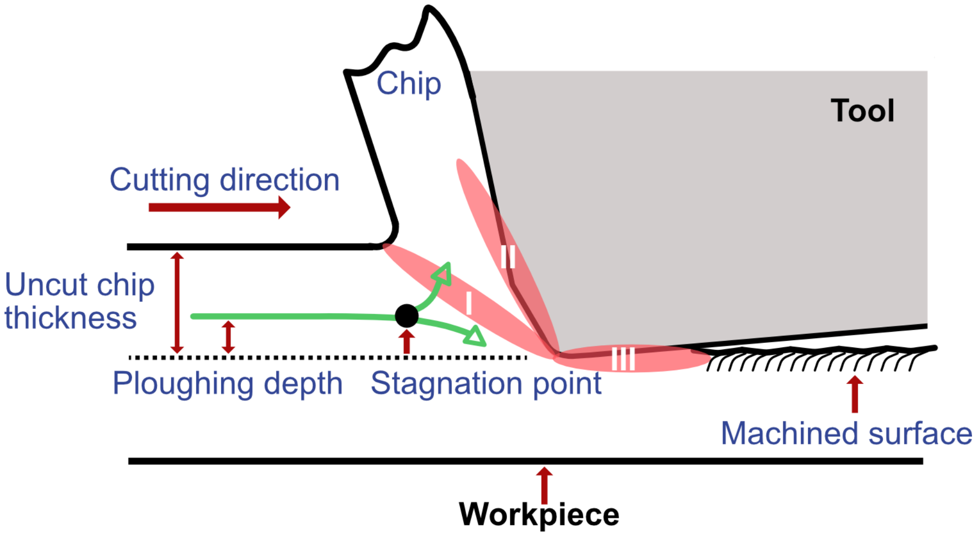

Fig. 9: Schematic representation of the deformation zones in hard turning: primary shear zone (I), secondary shear zone (II), and tertiary shear zone (III). The stagnation point, where the material flow divides to form the chip and the machined surface, is also indicated.

During cutting, the material ahead of the tool tip is either displaced upward along the rake face to form a chip or ploughed beneath the cutting edge to generate the machined surface. The location at which the material flow separates to form the chip and the machined surface is referred to as the stagnation point, as shown in Fig. 9 [55]. The thickness of material ploughed into the machined surface is referred to as the ploughed depth. The material ploughed beneath the cutting tool is subsequently stretched by the clearance (flank) face, where it undergoes severe plastic deformation and is subjected to elevated temperatures, ultimately forming the topmost layer of the machined surface. Further, the combined effects of friction and elevated temperature at the tool-workpiece and tool-chip interfaces accelerates tool wear through multiple simultaneous mechanisms, ultimately leading to deterioration in surface integrity. To mitigate these adverse effects, cutting fluids are commonly employed to reduce friction and dissipate heat during machining. In hard turning operations, the application of cutting fluids provides three primary benefits: (a) cooling of the cutting zone, (b) lubrication at the tool-chip interface, and (c) effective removal of chips from the workpiece [51].

3.3 Surface integrity

Surface integrity refers to the changes that occur on a component during the manufacturing process, which can influence its properties and overall service performance. It has been defined as "*The inherent or enhanced condition of a surface produced in machining or other surface generation processes*" [56]. Given that components often experience dynamic loads following hard turning, surface integrity can be broadly categorized into two main aspects [57,58].

- Geometric irregularities: including surface finish and texture.
- Internal subsurface characteristics: including metallurgical features, hardness, and residual stresses.

This section focuses on surface topography and residual stresses, while metallurgical features and hardness effects are discussed in detail in Chapter 4.

Surface topography: Surface topography arises from a combination of factors related to the manufacturing process and the inherent properties of the workpiece material. Irregularities in surface topography can be classified into three types: surface form, surface waviness, and surface roughness. Form and waviness are generally caused by macrogeometry errors, such as cutting tool instability and workpiece deflection, whereas roughness pertains to microgeometry deviations. The present work emphasizes evaluating surface roughness generated under varied cutting conditions. Surface roughness is defined as the high-frequency irregularities on a surface resulting from the interaction between cutting tool parameters and the workpiece microstructure [57]. In hard turning, surface roughness is primarily influenced by tool geometry, cutting speed, and feed rate. Secondary factors, including built-up edge formation, tool wear, and machine-tool dynamics, also play a significant role in determining the final surface quality.

Residual Stresses: Residual stresses are internal stresses that remain in equilibrium within a component in the absence of external loads or thermal gradients. These are classified across three length scales: Type I (macro) stresses, which balance throughout the material bulk; Type II (micro) stresses, which equilibrate among individual grains or phases; and Type III (sub-micro) stresses, which occur at atomic dimensions and are balanced by defects such as dislocations and vacancies. All three types are typically present to varying degrees in machined components [59]. The final distribution of these stresses in a machined component is a combined result of previous material processing and the simultaneous thermal and mechanical effects of the hard turning process itself. The resulting residual stress state is governed by three competing mechanisms. First, the mechanical pressure and rubbing between the tool and workpiece induce plastic deformation, typically generating favorable compressive residual stresses. Second, intense friction at the tool-workpiece interface generates localized heat, causing a constrained thermal expansion that may exceed the yield stress upon cooling, the subsequent thermal contraction results in tensile residual stresses at the surface.

Finally, elevated cutting temperatures can trigger phase transformations. In hardenable steels, the rapid heating and quenching cycle can generate martensite, which introduces compressive stresses due to the volumetric expansion associated with the phase transformation [57].

3.3.1 Influence of cutting parameters and tool geometry on surface integrity

The influence of cutting parameters and tool geometry on surface integrity in hard turning has been extensively investigated, resulting in a wide range of reported findings. In particular, residual stress formation has been shown to be strongly dependent on the interplay between thermo-mechanical effects during machining, as mentioned in the above section.

Navas et al. [60] examined the effect of feed rate on surface residual stresses in AISI 4340 steel and reported that increasing the feed rate led to higher tensile residual stresses at the surface. This behaviour was attributed to elevated cutting temperatures arising from increased chip thickness, which intensifies heat generation through plastic deformation during chip formation and promotes thermally induced tensile stresses. In contrast, Dahlman et al. [61] investigated the effects of rake angle and feed rate during hard turning of AISI 52100 steel and observed that higher feed rates combined with larger negative rake angles resulted in increased compressive residual stresses beneath the surface. A more negative rake angle enhances mechanical loading in the subsurface due to increased passive cutting forces, thereby promoting compressive stress formation [62]. The role of feed rate in residual stress development has also been linked to subsurface plastic deformation. Higher feed rates lead to increased cutting temperatures and tensile plastic deformation beneath the flank face, with the affected deformation zone extending deeper into the workpiece as feed increases. Upon unloading, this deformation results in a reversal of the stress state, producing deeper compressive residual stresses below the surface [62–64]. The effect of cutting speed on residual stresses was reported by Gunnberg et al. [62] for hard-turned case-carburized 18MnCr5 steel using PCBN tools. Their results showed that higher cutting speeds generated increased heat, leading to elevated surface temperatures and tensile residual stresses at the surface. However, because a major portion of the generated heat is carried away by the chip, thermal penetration into the workpiece remains limited, thereby reducing the influence of cutting speed on subsurface residual stress development. Several studies have further reported that the depth of cut has a negligible effect on residual stress generation in hard turning [61,62,65]. Tool wear (VB) has also been identified as a critical factor influencing residual stress distribution. Abrão et al. [66] reported that worn cutting inserts produced higher compressive residual stresses at a depth of ~20 μm beneath the surface when machining AISI 52100 steel. This behaviour was attributed to the increased cutting forces required by worn tools, which intensify mechanical loading compared to sharp inserts. Similarly, Liu et al. [67] investigated residual stress evolution in SuJ2 bearing steel and observed that increasing tool wear resulted in higher surface tensile stresses along with enhanced compressive stresses beneath the surface. These effects were linked to elevated frictional heating and plastic deformation at the tool-workpiece interface, as well as increased passive forces caused by the enlarged contact area. Comparable trends were also reported by König et al. [68]. In addition to cutting parameters and tool wear, tool edge geometry plays a significant role in residual stress formation. Hua et al. [64] studied the influence of hone radius and chamfer angle during hard turning of AISI 52100 steel and found that the incorporation of a chamfer combined with a hone radius increased subsurface compressive residual stresses. This effect was attributed to enhanced edge rounding and burnishing action at the cutting edge, which promotes substantial elastic and plastic deformation of the machined surface. Varela et al. [69] reported similar findings, noting that chamfered and honed cutting edges effectively increase the negative rake angle, leading to higher cutting forces and, consequently, increased compressive residual stresses.

According to well established theoretical expression shown in equation 2, the surface roughness (R_a) of hard-turned components is predominantly governed by the feed rate (f, mm/rev) and the tool nose radius ($R\varepsilon$, mm), which are widely recognized as the primary parameters influencing surface finish in turning operations.

$$R_{\mathrm{a}} = \frac{f^2}{32R\varepsilon} \qquad (2)$$

According to the theoretical model, the calculated surface roughness may deviate from experimentally measured values, being either higher or lower depending on the cutting conditions. This discrepancy can be primarily attributed to material plastic flow induced by the honed cutting-edge geometry, which is not accounted for in the theoretical equation. As the model considers only kinematic effects associated with feed rate and tool nose radius, it neglects the influence of edge geometry and associated ploughing phenomena. At a constant tool nose radius, increasing the feed rate leads to higher surface roughness due to the increased spacing between successive feed marks. Benga et al. [70] reported that lower feed rates produced smoother surfaces in hard-turned AISI 52100 steel, while identifying an optimal cutting speed range of 116-130 m/min for minimum roughness. Cutting speeds below this range resulted in higher cutting forces due to insufficient thermal softening, whereas higher speeds promoted vibration and tool wear, both of which degraded surface finish. An increase in edge hone radius at a constant feed rate generally raises surface roughness as ploughing becomes more dominant than shearing [71]. The honed edge intensifies side plastic flow, particularly at low feed rates and high negative rake angles, leading to increased peak heights in the surface profile due to viscous flow-like behaviour. This mechanism is largely absent in tools with chamfered edges without a hone, resulting in surface roughness values closer to theoretical predictions. Although tool edge geometry affects surface roughness, feed rate remains the dominant influencing parameter [69,72].

CHAPTER 4

White Layers

4.1 Background

The term "*white layer"* (WL) also known as "*white etching layer*" describes a microstructural transformation of the metallic materials and appear featureless and white, when viewed under a LOM. The earliest observation of WLs dates back to 1912, when Stead reported their presence on steel wire ropes after service exposure [73]. He attributed their formation to intense frictional heating followed by quenching during operation. Since then, surface WL formation has been extensively identified and reported in various machining processes, including hard turning [7], grinding [74], milling [75], drilling [76], reaming [77], and electrical discharge machining [78]. Beyond machining applications, WLs have also been identified in rail-wheel interactions [79] and as adiabatic shear bands (ASBs) under high strain rate impact loading tests [80]. Additionally, it is important to distinguish surface WLs from subsurface degradation phenomena, such as white etching bands (WEBs) [81] and white etching cracks (WECs) [82], commonly found in AISI 52100 bearing steel. While these features share a similar etched appearance, their formation mechanisms typically driven by rolling contact fatigue, differ significantly from the WLs formation after hard turning. Ultimately, WLs represent a universal phenomenon observed across a diverse range of ferrous and non-ferrous alloys subjected to extreme thermo-mechanical or cyclic loading conditions.

The characteristic etch-resistant behavior and white appearance of the WL arise from the scattering of white light when the Nital etched surface in the LOM interacts with the visible light. Since the microstructural features within the altered region are smaller than the wavelength of visible light (400-700 nm), they remain unresolved in LOM and appear featureless. However, scanning electron microscopy (SEM) shows the grain refinement within the WL, while scanning transmission electron microscopy-in-SEM (STEM-in-SEM) further resolves the underlying NC grains even more precisely. This transition from a featureless layer to NC grains is shown in Fig. 10, which compares LOM, SEM, and STEM-in-SEM images of WL generated by hard turning.

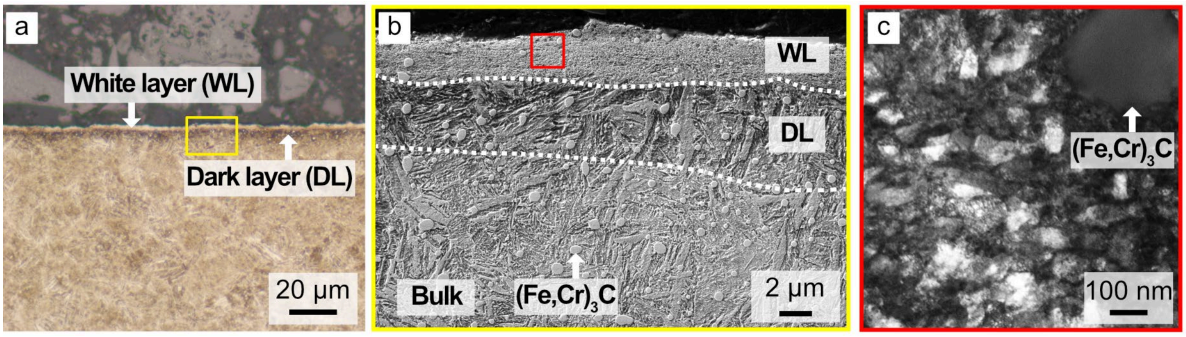

Fig. 10: Hard turning induced WL microstructure in AISI 52100 tempered martensite steel observed by (a) LOM, (b) SEM, and (c) STEM-in-SEM.

The WL is often accompanied by a subsurface microstructural transformation referred to as "*dark layer*" (DL). Both WLs and DLs formed on machined surfaces exhibit microstructural characteristics that differ significantly from those of the bulk material. The observed WL is typically untempered martensite formed through reverse martensitic transformation, whereas the DL consists predominantly of over-tempered martensite [9,83]. However, depending on the machining conditions and process parameters, a WL may form without an underlying DL. In 1975, Turley [77] investigated WL formation during the reaming of ultra-high strength steel and concluded that WLs with a fine subgrain structure result from surface fragmentation induced by SPD. In this case, no DL was observed beneath the WL and instead, a plastically deformed layer was present, as shown in Fig. 11a. Consistent with these observations, the present study also identifies WLs formed during hard turning of AISI 52100 tempered martensitic steel without the presence of an underlying DL, as shown in Fig. 11b.

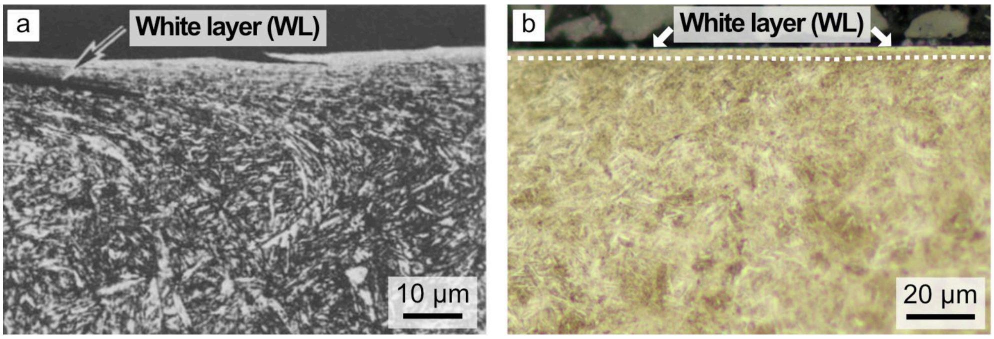

Fig. 11: (a) White etching surface formed during the reaming process, with a plastically deformed layer beneath it. The arrow indicates the presence of a thin WL. Reproduced with permission from Ref. [77]. (b) WL generated during the hard turning process in AISI 52100 tempered martensitic steel, with no underlying DL observed.

The formation mechanisms of WLs have been extensively investigated. Griffiths [84] proposed three primary mechanisms responsible for WL generation: (a) the formation of an ultrafine-grained (UFG) structure resulting from SPD (mechanical effect), (b) phase transformation induced by rapid heating followed by quenching (thermal effect), and (c) surface reactions driven by environmental interactions (chemical effect). However, in the context of machining hardened steels, WL formation is predominantly attributed to the combined influence of mechanical and thermal effects.

4.2 Hard turning induced white layers

The formation of WLs during the hard turning process was first examined by Bailey et al. in 1976 [85]. In their study, WLs were observed on hardened AISI 4340 steel, when machined using a tungsten carbide cutting tool under varying cutting speeds and tool flank wear. They concluded that, under conditions of high cutting speed and tool flank wear, WL formation is primarily driven by phase transformations resulting from the elevated temperatures generated at the tool-workpiece interface. Subsequently, Chou and Evans [9] investigated WL formation in hard-turned AISI 52100 steel using a worn Al_2O_3-TiC ceramic cutting tool. Their results showed that increasing cutting speed led to an increase in WL thickness. Beyond a critical cutting speed, however, the increase in thickness gradually decreased. In contrast, WL thickness increased progressively with increasing tool wear. X-ray diffraction (XRD) analysis revealed a significantly higher RA content of 33% in the WL compared to the bulk material, which has 11% RA. This elevated RA content was attributed to thermally driven reverse martensitic transformation, potentially enhanced by plastic strain. Zemzemi et al. [86], using a multiphysics modeling approach, demonstrated that WL thickness increases with cutting speed, feed rate, and tool wear. These predictions are in good agreement with the experimental results reported by Capellini et al. [87], who investigated orthogonal turning of AISI 52100 steel and confirmed that WL thickness increases with cutting speed, feed rate, and tool wear. Furthermore, the tool microgeometry also influences WL formation, for example, increasing the chamfer width and length leads to thicker WLs [88]. In the literature, WL formation is generally associated with reverse martensitic phase transformation that occurs when the surface temperature of the workpiece exceeds the austenitization temperature defined by the equilibrium Fe-C phase diagram, followed by rapid quenching. While the formation of the DL underneath is typically attributed to the over-tempering of martensite caused by thermal gradients during hard turning. Based on this mechanism, Hosseini et al. [14] classified such WLs as thermally-induced white layers (T-WLs).

However, so far only a few studies have explicitly recognized the significant role of SPD in WL formation during hard turning [6,7,14,89]. This mechanism becomes dominant when the temperatures generated at the tool-workpiece interface are insufficient to initiate austenitization, which typically occurs under conditions of low cutting speed, low feed rate, and minimal tool wear. Under such conditions, mechanical deformation rather than thermal effects governs WL formation. Ramesh et al. [6] investigated WL formation in hard-turned AISI 52100 steel using a CBN cutting insert and reported that machining at a low cutting speed of 91 m/min produced WLs primarily due to SPD and resulted in grain refinement. In this case, the RA content was reduced, which was attributed to strain-induced phase transformation and/or tempering effects occurring during machining. In contrast, machining at a higher cutting speed of 273 m/min resulted in WL formation dominated by reverse martensitic transformation, accompanied by a high RA content. Similar trends were reported by Barry and Byrne [7] who observed that worn cutting inserts promoted the formation of T-WLs, whereas fresh inserts led to WLs without an underlying DL. Han et al. [89] examined cutting temperatures during orthogonal machining of annealed AISI 1045 steel and observed WL formation at temperatures below the phase transformation threshold, which they attributed to SPD. Furthermore, Hosseini et al. [14] studied WL formation at a low cutting speed of 30 m/min and reported the absence of a DL beneath the WLs. These WLs were classified as mechanically-induced white layers (M-WLs) and exhibited lower RA content than the bulk material. Further, TEM revealed elongated nanograins within the M-WL, indicative of dynamic recovery (DRV) process.

Grainsize and properties of white layers

A common feature of M-WL and T-WL is their NC grain structure. TEM studies have consistently determined grain sizes in these layers ranging from <10 nm to submicron sizes of 200 nm [7,8,14,90]. Ramesh et al. [6] reported that T-WLs exhibit relatively larger grains of ~20 nm compared to M-WLs, which typically contain finer grains of ~5 nm. Owing to their ultrafine grain size, WLs generally exhibit higher hardness than the bulk material, primarily as a result of Hall-Petch strengthening and increased dislocation density [91]. Zhang et al. [92] quantified this using the example of AISI 52100 steel and found that the hardness of the bulk material was 10.3 GPa, while the hardness in the T-WL increased to 12.5 GPa and the hardness in the DL decreased to 8.8 GPa due to over-tempering. In T-WLs, increased cutting speeds promote carbide dissolution, which preserved carbon in the martensitic matrix and further increases the hardness [6]. Hosseini et al. [10] reported that M-WLs have a 26% higher hardness than the bulk material, mainly due to SPD leading to the formation of NC grains, and that under these conditions no softer DL forms beneath the WL. The formation mechanism also dictates the resulting residual stress state. M-WLs, typically generated at low cutting speeds and feed rates, tend to induce beneficial surface compressive residual stresses. Conversely, T-WLs are associated with surface tensile residual stresses due to the dominant thermal loads from high cutting speeds, high feed rates, or significant tool wear [10,93].

4.3 Thermo-mechanical interactions

The metal cutting process is characterized by intense plastic deformation of the workpiece material confined to a small volume and occurring within extremely short timeframes. As established in Chapter 3, the combination of SPD and friction at the tool/chip/workpiece interfaces generates high temperatures within a constrained volume. This leads to thermo-mechanical interactions (TMIs) of varying strength, which control the formation of WLs. The nature of these interactions is influenced by process dependent factors such as: strain, strain rate, temperature, heating/cooling rates, and contact pressure. In addition, intrinsic workpiece properties such as initial grain size, chemical composition, crystal structure, specific heat capacity, and thermal conductivity also significantly affect the TMIs [5,94].

In conventional material testing, strain rates typically range from 10^{-3} to 10^{-1} s^{-1} under isothermal conditions. In contrast, machining processes involve strain rates in the order of 10^4-10^5 s^{-1} under predominantly adiabatic conditions, with total strains ranging between 1 and 10 [4,5]. Under adiabatic deformation, the strain rate controls the rate of heat generation, while the thermal conductivity of the material controls heat dissipation. For metallic materials subjected to strain rates exceeding 10^2 s^{-1}, deformation tends to localize, leading to rapid temperature increase within the deformed region. This temperature increase causes thermal softening and a reduction in flow stress. When the rate of heat generation exceeds heat dissipation, localized adiabatic shear deformation develops [95]. Zener and Hollomon [96] first identified ASBs in metals subjected to high strain rate ballistic impacts. In the context of hard turning, similar conditions prevail, where the strain rates in hard turning ranges between 10^4-10^6 s^{-1} and the contact times are restricted to a few microseconds, making adiabatic deformation relevant to WL formation [4,97].

Depending on the prevailing TMIs, the cutting temperatures associated with WL formation during hard turning may occur above or below the austenitization temperature range. Takashi et al. [98] investigated cutting temperatures during hard turning of AISI 52100 steel with a hardness of 700 HV1 using a CBN cutting insert. They reported cutting temperatures of ~800 °C at a cutting speed of 100 m/min, increasing to about 950 °C at 300 m/min near the tool flank. Similarly, Hosseini et al. [99] measured cutting temperatures during hard turning of AISI 52100 steel using a two-colour pyrometer and reported that T-WLs formed at temperatures between 820 °C and 900 °C. In contrast, M-WLs were observed to form at temperatures of ~550 °C, well below the austenitization temperature of ~750 °C. The large variation in reported temperatures can be attributed to the combined influence of heating rate, cooling rate, and hydrostatic pressure. During hard turning, estimated heating rates are extremely high, ranging from 10^4 to 10^6 °C/s [86]. Orlich et al. [100] showed that the heating rate strongly influences the phase transformation kinetics, which can be represented using Time-Temperature-Austenitization (TTA) diagram. High heating rates promote non-equilibrium conditions, shifting the austenitization phase transformation temperatures to higher values, thereby requiring higher re-austenitization temperatures. Simultaneously, mechanical loads during hard turning can generate contact pressures as high as 2 GPa [86]. The use of negative rake angles in combination with low feed rates results in very small uncut chip thicknesses, which effectively increases the negative rake angle and further increases the contact pressure at the tool-workpiece interface to form the chips [2]. According to the Clausius-Clapeyron relationship, increased hydrostatic pressure reduces the A_{c1} [101]. Han et al. [89] reported a reduction of ~45 °C in A_{c1} at a pressure of ~0.7 GPa for AISI 1045 steel, while Ramesh and Melkote [102] observed a reduction of about 100 °C in A_{c1} at a pressure of ~1.3 GPa for AISI 52100 steel. Variations in tool geometry alter cutting forces and contact area, thereby influencing the magnitude of contact pressure and, consequently, the transformation behavior. In addition to heating and pressure effects, cooling rates play a crucial role in defining the final WL microstructure. Surface cooling rates during hard turning can reach 10^4-10^5 °C/s, particularly when coolants are employed [99]. At extremely high cooling rates, well above the critical value, M_s has been reported to decrease for various alloy systems. For example, Bibby and Parr [103] observed a reduction of ~200 °C in the austenite to martensite transformation temperature of pure iron (0.0017 wt.% C) at cooling rates >10^3 °C/s. Ultimately, WL formation during hard turning is governed by a complex interplay of strain, strain rate, temperature, heating and cooling rates, and contact pressure. These factors collectively modify phase transformation kinetics and M_s temperatures, thereby influencing the resulting microstructural phases in WLs and their underlying formation mechanisms.

4.4 Microstructural evolution mechanisms

Based on the TMIs described above, the microstructural evolution within WLs can be predominantly governed by either thermal loads, resulting in T-WLs, or mechanical loads, resulting in M-WLs. Although both factors inevitably influence a hard-turned surface, their respective dominant contributions determine the resulting microstructure. In the well-established case of T-WLs, the microstructure consists of NC grains composed of untempered martensite. This structure is formed via reverse martensitic transformation and is typically characterized by an increased volume fraction of RA [14,83]. Beneath the T-WL, a DL is commonly observed, which is composed of over-tempered martensite [92]. Numerous studies have concluded that the NC grain structure in T-WLs formed under high strain rate and high temperature cutting conditions arises mainly from dynamic recrystallization (DRX), coupled with reverse martensitic transformation and severe plastic deformation [8,14,80,104]. However, material specific thermal properties influence this behavior. In AISI 52100 steel, the relatively high thermal conductivity facilitates heat dissipation into the workpiece material, typically resulting in DRX driven grain refinement alongside a distinct DL underneath. In contrast, materials with low thermal conductivity, such as Inconel 718, restrict the generated heat and microstructural changes entirely within the WL region, preventing DL formation [11]. The Hybrid 60 steel investigated in this study possesses significantly lower thermal conductivity than AISI 52100. Given the lack of literature on the hard turning of Hybrid 60, investigation of its microstructural reaction represents an important research gap, which is addressed in *Paper V*. Conversely, the NC grains observed in M-WLs formed at temperatures below the phase transformation threshold are primarily attributed to DRV processes driven by SPD [6,7,14,105]. Despite extensive studies, the exact sequence of mechanisms that cause grain refinement from the initial unaffected microstructure to the NC grains of an M-WL during hard turning is not yet sufficiently understood and requires further investigation.

4.4.1 Dynamic recovery

During thermo-plastic deformation in the hard turning process, the free energy of the material increases as a result of the rising dislocation density induced by plastic deformation, leading to work hardening and an associated increase in flow stress. At the initial stages of deformation, a large number of dislocations are generated. However, the overall grain morphology remains largely unchanged due to the relatively low accumulated plastic strain. As deformation progresses, adiabatic shear localization develops, resulting in a sharp increase in dislocation density. The material containing such a high density of defects is considered thermodynamically metastable [106]. With continued intense plastic shear, the original grain structure undergoes reorientation and elongation along the shear direction. As deformation becomes increasingly localized, dislocations begin to climb and rearrange, forming dislocation cells. This marks the onset of DRV, during which dislocation annihilation and rearrangement occur. Under the extreme deformation conditions characteristic of hard turning, the rate of dislocation generation exceeds the rate of dislocation annihilation, resulting in only partial recovery. Assisted by the localized temperature rise associated with SPD, dislocation tangles develop, creating regions of heterogeneous dislocation density and leading to the formation of subgrain boundaries. Progressive segmentation of these subgrains ultimately results in the refinement of the elongated grains into a NC structure [104–107]. Dislocation climb plays a critical role in DRV processes. In metals with high stacking fault energy (SFE) such as BCC iron, dislocation climb occurs readily, promoting efficient DRV [7,108].

Grain subdivision

SPD processes such as ARB [19], HPT [20], ECAP [21], and surface mechanical rolling treatment (SMRT) [109] are known to produce significant microstructural refinement, resulting in UFG structures. During plastic deformation, a fraction of the mechanical energy is stored within the metal, primarily in the form of dislocations. These dislocations are not randomly distributed, but accumulate to form dislocation boundaries that separate regions with comparatively low dislocation density. At higher strains, the microstructure evolves into a lamellar structure characterized by deformation induced dislocation boundaries with low to high angle misorientations, as illustrated in Fig. 12(a-d) [110,111]. Hansen and co-workers extensively investigated the evolution of deformation microstructures in metals and alloys and described this process as grain subdivision within an original grain [110,112,113]. According to this, deformation induced dislocation boundaries are classified into two distinct types: geometrically necessary boundaries (GNBs) and incidental dislocation boundaries (IDBs), which form through different mechanisms. GNBs develop between regions exhibiting different strain patterns in order to accommodate variations in lattice rotation. Such differences in strain patterns may arise from changes in the active slip systems, variations in the partitioning of slip activity within the same slip systems, or differences in the local strain level. These variations promote, on average, compatible deformation involving fewer slip systems and reduced dislocation interactions, thereby lowering the system energy. In contrast, IDBs form through the trapping of gliding dislocations, multiple IDBs are typically stored within each domain divided by GNBs and tend to adopt low energy configurations. Experimental studies have shown that both the density and misorientation angles of GNBs increase with increasing plastic strain, whereas the misorientation angles of IDBs increase to a much lesser extent [110–113]. In the context of the present hard turning study, appropriate control of process parameters led to the formation of M-WLs exhibiting lamellar grain structures in the material drag region. Such structures, previously not reported in hard-turned tempered martensitic steels, are shown in Fig. 12e,f. These lamellar morphologies are typically associated with low temperature SPD processes and provide valuable insight into the microstructural evolution mechanisms governing M-WL formation. A detailed discussion of these observations is presented in *Papers III-V*.

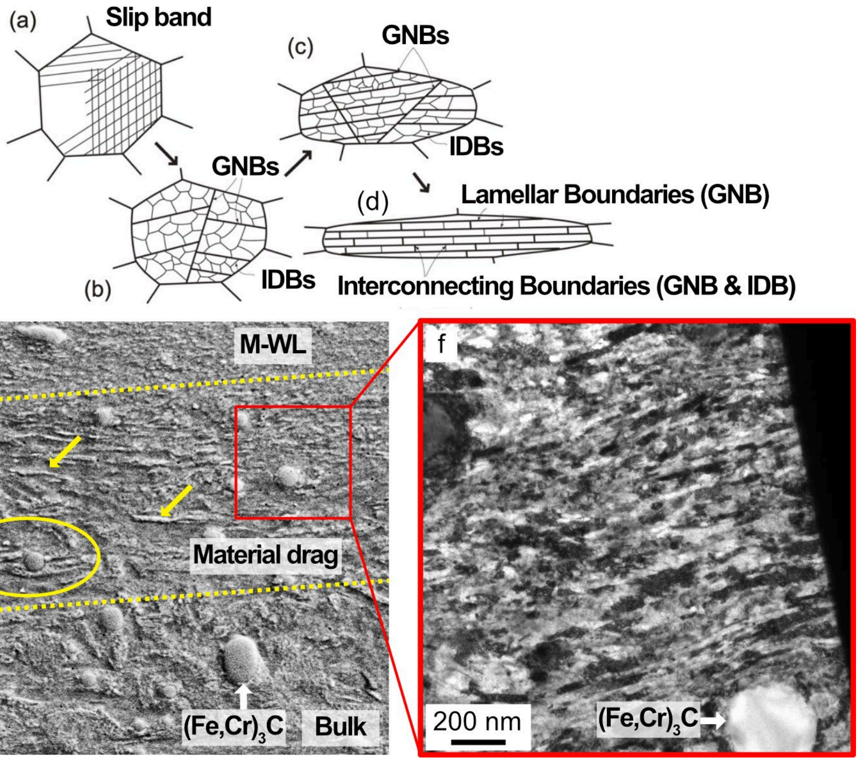

Fig. 12: (a-d) Schematic illustration showing the progression of grain subdivision within a grain of a polycrystalline material during plastic deformation. Reproduced from Ref. [111]. (e) SE-SEM image of material drag region exhibiting an elongated lamellar grains microstructure in AISI 52100 steel. Arrows indicate the elongated tempered martensitic structure, while the circled regions highlight elongated martensite flow lines around spherical cementite particles. (f) BF TEM image of lamellar grains formed in the material drag region after hard turning, oriented along the feed direction and exhibiting microstructural features analogous to those observed in bulk and surface SPD processes.

Triple junction motion

M-WLs consist of NC grains, and as discussed earlier, their formation is associated with the progressive segmentation of subgrain cells during DRV. However, the precise mechanisms governing this process during hard turning are not fully understood. Notably, Yu et al. [114,115] reported a structural evolution involving lamellar grains interconnected by triple junctions, consistent with the grain subdivision mechanism described in the preceding section. Based on their observations in cold rolled aluminium subjected to high strains, they proposed mechanically assisted triple junction motion as a DRV mechanism that facilitates grain refinement. Further, comparable microstructural behaviors have been reported by Renk et al. [116,117] in severely deformed tantalum at elevated temperatures and in severely deformed cold-rolled copper. Yu et al. [118] proposed a new DRV mechanism in which triple junction motion promotes the removal of thin lamellar boundaries, thereby driving the transition from a lamellar grain structure to an UFG microstructure. Within the context of deformation induced dislocation boundaries described earlier, three types of triple junctions have been identified by Yu et al. [115], as illustrated in Fig. 13a(i-iii), (i) Y-junctions, formed by three lamellar boundaries, (ii) H-junction pairs, formed by two lamellar boundaries connected by an interconnecting boundary, and (iii) r-junctions, formed by three interconnecting boundaries. Experimental evidence suggests that Y-junction motion is the dominant recovery mechanism in finely spaced lamellar structures [115]. As shown in Fig. 13b (yellow arrow), lamellar breakup leading to an UFG structure was observed during cold rolling of aluminium. The breakup of a lamella due to Y-junction motion (red arrow) is believed to result from localized shear deformation, whereby two lamellar boundaries converge, potentially through shear banding under extreme conditions [114]. In the context of hard turning, the observed lamellar grain thickness is significantly smaller than those reported in cold-rolled materials, and the resulting NC grains are correspondingly finer. These observations provide a strong motivation to investigate the microstructural evolution of M-WLs that form under the extreme thermo-mechanical conditions of hard turning, since the fundamental mechanisms of grain refinement down to the NC grains are not yet fully understood. This research gap is addressed in detail in *Paper IV and Paper V*.

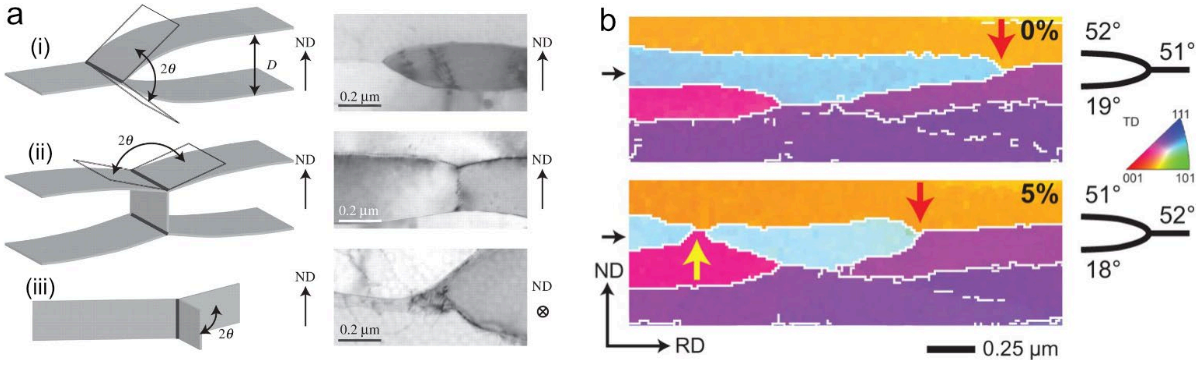

Fig. 13: (a) Schematic illustrations and representative examples of three types of triple junctions in lamellar microstructures: (i) a Y-junction formed by three lamellar boundaries, (ii) an H-junction pair formed by two lamellar boundaries connected by an interconnecting boundary, and (iii) a random r-junction formed by three interconnecting boundaries. Triple junctions are highlighted by bold lines, with dihedral angles (2θ) indicated. Reproduced with permission from Ref. [115]. (b) EBSD orientation maps showing Y-junction in the longitudinal section of cold-rolled 99.5% purity aluminium during rolling. The extent of additional rolling is indicated within each map. Migrating Y-junctions are marked by red arrows, while the corresponding shortening lamellae are indicated by black arrows. Boundaries with misorientation angles greater than 2° are shown in white. The misorientation angles of lamellar boundaries forming the migrating Y-junctions are illustrated schematically, and the yellow arrow highlights lamella break-up caused by localized shear during deformation. Reproduced from Ref. [114].

4.4.2 Dynamic recrystallization

Under high cutting conditions, characterized by increased cutting speed, feed rate, and tool wear, DRV initiates in the workpiece material and further the local temperature raises beyond the phase transformation threshold, causing the initial BCC/BCT tempered martensitic microstructure to transform into the FCC austenite phase. In addition, the substantial energy stored within the severely deformed and elongated grains during DRV significantly lowers the recrystallization temperature [119]. Once the material enters the austenitic FCC phase, the accumulated stored energy exceeds a critical level at which work hardening and recovery can no longer accommodate additional immobile dislocations. Under these conditions, a more intense restoration process known as DRX becomes energetically favorable, particularly in low SFE austenitic phases. At elevated temperature of 1000 °C, BCC iron exhibits a relatively high SFE of approximately 0.2 J/m^2, whereas FCC iron has a substantially lower SFE of about 0.075 J/m^2 [7]. Materials with low SFE experience restricted dislocation climb out of their glide planes, resulting in slow DRV and an increased susceptibility for DRX [119]. Consequently, the reduction in SFE associated with the BCC/BCT to FCC phase transformation possibly promotes the occurrence of DRX [7]. Given the extremely short time periods, typically found in the order of microseconds range during hard turning, discontinuous dynamic recrystallization (DDRX) is unlikely to occur as it relies on diffusion controlled grain boundary migration [120]. Instead, grain refinement is dominated by mechanically assisted progressive subgrain rotation associated with continuous dynamic recrystallization (CDRX), which refines the austenite grains to the nanometer scale [104,121]. Finally, due to the exceptionally high cooling rates, a characteristic of hard turning, the newly recrystallized austenite grains are rapidly quenched, transform into untempered martensite, and lead to the formation of T-WLs.

CHAPTER 5

Process and Material Characterization

This chapter begins by outlining the process employed to perform the hard turning. Following the experimental trials, a comprehensive characterization strategy was implemented to evaluate the surface integrity of the machined workpieces. To understand the phenomena across different length scales, multi-scale characterization techniques were applied, spanning from the millimeter scale down to the atomic scale. Residual stresses were analyzed using XRD, while surface roughness was quantified using vertical scanning interferometry (VSI). Metallographically prepared cross-sectional samples were first examined using LOM to identify the presence and distribution of WLs. However, detailed microstructural analysis within WLs required high resolution microscopy techniques. While electron microscopy enables the acquisition of high resolution images with crystallographic information, conventional methods are often limited in their ability to resolve the NC grains characteristics in WLs. To address this challenge, site-specific focused ion beam (FIB) lift-out technique was employed to prepare electron-transparent specimens. This approach significantly enhanced spatial resolution for subsequent analyses using STEM-in-SEM, transmission Kikuchi diffraction (TKD), and transmission electron microscopy (TEM). Preparing FIB lift-out samples to the highest quality is a time-consuming process that demands exceptional precision, and is often regarded as an art in itself. To further investigate the behavior of nanoprecipitates following hard turning, atom probe tomography (APT) was performed on FIB lift-out needle specimens, enabling three-dimensional chemical mapping at the atomic scale. Finally, the localized mechanical properties of the affected layers were characterized using nanoindentation and correlated with the observed microstructural features. Detailed descriptions of the specific experimental parameters and equipment used for each technique are provided in the following subsections. A comprehensive description of the materials investigated in this thesis is provided in Chapter 2.

5.1 Hard turning

Paper I, Paper III and Paper IV

The longitudinal hard turning experiments were conducted on a MONFORTS RNC500 SingleTurn machine under coolant conditions. Cylindrical ring specimens with a diameter of 180 mm and a length of 60 mm were machined and subsequently analyzed. To investigate the influence of cutting parameters on AISI 52100 steel surface integrity, cutting speed (V_c), feed rate (f), depth of cut (a_p), coolant pressure (P), tool chamfer angle (Y), and tool wear (VB) were varied between two levels, as summarized in Table 3 [63]. A tool flank wear value of VB = 0.2 mm represents a pre-treated tool state prior to experimentation. This pre-treatment was achieved by machining an additional workpiece using a new tool at a V_c of 110 m/min until a VB of ~0.2 mm was reached, while keeping f, a_p, and Y constant. *Paper III and Paper IV* investigate four cutting conditions by varying the V_c (60 m/min and 110 m/min), f (0.05 mm/rev and 0.2 mm/rev), and VB (0 and 0.2 mm), while keeping the a_p (0.2 mm), P (150 bar), and Y (35°) constant. This experimental design was chosen to differentiate the dominant mechanisms influencing surface integrity, specifically to determine whether they are thermally or mechanically induced. Across all three papers, TiAlBN-coated PCBN cutting tool inserts BNC 2125 (DNGA 1506 S01015/S01035) were used in all experiments. The inserts feature a nose radius of 2 mm, a CBN content of 65-70%, and a chamfer land width of 0.1 mm.

Table 3. Test parameters to understand the effect of cutting parameters on the surface integrity.

Parameters	Units	Low	High
Cutting speed (V_c)	m/min	60	110
Feed rate (f)	mm/rev	0,05	0,2
Depth of cut (a_p)	mm	0,05	0,2
Coolant pressure (P)	bar	20	150
Chamfer angle (γ)	°	15	35
Tool wear (VB)	mm	0	~0,2

Paper II

To examine the influence of RA content on WL formation and residual stress distribution in AISI 52100 steel, the hard turning experiments were conducted using the Hembrug precision lathe on cylindrical rod specimens with a length of 200 mm and a diameter of 34 mm. The study varies the V_c at two levels (60 m/min and 260 m/min), together with VB (0 and 0.2 mm). The f and a_p was kept constant at 0.16 mm/rev and 0.16 mm, respectively. All experiments were performed under flooding coolant conditions. TiAlN-coated PCBN cutting tool inserts BNC 200 (DNGA 150612 (HS)) were used consistently across all test conditions. The cutting tools featured a nose radius of 1.2 mm, a chamfer angle of 15°, a chamfer land width of 0.1 mm, and a CBN content of 65-70%.

Paper V

The longitudinal hard turning experiments were conducted on a MONFORTS RNC 500 SingleTurn lathe. The Hybrid 60 steel cylindrical bar specimens with a diameter of 114 mm and a length of 200 mm were machined and subsequently analyzed. The cutting tools employed in this study were coated PCBN inserts designated IT105 (DNGA 150612NU2), featuring a nose radius of 1.2 mm, a chamfer angle of 15°, and a CBN content of 75-80%. To ensure consistent machining conditions, all experiments were performed using cutting fluid supplied at a pressure of 20 bar, with a constant depth of cut of 0.2 mm, a clearance angle of 6°, and a rake angle of −41°. Two distinct sets of machining parameters were investigated using fresh cutting tool inserts, representing low and high cutting conditions. The low cutting condition was characterized by a V_c of 100 m/min and a f of 0.05 mm/rev, while the high cutting condition used a V_c of 200 m/min and a f of 0.2 mm/rev.

5.2 Sample preparation

5.2.1 Metallographic procedure

For microstructural analysis, cross-sectional specimens were prepared along the feed direction. The machined workpieces were sectioned using a Struers cutting machine and subsequently hot-mounted in conductive Struers PolyFast bakelite using a CitoPress 20. The wet grinding was initiated using P220 silica carbide paper, followed by sequential polishing with diamond suspensions of 9 µm, 3 µm, and 1 µm on the appropriate polishing cloths for 6 min, 6 min, and 3 min, respectively. All polishing steps were performed using a Struers TegraPol, resulting in scratch-free, mirror-finished surfaces. To reveal the WLs and DLs on the machined cross-sections, the specimens were etched with a 2% Nital solution (2 mL nitric acid in 98 mL ethanol) for 7-10 s. Due to the extremely thin WL region, the hard-turned surface of Hybrid 60 steel (*Paper V*) was electroplated with nickel (Ni) before hot-mounting to provide edge protection. For EBSD analysis (*Paper IV and Paper V*) and nanoindentation testing (*Paper III*), the samples were further polished using a 0.05 µm colloidal silica oxide polishing suspension (OPS) for 4 min following the 1 µm diamond polishing step. Prior to nanoindentation of the Ni-coated Hybrid 60 steel specimens (*Paper V*), the samples were mechanically polished down to the 1 µm diamond step, followed by ultrasonic cleaning. Final surface preparation was completed using a vibratory polisher with colloidal silica suspension to achieve a deformation-free surface suitable for nanoindentation testing.

5.2.2 Site-specific focused ion beam lift-out technique

The microstructure of the hard-turned surface, consisting of WLs and precipitates, was analyzed from the nanometer to atomic scale by extracting µm-sized specimens using a FIB lift-out technique in a dual-beam FEI Versa 3D instrument equipped with SEM. In this system, the FIB column is oriented at an angle of 52° relative to the vertically mounted electron column. The combined use of the two columns, together with a gas injection system (GIS) and a micromanipulator, enabled insitu site-specific preparation of regions of interest on machined surface. The SEM was primarily employed for imaging, however, in combination with the GIS, it was also used for electron-beam deposition of a thin metallic platinum (Pt) layer on the sample surface. This initial Pt deposition ensured that the region of interest remained visible and easily identifiable during subsequent FIB imaging. Although the FIB also has imaging capabilities, it was mainly used for ion-beam Pt deposition for protection and as a milling tool to create trenches and wedges at the sample surface through sputtering with a focused gallium ion (Ga^+) beam. The micromanipulator facilitated extraction of material for the preparation of electron-transparent lamellae and APT needles. Sample orientation was controlled by tilting the stage to align the specimen normal to either the electron- or ion-beam, enabling various milling, polishing, and deposition steps.

Specimen preparation for STEM and TKD

The individual steps involved in the standard lift-out procedure for preparing electron-transparent lamellae are illustrated in Fig. 14 (*Papers III-V*). An initial platinum (Pt) layer was deposited using the electron-beam (2 kV, 4 nA, 0° tilt), followed by ion-beam Pt deposition (30 kV, 100 pA, 52° tilt), as shown in Fig. 14b. FIB milling, including both rough milling and cleaning steps, was performed at 30 kV and a tilt angle of 52°, using progressively reduced beam currents ranging from 15 nA to 5 nA to create trenches required for the lift-out procedure, as shown in Fig. 14c. After undercut sectioning at a tilt angle of 7° (Fig. 14d), the lamella was lifted out at 0° tilt using a micromanipulator and subsequently welded to a copper (Cu) half-grid using ion-beam deposited Pt, enabling further thinning of the lamella (Fig. 14e). The presence of the WL was verified during the undercut step before welding the lamella to the half grid, as shown in Fig. 14d. Lamella thinning was carried out at 30 kV and 52° tilt (± a few degrees), with decreasing beam currents ranging from 1 nA to 50 pA to minimize ion-beam induced damage. Final polishing steps were performed at 5 kV and 48 pA, followed by 2 kV and 27 pA, to achieve electron transparency and to reduce the thickness of the FIB-induced amorphous layer (Fig. 14f). The final lamella thickness ranges from approximately 80 to 100 nm. Lamella thickness is a critical parameter for TKD, as it strongly influences both diffraction pattern quality and spatial resolution.

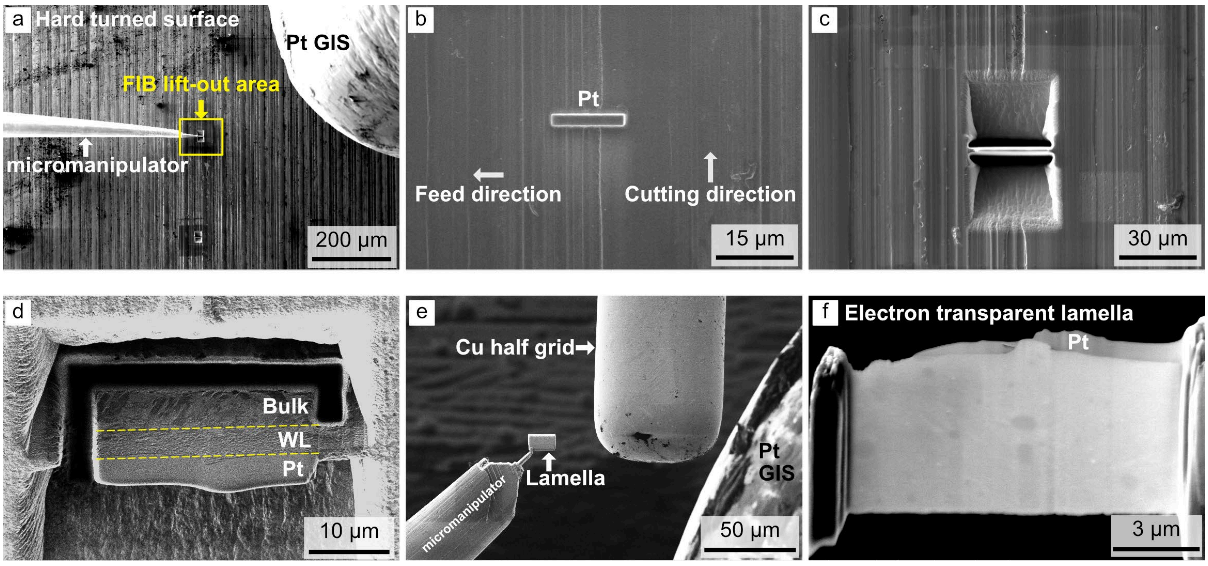

Fig. 14: Sample preparation using FIB for STEM and TKD analysis. (a) Overview of the selected area of interest (AOI) on the hard-turned surface. (b) Pt deposition on the AOI parallel to the feed direction. (c) Milling performed surrounding the AOI for the lift-out. (d) WL with refined microstructure observed beneath the Pt deposition. (e) Lamella extracted using a micromanipulator and welded to a Cu half-grid. (f) Final electron-transparent lamella obtained after thinning and polishing.

Specimen preparation for APT

The procedure for preparing APT needles closely follows the methodology used for electron-transparent lamellae, as illustrated in Fig. 15 (*Paper V*). The region of interest on the hard-turned surface was first marked with a platinum (Pt) layer using both electron-beam and ion-beam deposition (Fig. 15a). Similar trenches to those created for lamellae were then milled using the FIB at 30 kV and a 52° tilt. Next, the sample was tilted to 22°, and the FIB was used to mill trenches on both sides of the Pt strip (Fig. 15b). By rotating the sample 180°, a wedge-shaped geometry was created. At this stage, the thin WL region is identified and marked between the yellow lines to confirm its presence relative to the underlying lath martensite structure. The undercut and lift-out steps were performed similarly to the lamella preparation, however, the extracted material was welded onto a silicon (Si)-post (Fig. 15c). Multiple samples can be obtained from a single lift-out by repeating this process until the entire lamella was utilized. The sample was then rotated 180° and welded on the opposite side as needed (Fig. 15d). The final stage of APT sample preparation was sharpening. At this step, the sample was tilted to 52°, and annular FIB milling was applied to reduce the specimen into a sharp needle. This technique mills successive concentric circles along the axis of the ion beam, gradually reducing the radius to achieve a final tip size of ~50 nm, suitable for atom probe analysis (Fig. 15e).

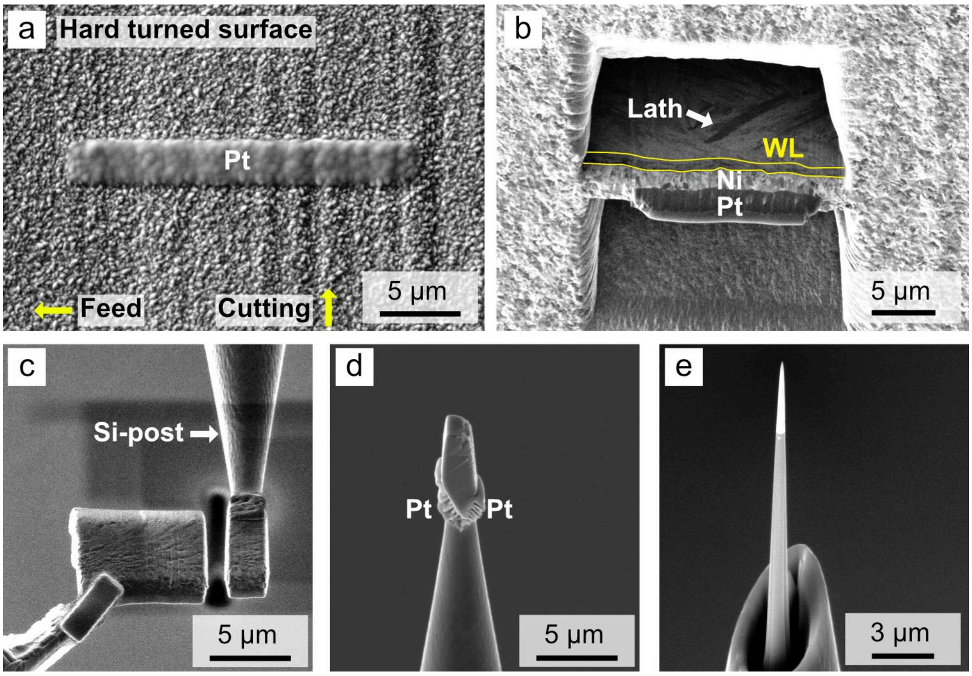

Fig. 15: (a) – (e) Overview of the sample preparation using FIB for APT needles on Hybrid 60 steel.

5.3 Material characterization techniques

5.3.1 X-ray diffraction

The XRD technique was employed to measure lattice strains induced by the hard turning process, and the corresponding residual stresses were calculated using elastic constants, assuming a linear elastic deformation of the relevant crystal lattice planes [122]. When the sample is irradiated with X-rays, the incident radiation interacts with the atomic lattice, resulting in the ejection of electrons from the outer shell. This interaction generates scattered X-ray beams, and those that satisfy Bragg's law (Equation 3) are detected as diffraction peaks originating from specific lattice planes. In Bragg's law, n represents the diffraction order, λ is the wavelength of the incident X-rays, d is the interplanar spacing, and θ denotes the angle of incidence [123].

$$n\lambda = 2d sin\theta \qquad (3)$$

When a metal is subjected to stress, it undergoes elongation and contraction, leading to changes in the interplanar spacing (d) of its {hkl} crystal lattice planes. These changes in lattice spacing cause corresponding shifts in the diffraction angle (2θ), observable as a shift in the diffraction peak. Accurate measurement of this peak shift enables the determination of the change in interplanar spacing, which in turn allows the calculation of strain within the material. Assuming a plane stress condition ($\sigma_z = 0$) and biaxial stress, the modified $\sin^2\psi$ method is commonly employed for residual stress measurements [123]. In this approach, the interplanar spacing d is measured at several tilt angles (ψ), and d is plotted against $\sin^2\psi$. The total stress in the material can then be determined using the elastic theory (Equation 4), where m is the slope of the d versus $\sin^2\psi$ line, and

E and *v* represent the material's Young's modulus and Poisson's ratio, respectively. The X-rays used in this technique have a very shallow penetration depth of 5-7 μm, which is particularly advantageous for evaluating residual stresses at or near the material's surface [122].

$$\sigma_{\Phi} = \left(\frac{E}{1+\nu}\right)m \qquad (4)$$

A Stresstech Xstress G2R 3000 laboratory XRD system was used, which measures a limited θ interval of 15° rather than scanning the entire 2θ range (*Papers I-III*). A Cr Kα X-ray tube with a wavelength (λ) of 2.29 Å and a 2 mm collimator was used to measure the interplanar spacing of the crystal lattice. The collimator diameter controlled the X-ray beam size, thereby defining the measurement spot on the sample surface. The XRD system was operated at 30 kV and 9 mA. The tilt angles (ψ) ranged from -45° to +45°. Two position sensitive detectors were mounted on arc-shaped paths at a diffraction angle of 156.4° to measure the (211) lattice plane spacings using the modified $\sin^2\psi$ method, with peak positions analyzed according to Bragg's law. Strain within the crystal lattice was quantified using Xtronic software, and Hooke's law was applied with a Young's modulus of 210 GPa and Poisson's ratio of 0.3, both taken from standard tabulated values. Residual stress evaluation was performed along both the feed direction and cutting direction on the machined rings. Depth profiling extended from the surface down to 100 μm, with measurements taken at 0, 5, 10, 20, 50, and 100 μm below the machined surface. Layer removal for depth profiling was achieved via electropolishing with a salt electrolyte, while a dial gauge was used to precisely monitor the depth of material removed.

5.3.2 Vertical scanning interferometry

Surface roughness of the hard-turned surfaces was evaluated using a Sensofar S Neox 3D optical profilometer employing the coherence vertical scanning interferometry (VSI) technique (*Paper I* and *Paper III*). Interferometric microscopy, which uses low-coherence white light, provides a non-contact method for measuring surface topography [124]. Measurements were performed over a stitched area of 7.4 x 1.3 mm with 10x magnification and a uniform lateral resolution of 1.29 μm. Data analysis involved applying a second-order polynomial fit to remove form errors, followed by a spatial medium noise reduction filter with a 5 x 5 point window to minimize short wavelength noise. Three measurements were taken for each sample, and the results were averaged. The acquired data were analyzed using Digital Surf's MountainsMap software, and the roughness parameter R_a was evaluated in this study.

5.3.3 Optical microscopy

Light optical microscopy (LOM) was employed to examine the presence of WLs under different cutting conditions and tool geometries, as employed in *Papers I-V*. A Zeiss Axiovision 7 LOM system was used for this purpose. Samples were etched with Nital to enhance contrast, allowing clear distinction between white and dark microstructural layers. An overall observation of continuous or discontinuous WL formation was performed at 200x magnification, while a higher magnification of 500x was used to measure the thicknesses of WLs and DLs under various cutting conditions. However, since the relevant features, such as the WL and DL, are located at a distance of a few hundred nanometers to about 5 µm from the hard-turned surface, the spatial resolution of the LOM was not sufficient to investigate fine details, including $(Fe,Cr)_3C$ cementite morphology and the material drag zone. Additionally, stereo optical microscopy (SOM) was used to capture images of tool wear geometry on cutting inserts, as illustrated in Fig. 8 of Chapter 3. Zeiss Stereo Discovery V20 microscope was employed for this purpose. In contrast to LOM, SOM provides lower magnification but does not require additional sample preparation, making it suitable for direct observation of tool wear.

5.3.4 Scanning electron microscopy (SE/BSE imaging)

SEM employs a focused electron beam generated by a field emission gun (FEG). The emitted electrons are condensed and focused into a fine probe using magnetic condenser lenses. Beam scanning across the sample surface is achieved by means of scanning coils, which deflect the electron beam in a raster pattern over a defined area. When the coherent electron beam interacts with atoms in the sample, various signals are generated that can be detected and used for imaging purposes [125]. In this thesis, imaging was performed using secondary electron (SE) and backscattered electron (BSE) detectors. These signals originate from a pear-shaped region known as the interaction volume, whose size and shape are primarily governed by the electron probe size and beam energy. SE imaging provides detailed topographical information by detecting low-energy electrons emitted from the near-surface region of the sample as a result of inelastic interactions between the primary beam and the etched surface. Although SEs are defined as electrons with energies below 50 eV, the majority possess energies below 2-5 eV and originate from shallow depths of approximately 10-20 nm, enabling high-resolution surface imaging [126,127]. Backscattered electrons are high-energy electrons that undergo elastic scattering within the sample and provide compositional contrast based on atomic number (Z-contrast). Regions containing heavier elements (high Z) appear brighter, while areas with lighter elements (low Z) appear darker relative to the overall composition. Due to their minimal energy loss, BSEs can escape from greater depths, typically in the range of 500 nm to 1 µm. In addition to compositional contrast, BSE image contrast is influenced by crystallographic orientation through the electron channeling effect [128]. Variations in BSE yield occur for different grain orientations, when a lattice plane is aligned with the incident electron beam, electrons penetrate deeper into the material, resulting in reduced backscattering and a darker image contrast [125,127,128].

In this study, SEM was performed using a Zeiss Gemini 450 FEG-SEM. It was employed to investigate the refined microstructure of the WL, its gradient microstructural behavior in comparison with the bulk material, and the deformation and fragmentation of $(Fe,Cr)_3C$ cementite with respective to applied hard turning process parameters. SE imaging was carried out on Nital etched samples using a probe current of 500 pA, with a working distance of 5-6 mm, and an accelerating voltage of 3 kV, in order to minimize the interaction volume and enhance surface sensitivity (*Papers I-V*). BSE imaging was conducted on vibratory polished samples following nanoindentation using an accelerating voltage of 20 kV, a probe current of 5 nA, and a working distance of approximately 5 mm. This approach enabled precise identification of indentation sites within the NC grain region (*Paper V*). Figure 16 demonstrates both SE and BSE imaging to distinguish the WL from the unaffected bulk material, with BSE imaging revealing compositional contrast associated with vanadium carbides (VC). In addition, BSE imaging highlights the presence of NC grains within the WL through orientation contrast. Prior to imaging, all samples were subjected to plasma cleaning using an Evactron system for 5 minutes at 50 W within the SEM chamber to remove hydrocarbon contamination and improve image quality.

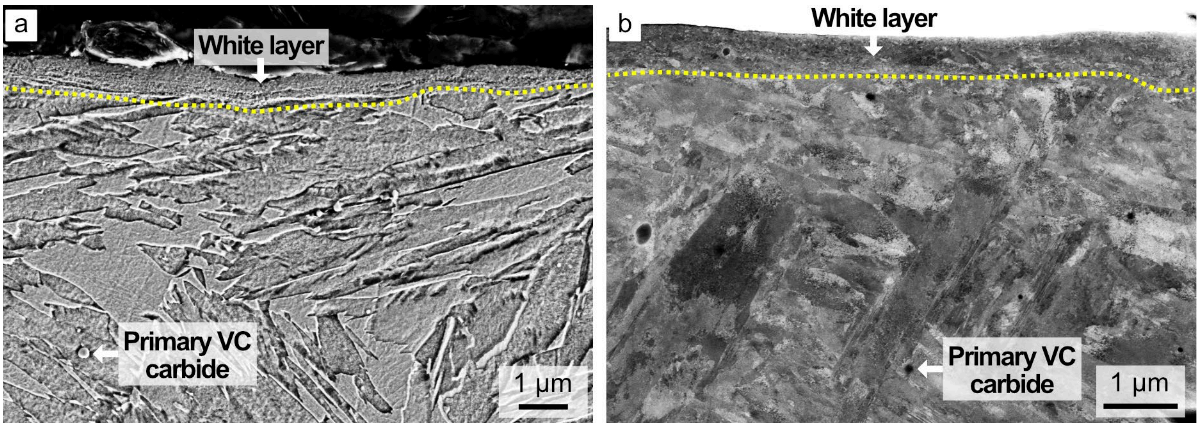

Fig. 16: (a) SE and (b) BSE image showing the white layer (WL) region after hard turning on Hybrid 60 steel.

5.3.5 Scanning transmission electron microscopy

TEM is an advanced characterization technique in which a high-energy electron beam is transmitted through an ultra-thin specimen, typically less than 100 nm in thickness. Imaging can be performed using a parallel electron beam in conventional TEM mode or a focused, rastered beam in scanning transmission electron microscopy (STEM) mode, which incorporates elements of both TEM and SEM [129]. Conventional TEM typically operates at accelerating voltages in the range of 60-300 kV. In STEM mode, imaging is achieved by scanning a focused electron probe across the specimen and collecting transmitted electrons at each pixel using dedicated detectors. The most commonly used STEM detector is a radially segmented annular semiconductor detector consisting of a central bright-field (BF) segment surrounded by annular dark-field (ADF) segments [129,130]. When the incident electron beam interacts with the specimen, multiple scattering events occur, generating various signals. The BF detector collects unscattered and low-angle forward-scattered electrons, typically below 15 mrad, while the ADF detector collects electrons scattered at medium to high angles, generally between 20 and 100 mrad [131].

In addition to TEM-based STEM, transmission imaging can also be performed in a SEM equipped with an electron-transparent sample stage and transmission detectors. In this configuration, SEM operates in transmission mode at significantly lower accelerating voltages, typically between 0.1 and 30 kV. This technique is commonly referred to as low-keV STEM, transmission scanning electron microscopy (TSEM), or STEM-in-SEM, the latter terminology being used throughout this thesis to distinguish it from conventional STEM performed in a TEM. Apart from the lower accelerating voltage (≤ 30 kV), the principal difference between STEM-in-SEM from STEM lies in the absence of a projection lens system [130]. Consequently, the camera length in STEM-in-SEM cannot be adjusted electronically and instead requires physical movement of either the specimen or the detector along the optical axis [132]. In STEM-in-SEM, BF and ADF detectors integrate the intensity of transmitted electrons as a function of scattering angle, producing images comparable to those obtained in conventional STEM. However, due to increased beam broadening associated with the lower accelerating voltages, STEM-in-SEM generally exhibits reduced spatial resolution and contrast compared to STEM [133]. Despite these limitations, STEM-in-SEM remains a powerful transmission imaging technique for applications where atomic-scale resolution is not required. Figure 17 compares BF images acquired using STEM-in-SEM and STEM from the same region of a FIB lift-out specimen, illustrating the similarities and differences between the two approaches.

Electron-transparent lamellae prepared by FIB lift-out were examined using BF STEM mode in an FEI Titan 80–300 TEM operated at an accelerating voltage of 300 kV (*Paper V*), as well as using an BF annular STEM (aSTEM) detector in a Zeiss Gemini 450 FEG-SEM operated in STEM-in-SEM mode at 30 kV and a probe current of 500 pA (*Papers III-V*). Prior to imaging, the FIB-prepared lamellae were subjected to plasma cleaning using an Evactron system for 5 minutes at a power of 50 W within the SEM chamber to remove hydrocarbon contamination and improve image quality.

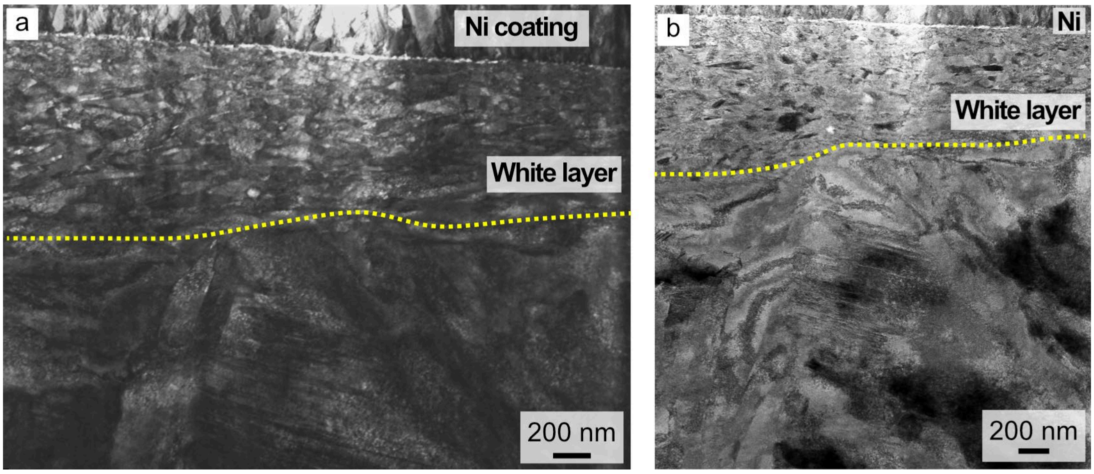

Fig. 17: (a) BF STEM-in-SEM and (b) BF STEM image showing the white layer (WL) region after hard turning in Hybrid 60 steel.

5.3.6 Electron backscattered diffraction and transmission Kikuchi diffraction

Crystallographic orientation mapping can be performed using EBSD and TKD techniques. Both methods utilize the same detector system and are based on identical diffraction principles. However, EBSD analyzes electrons scattered from the specimen surface, whereas TKD analyzes electrons transmitted through an electron-transparent sample, as shown in Fig. 18. In EBSD, the specimen is typically tilted by 70° relative to the horizontal plane to enhance the yield of BSE reaching the detector. When the incident electron beam interacts with the sample surface, a fraction of the electrons undergo inelastic scattering, losing a small amount of energy. Some of these electrons subsequently satisfy the Bragg diffraction condition,

$$\lambda = 2d_{hkl}sin\theta_{hkl} \qquad (5)$$

where λ is the electron wavelength, θ_{hkl} is the Bragg diffraction angle and d_{hkl} is the corresponding interplanar spacing. When the condition described by Equation 5 is satisfied, diffraction occurs [134]. For each (hkl) plane, the electrons are diffracted into two Kossel cones with angles of $90-\theta_{hkl}$ and $90+ \theta_{hkl}$. Due to the small θ_{hkl} involved and the close proximity of the detector, these cones appear as pairs of nearly parallel lines, known as Kikuchi lines, on the phosphorescent screen. Each pair of lines constitutes a Kikuchi band, whose angular width is equal to twice the θ_{hkl}, allowing the determination of the corresponding interplanar spacing using Equation 5. The collection of Kikuchi bands forms an electron backscatter diffraction pattern (EBSP), from which the crystallographic orientation at a specific point can be determined. EBSPs acquired at each measurement point are processed using a Hough transformation, in which each Kikuchi band is converted into a point in the two-dimensional Hough space. This transformation facilitates reliable band detection and indexing by automated software [134]. EBSD provides information on phase identification, crystallographic and grain boundary misorientation. In the present work, EBSD was employed to characterize the initial bulk microstructure, as the NC grains within the WL regions could not be resolved. The spatial resolution of EBSD is fundamentally limited to ~20 nm in dense materials such as steels, although in most practical applications it is typically restricted to 50-100 nm. This limitation arises primarily from the high specimen tilt angle, which increases the effective electron interaction volume by spreading the beam laterally across the surface. As a result, EBSD is generally unsuitable for characterizing nanograined microstructures in severely deformed metals. Furthermore, high lattice distortion associated with SPD processes presents additional challenges in obtaining high-quality, indexable diffraction patterns from NC grains [135].

To overcome the spatial resolution limitations of conventional EBSD, transmission EBSD commonly referred to as TKD was introduced by Keller and Geiss in 2010 [136]. In TKD, an electron-transparent specimen is mounted horizontally at the level of the EBSD detector, and Kikuchi patterns are generated by electrons transmitted through the sample rather than diffracted from the surface. This geometry significantly reduces the interaction volume, enabling spatial resolutions as fine as 2 nm [137,138]. The improved resolution in TKD primarily results from vertical electron beam penetration, in contrast to the extensive lateral beam spreading observed in EBSD due to the high specimen tilt [138]. Higher accelerating voltages, typically in the range of 25-30 kV, are preferred in TKD to increase the fraction of transmitted electrons, enhance pattern intensity, reduce beam broadening, and improve spatial resolution [135,136]. Despite these advantages, TKD analysis of heavily deformed steels containing NC grains, such as WLs, remains challenging. Factors including sample thickness variations, curtaining effects introduced during FIB lift-out preparation, and high dislocation densities can significantly degrade Kikuchi pattern quality [139–141]. In severely deformed regions, overlapping and blurred diffraction patterns often result in low indexing rates due to reduced band contrast [142]. To address these limitations, pattern matching indexing methods have been developed as a complement to conventional Hough transform indexing. This approach compares experimentally acquired Kikuchi patterns with dynamically simulated patterns using image correlation techniques, enabling improved indexing of patterns that are otherwise difficult to resolve [143–146]. In the present study, the integration of TKD with pattern matching indexing significantly enhanced the accuracy and reliability of crystallographic orientation measurements in highly strained NC grains, as shown in Fig. 19.

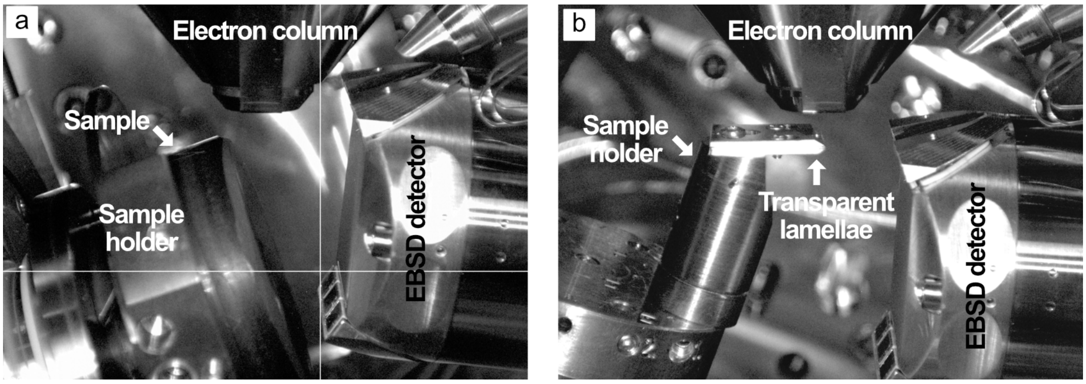

Fig. 18: In-chamber image showing the set up for (a) EBSD analysis and (b) TKD analysis.

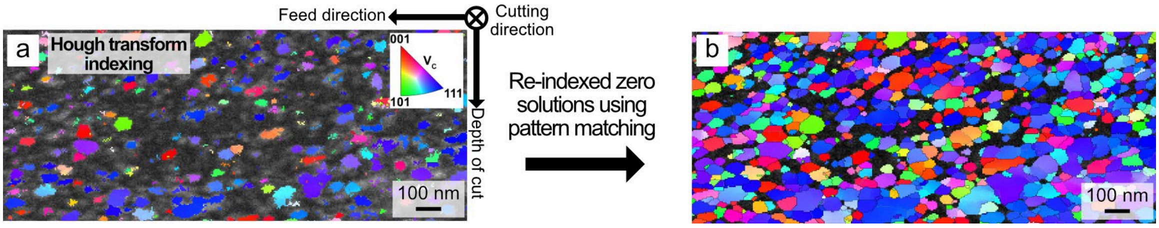

Fig. 19: (a)TKD IPF orientation map overlaid on band contrast image, obtained using Hough transform indexing with a hit rate of 18%. (b) IPF orientation map generated using the pattern matching technique with an indexing rate of 71% on NC grains.

EBSD data from the bulk material were acquired using a Zeiss Gemini 450 FEG-SEM equipped with an Oxford Instruments Symmetry detector (*Paper IV* and *Paper V*). Data acquisition was performed using AZtec 6.2 software (Oxford Instruments Nanoanalysis) at an accelerating voltage of 20 kV, and a probe current of 12 nA. The acquired EBSD maps were processed and visualized using AZtecCrystal 3.3 software, where a single iteration of the AutoClean function was applied for noise reduction and data cleaning. TKD measurements were performed in off-axis configuration on the thinnest regions of the FIB lamellae using the same Zeiss Gemini 450 SEM equipped with an Oxford Symmetry detector (*Paper IV* and *Paper V*). A setup with an accelerating voltage of 30 kV, a beam current of 5 nA, and a working distance of 4-5 mm was used. Data acquisition was conducted using AZtec 6.2 software (Oxford Instruments Nanoanalysis), with drift and shadow correction applied during acquisition. Each TKD pattern was initially analyzed using a conventional Hough transform based approach for Kikuchi band detection. All diffraction patterns were subsequently stored and post-processed using the "MapSweeper" pattern matching functionality in AZtecCrystal 3.3 software to improve indexing reliability. The detailed procedure for TKD pattern matching analysis was described in *Paper IV*. Prior to EBSD and TKD analysis, plasma cleaning was performed.

5.3.7 Atom probe tomography

APT is a high resolution analytical technique capable of three-dimensional characterization with sub-nanometer spatial resolution (<0.3 nm), enabling the visualization and analysis of millions of atoms within a specimen. APT analysis begins with the preparation of a needle-shaped specimen using FIB lift-out technique, resulting in a tip radius of ~50 nm. During analysis, atoms are field evaporated from the needle-shaped specimen in the form of positively charged ions. These ions are subsequently detected, and both their mass-to-charge ratio and spatial origin within the specimen are determined. The collected data are then reconstructed into a three-dimensional atomic map, providing detailed insight into the chemical distribution within the analyzed volume. To enable field evaporation, the specimen is maintained in an ultra-high vacuum environment at cryogenic temperatures, typically between 30 and 70 K, while a high positive direct current (DC) voltage is applied between the specimen and a counter electrode. Controlled field evaporation is initiated by applying either voltage or laser pulses, which ionize atoms at the specimen surface. The resulting ions are accelerated by the electric field toward a two-dimensional position-sensitive detector. The time-of-flight of each ion is measured as the interval between the applied pulse and the detection event, allowing determination of the ion's mass-to-charge ratio. Because the field evaporation occurs sequentially from the outermost atomic layers of the tip, ion trajectory models are used to trace backward each detected ion to its original position on the specimen surface. Through this process, the specimen is reconstructed atom by atom within a three-dimensional virtual space, enabling quantitative analysis of local chemical composition at near-atomic resolution. References for this section are [147–149].

In this thesis, APT was employed primarily for the investigation of behavior of nanoscale precipitates in Hybrid 60 steel after hard turning (*Paper V)*. APT analyses were performed using a CAMECA LEAP 6000 XR operated in laser-pulse mode. Measurements were conducted at a specimen temperature of 50 K, with a laser pulse energy of 30 pJ, a pulse repetition rate of 158 kHz, and a target detection rate of 0.4%. During data reconstruction, an image compression factor of 1.55 and a k-factor of 5.0 were applied. Data reconstruction and analysis were carried out using AP Suite 6.3 software. Nanoscale precipitates were visualized using iso-concentration surfaces, while their compositional profiles were quantified using proximity histograms (proxigrams).

5.3.8 Nanoindentation

Nanoindentation is a technique used to evaluate local mechanical properties using a diamond Berkovich indenter. In this thesis, two nanoindentation equipment's were employed, both operating on the same fundamental principle. The method is based on contact elastic-plastic mechanics, where the hardness (*H*) is calculated as the ratio of the maximum applied load (P_{max}) to the projected contact area (A_c) [150].

$$H = \frac{P_{max}}{A_c} \qquad (6)$$

Paper III

The WLs generated on the hard-turned surface of AISI 52100 steel exhibited thicknesses in the range of 1-3 µm. Nanoindentation was performed on both M-WLs and T-WLs to investigate their hardness using a NanoTest Vantage nanoindenter from Micro Materials Ltd. Indentations were performed under load-controlled conditions with a maximum applied load of 4 mN. Each indentation cycle consisted of a loading time of 10 s, a dwell time of 10 s at the maximum load, and an unloading time of 10 s. Thermal drift correction was enabled, with an additional 30 s of data collection to ensure measurement stability. Hardness values were determined from the load-displacement curves using the Oliver-Pharr method, as implemented in the Micro Materials analysis software [150].

Paper V

Nanoindentation measurements of the hard-turned affected regions in Hybrid 60 steel were performed using a Femto Tools FT-I04 nanoindenter. Indentations were conducted in displacement-controlled mode employing the continuous stiffness measurement (CSM) technique, with a maximum penetration depth of 100 nm. A dynamic oscillation of 3 nm at a frequency of 150 Hz was superimposed on the loading segment. The CSM approach enables continuous measurement of contact stiffness during loading, allowing nanohardness to be evaluated as a function of indentation depth. This capability is particularly important given that the NC grain regions are only a few hundred nanometers thick. Prior to testing, the indenter tip geometry was calibrated to determine the area function using the Oliver-Pharr method on a fused silica reference sample through standard indentation procedures [150]. Hardness values were subsequently analyzed using the Femto Tools analysis suite.

CHAPTER 6

Summary of Appended Papers

This chapter summarizes and discusses the findings reported in the appended papers. Section 6.1 presents a consolidated discussion of the results from *Papers I-III*, which correspond to RQ1. Section 6.2 focuses on the microstructural evolution of the M-WL, building on the results from *Paper III and Paper IV* to answer RQ2. Finally, section 6.3 investigates the formation of WLs and the behavior of nanoprecipitates in hard-turned Hybrid 60 dual-hardening steel, based on the results from *Paper V*, thus answering RQ3.

6.1 Process-structure-property relationship of WLs

6.1.1 Influence of process parameters and tool geometry

The primary objective of this study is to achieve the desired functional surface integrity in hard-turned AISI 52100 steel by enhancing compressive residual stresses, reducing surface roughness, and promoting the formation of beneficial M-WL. To meet these objectives, key process parameters such as V_c, f, a_p, P, tool geometry parameters Y, and VB were systematically varied using a 64 full factorial design of experiments. This experimental approach enabled a comprehensive assessment of their individual and combined effects on WL formation. The initial focus was placed on evaluating the influence of these parameters on residual stresses and surface roughness. Based on the resulting trends, optimized parameters were identified and subsequently examined in greater detail with respect to their influence on WL formation.

In general, as observed from *Paper I and Paper III*, higher V_c and f led to a reduction in surface compressive residual stresses, primarily due to increased cutting temperatures and associated thermal effects. Further, an increase in f resulted in higher compressive stresses in the subsurface region, attributed to elevated cutting forces that intensify plastic deformation beneath the machined surface. An increase in Y was found to enhance both surface and subsurface compressive stresses. This effect is associated with the development of more negative effective rake angles, which increase cutting forces and promote greater material deformation and flow into the machined surface

[151]. Moreover, higher *P* further improved surface compressive stresses, particularly for specimens machined at low *f*. Regarding R_a, lower *f* consistently produced smoother surfaces due to reduced spacing between surface peaks and valleys generated by feed marks. This behavior is associated with the formation of helicoid furrows arising from the relative motion between the cutting tool and the workpiece. At higher V_c, increased surface temperatures promote material softening, which contributes to a reduction in R_a. As described by Equation 2 in Section 3.3.1, R_a increases directly with *f*, a relationship that is clearly reflected in the experimental results.

Based on the residual stress analysis, a *Y* of 35°, a *f* of 0.05 mm/rev, a V_c of 60 m/min, and a *P* of 150 bar were identified as optimal for achieving favorable surface and subsurface compressive residual stresses. In terms of R_a, a *f* of 0.05 mm/rev resulted in significantly lower R_a values compared to 0.2 mm/rev. The a_p showed no significant effect on either residual stresses or R_a and was therefore set to a higher value of 0.2 mm to improve productivity. Based on this screening, four machining conditions were selected, as summarized in Table 4. The parameter P1, which favors low R_a and high compressive residual stresses, was compared with a parameter P2, which leads to surface tensile residual stresses and higher R_a values, in order to further investigate their effects on microstructural evolution. In line with RQ 1 outlined in Chapter 1, *VB* was also considered, recognizing its inevitable progression during hard turning. The influence of a *VB* of ~0.2 mm on surface integrity was examined under the selected machining conditions (P3 and P4).

Table 4. Selected parameters to understand their effect on the microstructure.

Parameters	Cutting speed (*Vc*)	Feed rate (*f*)	Tool wear (*VB*)
P1	60 m/min	0,05 mm/rev	0 mm
P2	110 m/min	0,2 mm/rev	0 mm
P3	60 m/min	0,05 mm/rev	~ 0,2 mm
P4	110 m/min	0,2 mm/rev	~ 0,2 mm

Figure 20a shows the residual stress profiles dominated by mechanical effects at low cutting speeds and low feed rates (P1 and P3), while Fig. 20b highlights thermally dominated residual stress profiles associated at high cutting speeds and high feed rates (P2 and P4). *VB* was observed to amplify these effects, leading to significantly higher compressive stresses under mechanically dominated conditions (P3) and pronounced tensile stresses under thermally dominated conditions (P4). In all cases, the magnitude of surface compressive residual stresses measured along the cutting direction was lower than that in the feed direction. This behavior is attributed to higher cutting forces and increased frictional heating along the cutting direction compared to the feed direction [152].

The R_a values and the surface topography maps for the selected machining conditions are shown in Fig. 20c,d. The dominant influence of *f* on R_a is evident across all conditions. At a low *f* of 0.05 mm/rev and a V_c of 60 m/min, R_a values of 0.11 µm and 0.19

µm were measured for the fresh (P1) and worn (P3) inserts, respectively. Increasing both *f* and V_c led to a substantial rise in surface roughness, with R_a values of 0.59 µm for P2 and 1.19 µm for P4. The degradation in surface quality observed with the worn insert is attributed to irregularities developing on the tool flank face as wear progresses. Nevertheless, surfaces machined at a low *f* with a worn insert exhibited lower roughness than those machined at a high *f* using a fresh insert, underscoring the dominant role of *f* in controlling R_a.

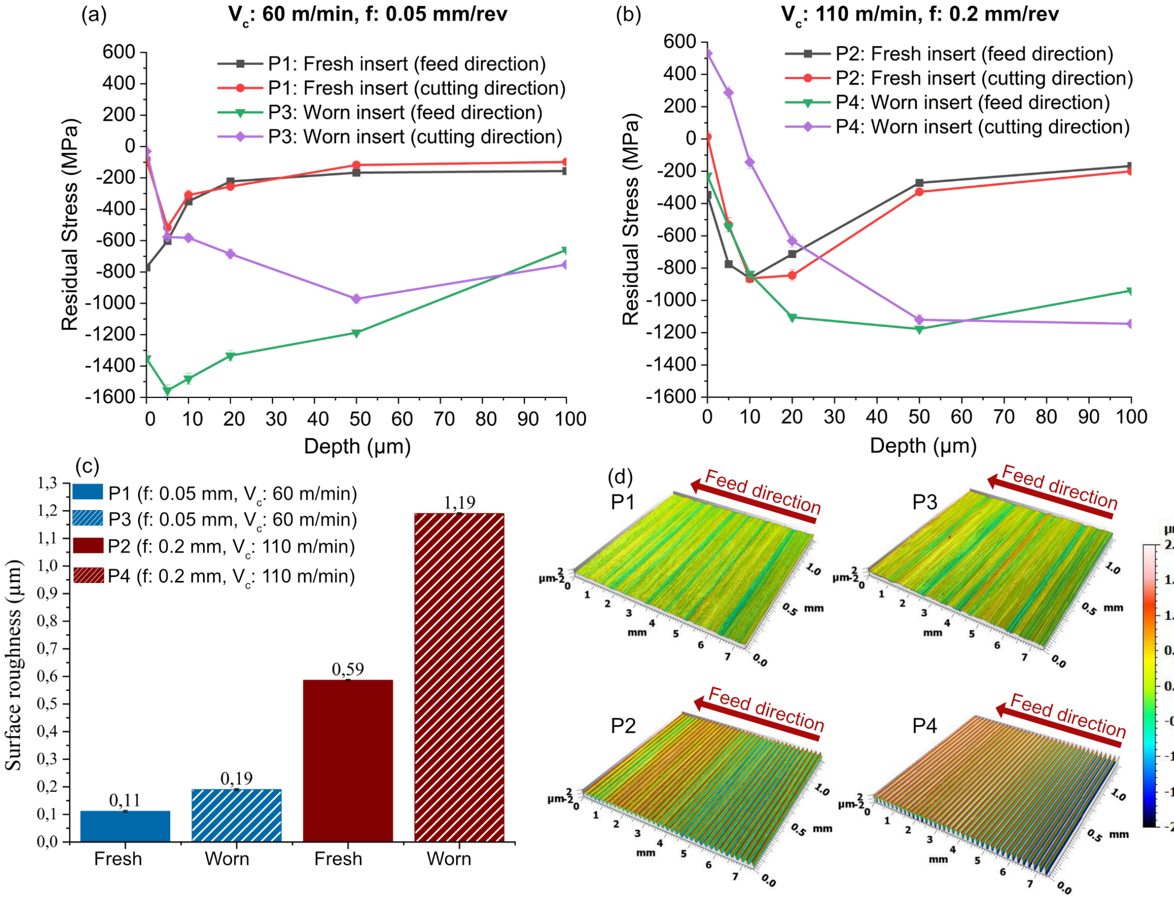

Fig. 20: Residual stress profiles for (a) V_c: 60 m/min, f: 0.05 mm/rev, (b) V_c: 110 m/min, f: 0.2 mm/rev with constant parameters a_p: 0.2 mm, Y: 35°, P: 150 bar parameters and the worn insert corresponds to VB: ~0.2 mm. (c) R_a values for the investigated hard turning conditions. (d) Surface topography maps of samples machined with the P1, P2, P3, and P4 parameters [153].

6.1.2 Microstructure and mechanical behavior

Following the identification of suitable machining parameters based on residual stresses and surface roughness, the surface microstructure and nanohardness response of the hard-turned specimens were investigated to understand the WL formation. Based on the LOM observations reported in *Paper III*, machining conditions P1 and P3 resulted in the formation of M-WL, whereas conditions P2 and P4 led to the formation of T-WL. The distinction between M-WL and T-WL in LOM images was primarily based on the presence of the DL beneath the WL. For the fresh insert and high cutting conditions (P2), the DL was observed to be significantly thinner than that formed using a worn insert (P4). This difference is attributed to increased flank wear, which enhances tool-workpiece friction and consequently raises the local temperature, extending thermal effects into the subsurface region and resulting in a thicker DL beneath the WL. To enable accurate quantification of the WL and DL thicknesses for all four machining conditions, imaging with SE-SEM was employed. The SE-SEM analysis revealed that, when using a fresh insert, the average WL thickness for both M-WL (P1) and T-WL (P2) ranged between 0.7 and 1.5 μm, with noticeable variation along the feed direction. The corresponding DL thickness beneath the T-WL formed with a fresh insert (P2) was ~0.5 μm in thickness. In contrast, the use of worn inserts resulted in a substantial increase in WL thickness, reaching ~2-3 μm for both M-WL and T-WL. Moreover, the DL associated with the T-WL formed using a worn insert (P4) had a thickness of 3-4 μm. Given the greater thickness and more pronounced features of WLs generated by worn tools, subsequent microstructural and nanohardness analyses were focused on these regions.

The SE-SEM images presented in Fig. 21a show that the M-WL is formed predominantly through intense plastic deformation, characterized by an elongated and fragmented refined microstructure along with the feed direction. Fragmented, nearly spherical $(Fe,Cr)_3C$ cementite particles are evident within the M-WL, as highlighted by the yellow circles. Beneath the M-WL, a plastically deformed material drag zone with a thickness of approximately 1 μm is observed. In this region, grains are elongated along the feed direction but do not exhibit the same degree of fragmentation as in the WL. Figure 21b illustrates the morphology of the T-WL formed at conditions dominated by thermal effects, accompanied by a distinct DL beneath the WL. The clear differences in morphology between the M-WL and T-WL indicate fundamentally different formation mechanisms driven by predominant mechanical and thermal influences, respectively. To further characterize these differences, nanoindentation measurements were performed to assess the local hardness variations within the WLs and adjacent regions. The nanohardness profiles for M-WL and T-WL are shown in Fig. 21c,d, respectively. Both WL types exhibit significantly higher hardness than the bulk material, with increases of 26% for the M-WL and 27% for the T-WL. However, notable differences were observed in the underlying regions. The material drag zone beneath the M-WL had a 7% higher hardness than the bulk material, whereas the DL beneath the T-WL showed a 16% lower in hardness than the bulk. The combination of higher hardness in the M-WL and material drag zone, increased compressive residual stresses and lower surface roughness, suggests that M-WL formation is more favorable for functional performance than T-WL formation. These microstructural and nanohardness characteristics are directly correlated with the selected process parameters and the associated thermo-mechanical interactions (TMIs) during hard turning.

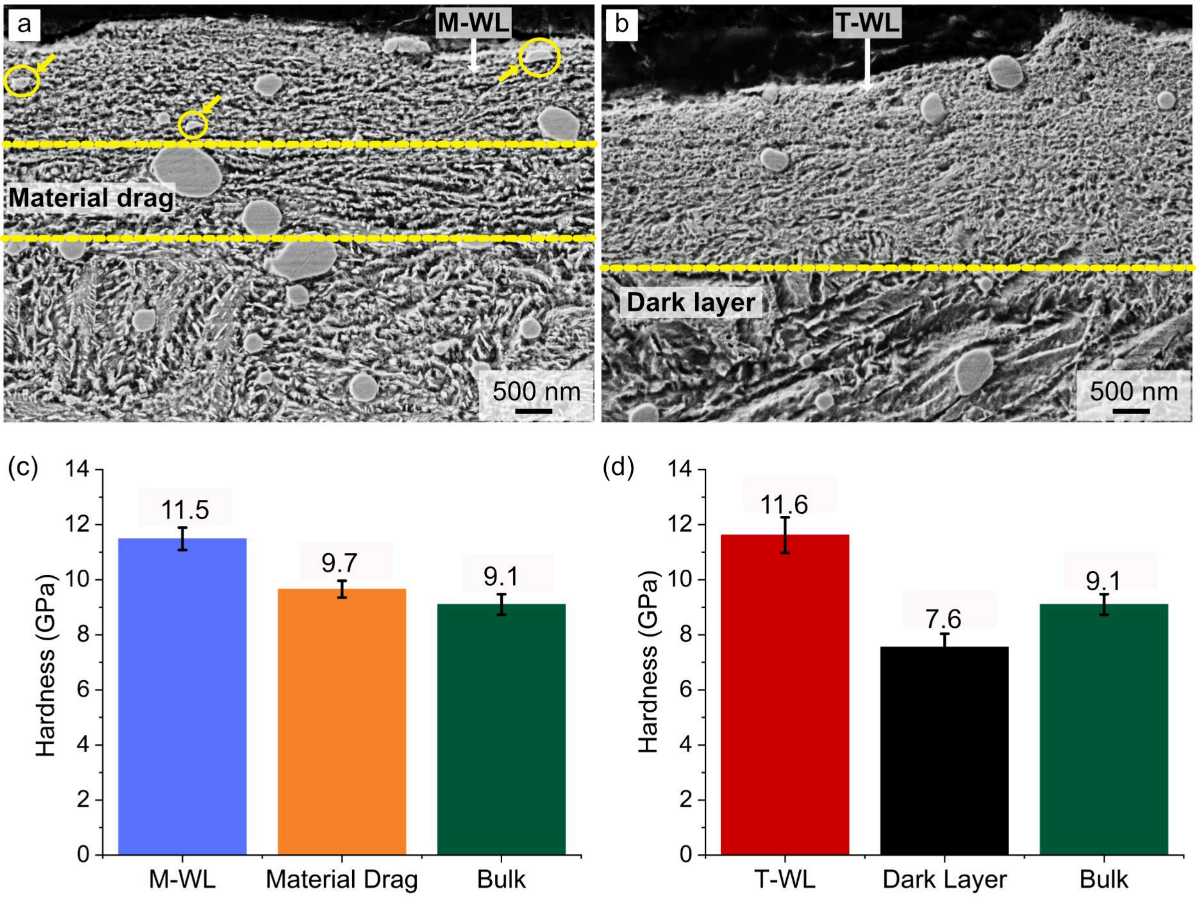

Fig. 21: SE-SEM images showing (a) M-WL characterized by a fine, fragmented, and elongated grain structure, yellow circles highlight fragmented, nearly spherical cementite particles, with a material drag zone present beneath the WL. (b) T-WL exhibiting a fine microstructural morphology accompanied by a distinct DL beneath the WL. Corresponding nanohardness values for (c) the M-WL and underlying material drag zone and (d) T-WL with the underneath DL [153].

6.1.3 Role of initial retained austenite content

The primary objective of this part of the study is to elucidate the role of RA in the formation of M-WL and T-WL. As demonstrated in section 6.1.1 (Fig. 20), M-WL formation results in superior surface integrity compared to T-WL. *Paper II* specifically addresses the influence of different initial RA contents (<2%, 12%, and 25%) on WL formation under hard turning conditions. The machining parameters employed in this investigation are detailed in Section 5.1.

Residual stress profiles measured along the cutting direction for varying RA contents and cutting speeds are reported in *Paper II*. For both cutting speeds investigated (V_c: 60 m/min and 260 m/min), specimens with higher RA contents (12% and 25%) exhibited reduced surface compressive residual stresses when machined with a fresh insert and developed surface tensile residual stresses when machined with a worn insert. At the higher cutting speed of 260 m/min, worn inserts generated pronounced surface tensile stresses in the range of 600-800 MPa, primarily due to elevated surface temperatures. In contrast, specimens with <2% RA showed significantly lower surface tensile stresses of ~200 MPa under the same V_c and worn insert conditions.

To clarify the observed reduction in surface compressive stresses for fresh inserts and the increase in surface tensile stresses for worn inserts in specimens with 12% and 25% RA relative to those with <2% RA, a detailed microstructural analysis was conducted. The corresponding microstructures, presented in Fig. 22, are consistent with the measured residual stress profiles. The high tensile stresses observed in the higher RA content specimens correlate with the formation of T-WLs. Conversely, under fresh insert conditions at a V_c of 60 m/min, all specimens exhibited higher surface compressive stresses associated with the formation of M-WLs. An increase in RA content was found to promote T-WL formation under conditions of increased tool wear and higher cutting speed. Although T-WL formation was also observed in specimens with <2% RA at 260 m/min using a worn insert, the resulting WL was significantly thinner compared to those formed in specimens with higher RA content, as shown in Fig. 22a in comparison with Fig. 22b,c.

The influence of specific cutting pressure on the austenitization temperature is a key factor governing these observations. Since austenite (FCC) has a higher atomic packing density than tempered martensite (BCC), increased cutting pressure can effectively lower the austenitization temperature, thereby facilitating phase transformation during machining. Additionally, the relatively low stacking fault energy of austenite suppresses DRV and promotes CDRX, which further contributes to T-WL formation under thermally dominated conditions. Nevertheless, a comprehensive understanding of the mechanisms by which RA content influences WL formation and its final microstructural characteristics requires a more detailed analysis of calculating the austenitization temperatures. Such an investigation should explicitly account for the combined effects of heating rate, plastic strain, contact pressure, and carbon concentration during hard turning.

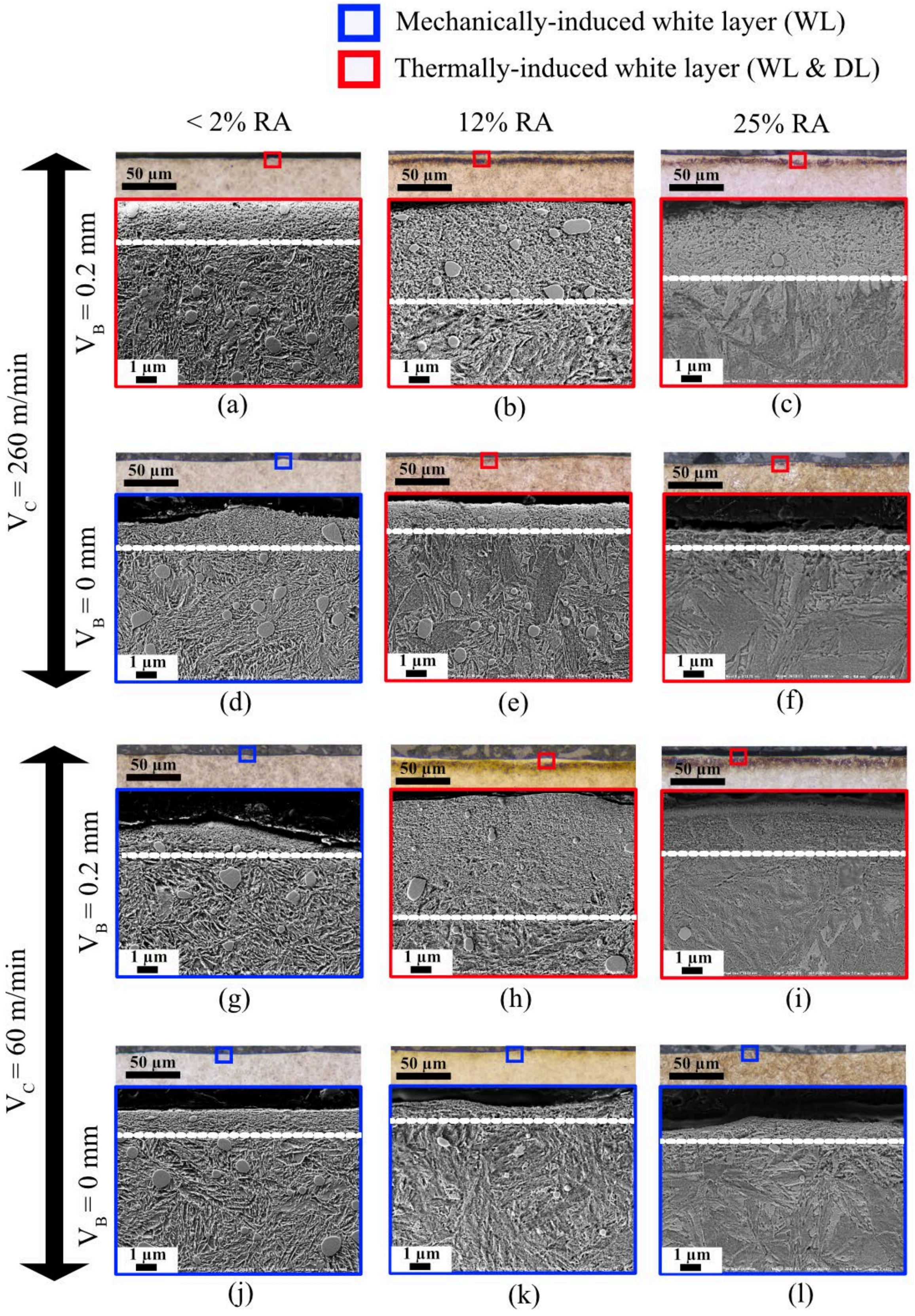

Fig. 22: LOM and their respective SE-SEM images of samples machined under different cutting conditions. The white dashed lines denote the boundary between the WL and the bulk for the M-WL and the boundary between the WL and DL for the T-WL [39].

6.2 Formation mechanism of M-WL

Having established the process-structure-property relationships governing the formation of both M-WL and T-WL, the superior surface integrity associated with M-WL highlights its potential for producing process-induced NC surfaces suitable for demanding engineering applications. However, the fundamental mechanisms responsible for the grain refinement leading to the NC structure require further clarification. Accordingly, the primary objective of this section is to elucidate the gradient microstructural evolution from the unaffected bulk material to the hard-turned surface and further to compare this evolution with that observed in the well-established T-WL, as reported in *Paper III* and *Paper IV*.

BF STEM-in-SEM image obtained from a FIB lift-out specimen of the M-WL is shown in Fig. 23a. During hard turning under the selected processing conditions (P1 and P3), the initial lath martensitic microstructure is subjected to intense SPD, as schematically indicated by the black dashed line in Fig. 24a. As revealed by the SE-SEM observations in Fig. 21a, a key microstructural feature motivating the present analysis is the identification of a distinct material drag region beneath the M-WL. Within this material drag region of ~1 μm thickness, the original martensitic laths with a width of ~300-400 nm progressively transforms into multiple elongated lamellar grains with an average thickness of ~30-50 nm. These lamellar grains are characterized by a high density of both GNBs and IDBs, as clearly shown in Fig. 23e. This structural refinement known as grain subdivision process represents the initial stage of M-WL formation. To further confirm the presence and nature of GNBs and IDBs within the lamellar grains, quantitative TKD with pattern matching analysis was performed. As illustrated in Fig. 24b, misorientation analysis was conducted across a representative lamellar grain. The point-to-point misorientation profile (black line) shown in Fig. 24c indicates the presence of subgrain structures bounded by IDBs and characterized by low-angle grain boundaries (LAGBs). In contrast, the point-to-origin misorientation profile (red line) indicates a cumulative misorientation of 13°. The dark boundary traces surrounding the lamellar grain in Fig. 24b correspond to GNBs, which are characterized by HAGBs. While GNBs exhibit either low or high-angle GBs, increased strain and strain rates typically drive them toward HAGBs, while IDBs remain as LAGBs. As strain gradients intensifies towards the hard-turned surface of ~1-3 μm thickness, the grain subdivision process progresses further, ultimately resulting in the formation of distinct, rectangular, elongated NC grains, as shown in Fig. 23c. While the traditional DRV mechanism suggests that NC grains are primarily subgrains with LAGBs formed by dislocation rearrangement, HAGBs were observed in the NC grains near the surface, in this study, as detailed in *Paper IV*. The formation of such NC grains with HAGBs within the M-WL is attributed to mechanically assisted triple junction motion, a DRV mechanism operating under extreme deformation conditions.

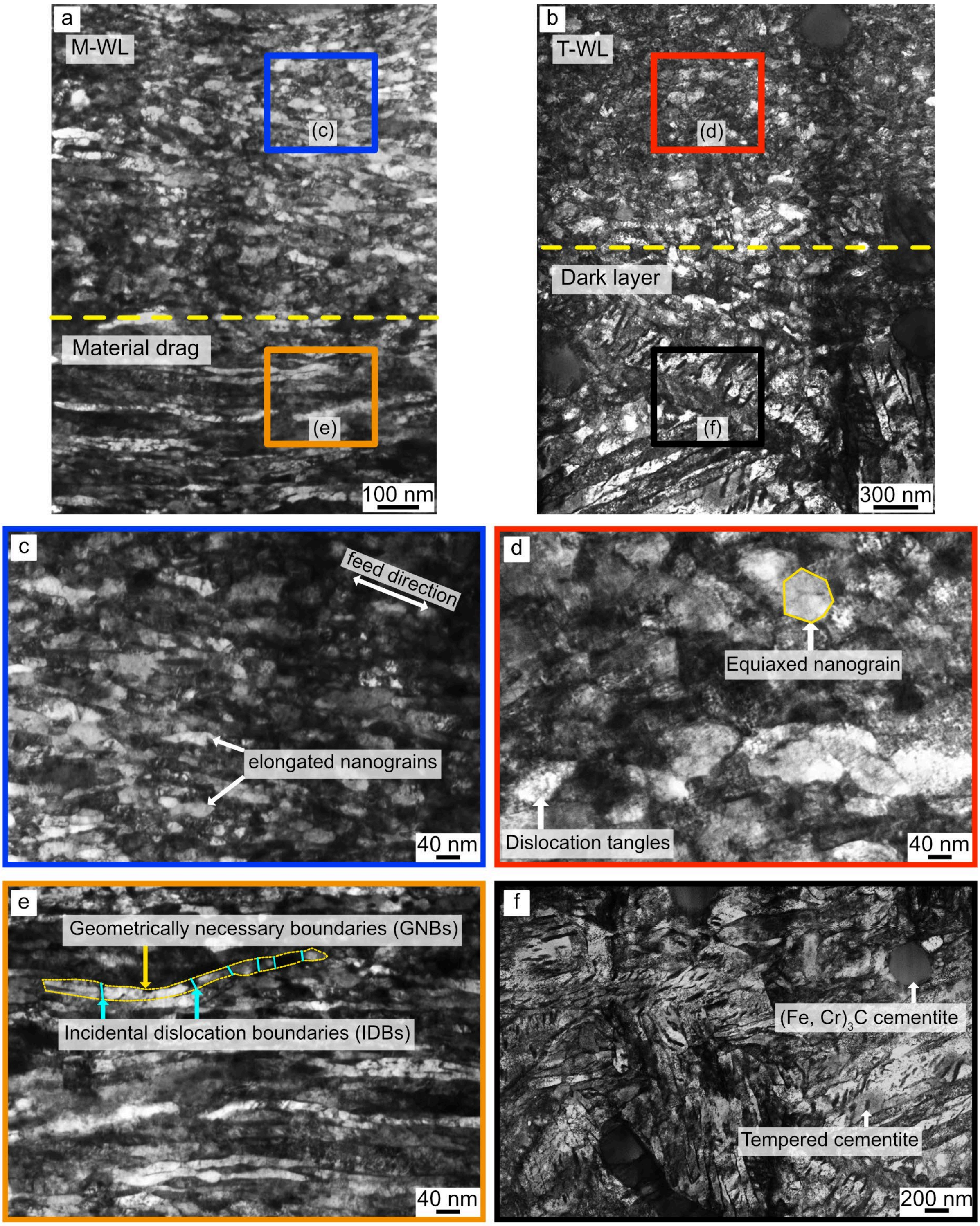

Fig. 23. BF STEM-in-SEM images showing (a) M-WL with an underlying material drag region. (b) T-WL with a DL beneath. (c) NC grains within M-WL. (d) NC grains within T-WL. (e) Grain subdivision within a lamellar grain in the material drag zone beneath the M-WL, highlighting the presence of GNBs and IDBs. (f) Over tempered martensite in the DL beneath the T-WL, containing nearly spherical $(Fe, Cr)_3C$ cementite precipitates and nano-sized tempered cementite [153].

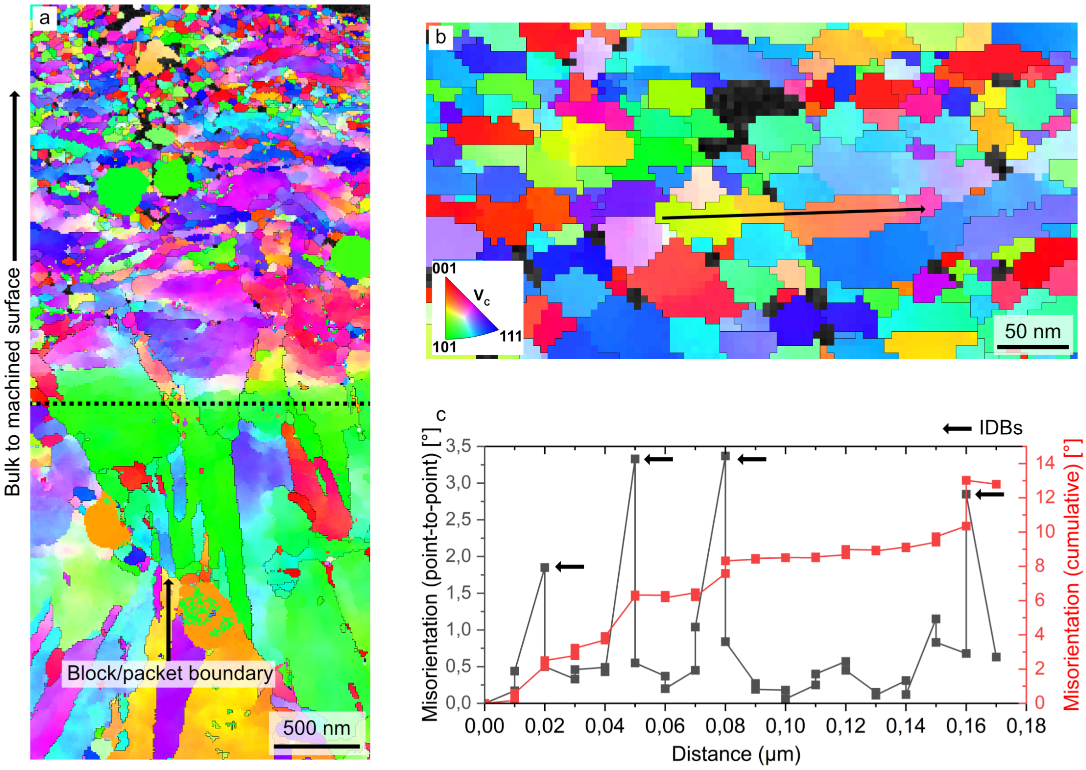

Fig. 24. Revealing the grain subdivision mechanism using TKD pattern matching analysis. (a) Effect of hard turning on the orientation of the original block/packet martensitic structure, highlighted by black dashed lines. (b) Rectangular lamellar grain within the material drag region, exhibiting varying IPF orientations. (c) Misorientation point-to-point and cumulative line profile analysis corresponding to the black arrow in (b) with the point-to-point analysis indicating the low angle IDBs in the lamellar grain.

The high-magnification BF STEM-in-SEM image shown in Fig. 25a shows the presence of Y-type triple junctions (indicated by red arrows) and an H-type junction (indicated by a yellow arrow) within the M-WL. During deformation, the lamellar grains formed through grain subdivision in the material drag region experience localized shear and subsequently break apart due to Y-type triple junction migration, as shown in Fig. 25b. This migration process effectively replaces two lamellar boundaries with a single boundary, thereby eliminating associated IDBs and dislocations in the affected region while preserving the rectangular morphology of the NC grains. As a result, the stored strain energy within the deformed material is reduced, which is characteristic of a DRV process. While similar triple junction motion assisted DRV mechanisms have been reported in cold rolled aluminum [115], where lamellar grain thicknesses are typically on the order of ~300 nm, the present study shows lamellar grains with widths of ~30 nm. The substantially finer scale of these microstructural features are primarily due to the hard turning induced TMIs.

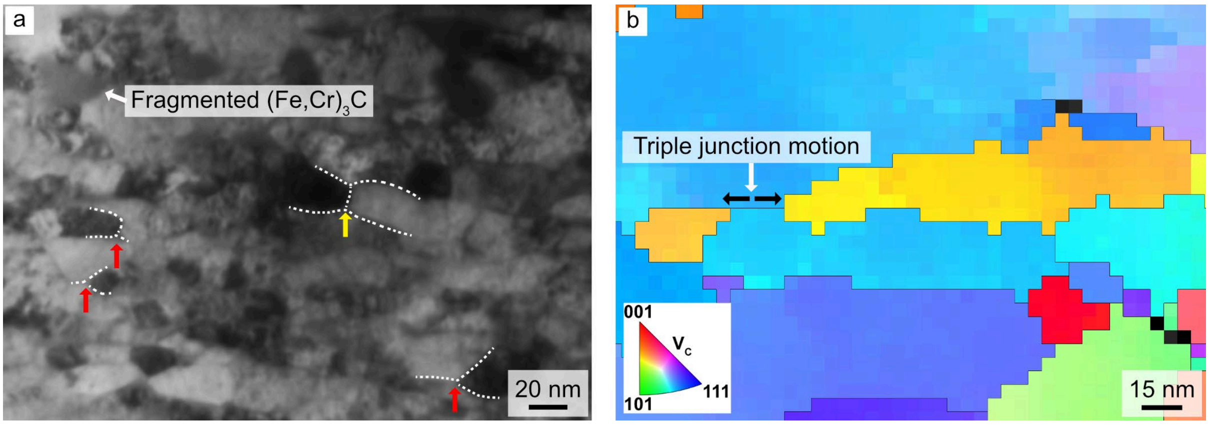

Fig. 25. Dynamic recovery (DRV) assisted triple junction motion in the M-WL. (a) High-magnification BF STEM-in-SEM image of the NC grains in the M-WL region, revealing H-type (yellow arrow) and Y-type (red arrow) junctions. (b) TKD pattern matching analysis indicating DRV assisted triple junction motion (Y-junction), indicated by black arrows.

In contrast to the M-WL, a key observation in the T-WL is the absence of lamellar grains, indicating that the grain subdivision mechanism dominant in M-WL formation is not operative in the T-WL. Instead, as revealed by the BF STEM-in-SEM image in Fig. 23f, the underlying DL retains the original lath martensitic morphology along with tempered cementite. Under these thermally dominated conditions, NC grain formation proceeds via a CDRX mechanism. This process involves a gradual increase in boundary misorientation through the rotation of subgrains within the re-austenitized phase, followed by rapid quenching that produces NC untempered martensite, as shown in Fig. 23d. The distinct nanohardness responses shown in Fig. 21c,d further support these mechanistic differences, with the measured hardness trends closely correlating with the observed microstructural features and clearly distinguishing between M-WL and T-WL formation mechanisms.

By integrating multi-scale characterization analysis, this work demonstrates that NC grain formation in the M-WL follows a microstructural evolution pathway analogous to that observed in bulk nanostructured materials produced by multi-pass SPD techniques such as like ECAP [21], ARB [20], and HPT [19]. Notably, in the present case, comparable nanostructured states are achieved locally at the hard-turned surface in a single machining pass during final finishing.

6.3 Formation of WLs and behavior of nanoprecipitates in Hybrid 60 steel

Building on the understanding of WL microstructural evolution in AISI 52100 steel, the primary objective of this part of the study was to assess whether WLs can be generated in hard-turned Hybrid 60 steel using fresh inserts, as reported in *Paper V*. As discussed in Section 2.4, Hybrid 60 steel exhibits distinct phase constituents and higher phase transformation temperatures compared to AISI 52100 steel, which can significantly influence WL formation mechanisms in combination with materials intrinsic properties.

Hard turning at low cutting conditions resulted in pronounced grain refinement region of ~100-150 nm thickness from the machined surface into the workpiece material, leading to the formation of NC grains, as observed by BF STEM and TKD analyses (Fig. 26a,b). Beneath this NC layer, lamellar grains are formed via grain subdivision mechanism, similar to that observed in AISI 52100 steel. In addition to intrinsic material property differences between the two steels, the reduced extent of the NC grain area in the Hybrid 60 steel is attributed to differences in tool geometry; in particular, a chamfer angle of 15° was used for Hybrid 60 steel compared to 35° for AISI 52100 steel and a reduced tool nose radius of 1.2 mm for Hybrid 60 steel compared to 2 mm for AISI 52100 steel. The variations in TMIs, particularly in plastic strain, contact pressure, and ploughing depth which depend on the position of the stagnation zone arising from differences in tool geometry, directly influence the extent and volume of material undergoing deformation during hard turning. In summary, the microstructural evolution at low cutting conditions in Hybrid 60 steel begins with grain subdivision and subsequently transitions into NC grain formation via a mechanically assisted triple junction motion DRV mechanism consistent with the M-WL formation mechanism. Under high cutting conditions, the thickness of the NC grain layer increases to ~300-400 nm. In this case, no lamellar grain region is observed beneath the NC layer, but instead, subgrain structures dominate, as shown in Fig. 26c,d. Owing to the lower thermal conductivity of Hybrid 60 steel compared to AISI 52100 steel, the heat generated during hard turning remains highly localized at the surface. This localization limits the development of a pronounced temperature gradient into the subsurface during the short tool-workpiece interaction time, thereby suppressing the formation of a distinct DL, which was not observed in LOM. Given the extremely thin affected region, distinguishing a DL is challenging even using electron microscopy. Consequently, NC grain formation under high cutting conditions is attributed to a CDRX assisted mechanism similar to the T-WL formation, but without the development of a pronounced DL.

The superior mechanical performance of Hybrid 60 steel is primarily obtained from nano-sized NiAl intermetallic precipitates and Cr-rich M_7C_3/$M_{23}C_6$ secondary carbides. However, the intense TMIs experienced during hard turning significantly modified dislocation/precipitate interactions near the surface. As reported in *Paper V*, these interactions result in deformation and partial or complete dissolution of precipitates within the near-surface region, with the severity of these effects reducing with depth and showed a clear gradient in precipitate morphology from surface to bulk. A schematic representation of this precipitate dissolution process is provided in Fig. 27. Initially, the high density of moving dislocations subjects both the NiAl intermetallics and Cr-rich secondary carbides to intense shear stresses, causing precipitate elongation. As deformation increases, the precipitates are sheared off by dislocations, effectively propelling the atoms forward by creating fast diffusion pathways. Under continued severe deformation, the combined effects of elevated dislocation density (and associated vacancy concentration), extreme shear stress, and adiabatic temperature rise promote partial dissolution of precipitate into the surrounding matrix. This process leads to fragmentation of the precipitates and ultimately, accelerated and complete dissolution of NiAl intermetallics and partial dissolution of Cr-rich secondary carbides into the BCC/BCT solid solution closer to the hard-turned surface.

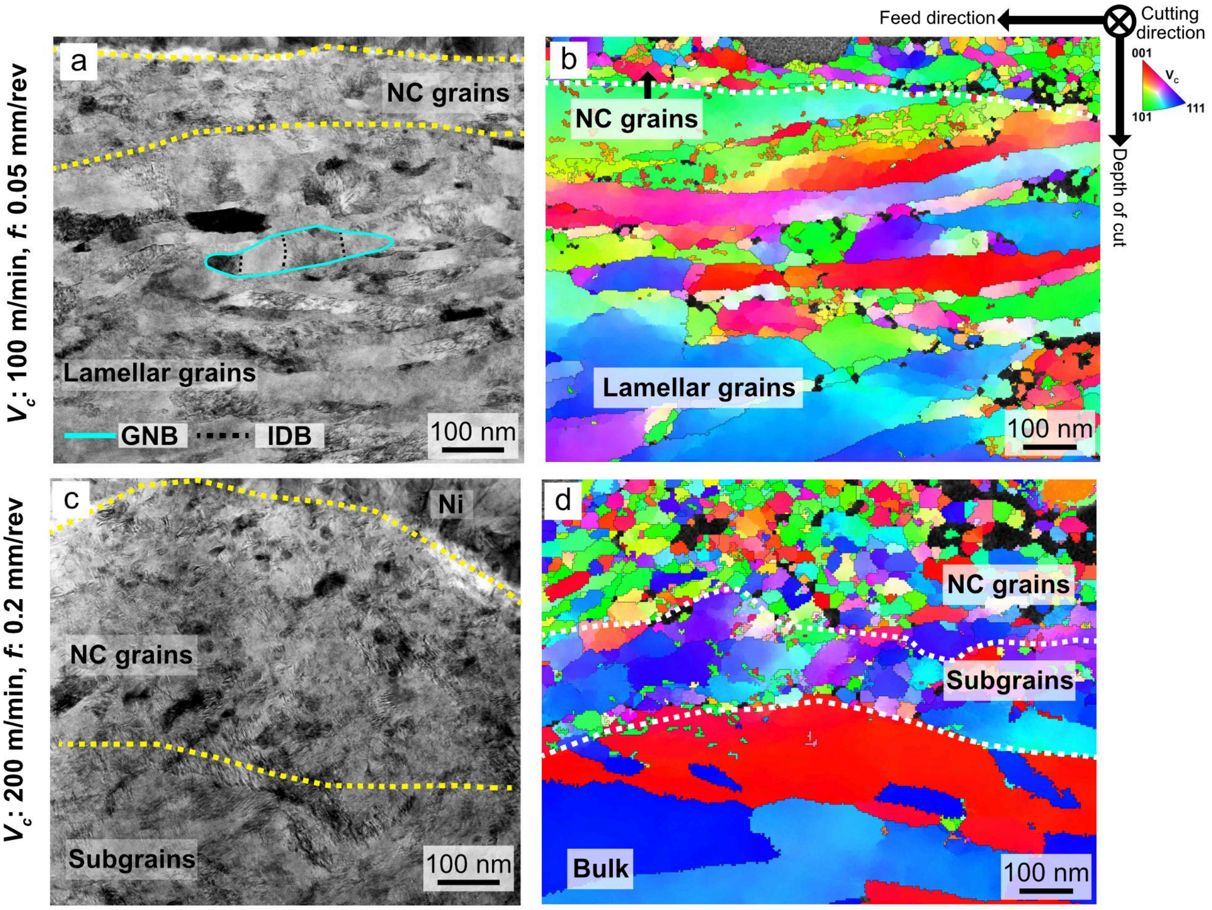

Fig. 26. (a) BF STEM image and (b) TKD IPF orientation map of the V_c*: 100 m/min and f: 0.05 mm/rev (low). (c) BF STEM image and (d) TKD IPF orientation map of the* V_c*: 200 m/min and f: 0.2 mm/rev (high).*

The formation of an NC grain layer at the hard-turned surface resulted in a significant increase in nanohardness by ~24% under low cutting conditions and ~17% under high cutting conditions. Notably, this hardness enhancement was achieved despite APT revealing extensive precipitate deformation and dissolution within the NC layer. This observation indicates a reduced contribution from precipitation strengthening (σ_p) in the hard-turned surface region. Instead, the observed hardness increase is primarily attributed to grain boundary strengthening due to extreme grain refinement, dislocation strengthening induced by high strain-rate plastic deformation, and solid solution strengthening arising from the partial dissolution of precipitates.

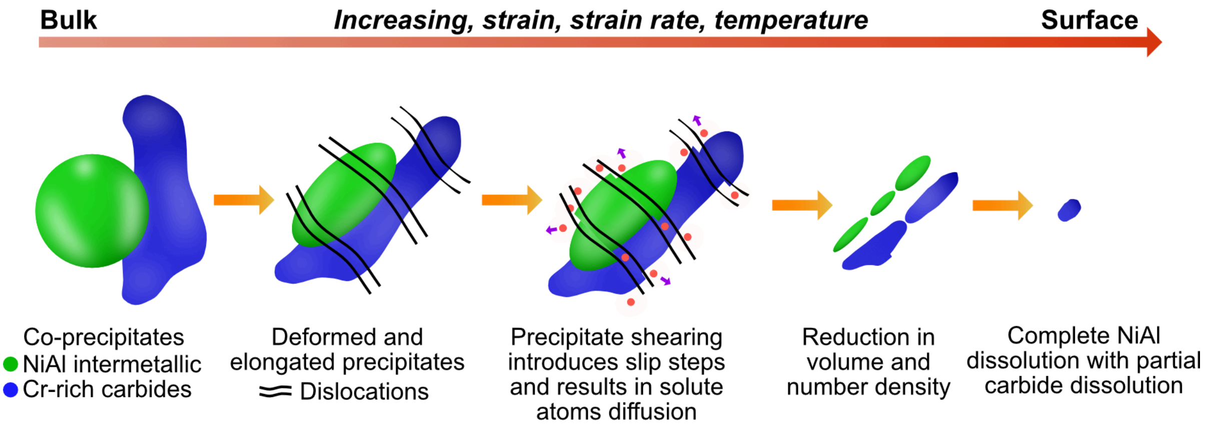

Fig. 27. Schematic illustration of the NiAl intermetallic and Cr-rich secondary carbide nanoprecipitates dissolution process.

This study demonstrates that WLs can indeed be generated on Hybrid 60 steel surfaces using fresh inserts, with a primary focus on M-WL formation. An important result of this work is that the presence or absence of a lamellar grain region serves as the critical feature for identifying the dominant microstructural evolution mechanism, whether through DRV or CDRX. This microstructural fingerprint is particularly important in the case of Hybrid 60 steel, where traditional features such as the underlying DL was notably unseen in both WL types. Consequently, high-resolution imaging of the subsurface grain morphology remains the most reliable method for characterizing the formation pathways in these alloy systems, where the cutting temperatures and other TMIs are difficult to predict.

CHAPTER 7

Conclusions and Future Work

This chapter presents the conclusions corresponding to the research questions formulated in Chapter 1, followed by recommendations for future work.

7.1 Conclusions

RQ1: What influence do process parameters, the geometry of the cutting tool, and the initial retained austenite content have on the formation of WLs in AISI 52100 steel after hard turning?

- Hard turning at low V_c: 60 m/min and low f: 0.05 mm/rev, with constant a_p: 0.2 mm, P: 150 bar, and Y: 35°, resulted in superior surface integrity. These conditions promoted lower R_a and higher surface compressive residual stresses through the formation of M-WL.
- In contrast, hard turning at high V_c: 110 m/min and high f: 0.2 mm/rev, while maintaining the similar a_p, P, and Y conditions led to increased R_a and diminished surface compressive stresses when using fresh inserts. Under identical conditions with worn inserts, tensile residual stresses developed at the surface, accompanied by the formation of a T-WL.
- The generation of M-WL was achieved using fresh inserts from the initial stages of machining. When worn inserts were employed, the M-WL thickness increased substantially, generating significantly higher surface and subsurface compressive stresses. Notably, the R_a obtained with worn inserts was ~3 times lower than that observed for fresh inserts resulting in T-WL.
- The M-WL exhibited an elongated and fragmented morphology with hardness ~26% higher than that of the bulk material, while the underlying material drag zone had a ~7% higher hardness relative to the bulk material. While T-WL exhibited ~27% higher hardness, the beneath DL resulted in ~16% lower hardness relative to the bulk material.
- The initial RA content was identified as a critical factor influencing WL formation. An RA content <2% was found to favor the development of M-WL, both under low

cutting speed conditions with worn inserts and under high cutting speed conditions when using fresh inserts.

RQ2: What is the governing formation mechanism of M-WL in AISI 52100 steel?

- Based on novel insights obtained from SEM, STEM-in-SEM, and TKD pattern-matching analyses, the gradient microstructural evolution observed in the M-WL during hard turning is primarily initiated by a grain subdivision mechanism. This process leads to the formation of lamellar grains, which subsequently undergo mechanically assisted triple junction motion. This DRV mechanism ultimately results in the development of HAGB surrounded rectangular NC grains.
- The evidence from quantitative TKD pattern matching analysis confirms the presence of lamellar grains beneath the M-WL, characterized by the coexistence of high-angle GNBs and low-angle IDBs.
- With increasing TMIs towards the hard-turned surface, these lamellar grains progressively transform into rectangular NC grains, within which both H-type and Y-type triple junction were observed.
- In contrast, the microstructural evolution associated with the T-WL is governed by a distinct mechanism, namely CDRX. In this case, surface temperatures exceed the austenitization threshold, facilitating subgrain rotation and progressive boundary misorientation. Subsequent rapid quenching leads to the formation of untempered martensite with NC grains, while the accompanying thermal gradient gives rise to a DL beneath the T-WL.

RQ3: Does hard turning on Hybrid 60 dual-hardening steel lead to WL formation and how does this affect the nanoprecipitates?

- Hard turning at V_c: 100 m/min and f: 0.05 mm/rev resulted in the formation of a M-WL, whereas the V_c: 200 m/min and f: 0.2 mm/rev led to the formation of a T-WL using fresh inserts, consistent with the observed mechanisms in AISI 52100 steel.
- Notably, the T-WL did not exhibit a clearly defined DL. However, the formation mechanisms were identified from the presence of lamellar grains, which are indicative of intense severe plastic deformation and are typically associated with M-WL formation.
- At the hard-turned surface, both the strength enhancing NiAl intermetallics and Cr-rich secondary carbides experienced partial to complete dissolution under both cutting conditions.
- Despite the differences in formation mechanisms and precipitates dissolution, both M-WL and T-WL exhibited increased hardness. This hardening is primarily attributed to grain boundary strengthening and dislocation strengthening, with an additional contribution from solid solution strengthening resulting from precipitate dissolution.

7.2 Future work

Based on the findings reported in this thesis, several topics requires further investigation. These potential research directions are outlined below.

The M-WL generated using fresh cutting inserts was consistently observed to have a thickness ranging from a few hundred nanometers to ~1.5 μm. Increasing the thickness of this layer could be advantageous. One promising approach is to modify tool geometry to enhance the ploughing depth during hard turning, thereby increasing the volume of plastically deformed material beneath the tool flank. Such an approach should be carefully designed to minimize thermal effects, as excessive temperature rise would increase the likelihood of forming a T-WL. Although the M-WL demonstrated superior surface integrity, further work is required to investigate its wear mechanisms and fatigue life performance. Comparative studies involving M-WL, T-WL, and conventionally ground specimens would provide valuable insight into their respective degradation and failure behaviors.

Hybrid 60 steel is specifically designed for high temperature service in the range of 500-600 °C, where nanoprecipitates are typically stable for better mechanical performances. However, in the present study, these nanoprecipitates were observed to deform or dissolve following hard turning. In this context, it would be of interest to examine the thermal stability of the NC grains formed within the M-WL in this particular temperature range. Such studies could include nanoindentation and TKD measurements to assess the evolution of mechanical properties and microstructure. In addition, in-situ TEM heating experiments focused on the M-WL region would enable direct observation of nanoscale mechanisms such as grain growth or possible grain boundary pinning.

Finally, in the present work, hard turning of Hybrid 60 steel was carried out after heat treatment process, resulting in nanoprecipitate dissolution. An alternative processing route would be to perform hard turning prior to the tempering process in order to generate M-WL, followed by subsequent tempering at 520 °C. This approach would allow investigation of the precipitation behaviour of NiAl intermetallics and Cr-rich secondary carbides within or surrounding the NC grains of the M-WL. Such studies, combined with appropriate mechanical testing, would contribute to a more comprehensive understanding of fatigue life and failure mechanisms in hard-turned Hybrid 60 steel.

Acknowledgements

I would like to express my wholehearted and deepest gratitude to Prof. Uta Klement and Dr. Seyed B. Hosseini (AB SKF) for giving me this wonderful opportunity. They have been absolutely incredible as supervisors who believed in me, supported me at every stage, encouraged me, and gave me the freedom to develop my own scientific path. I would also thank my examiner, Prof. Peter Krajnik, for his helpful feedback and support.

I would like to thank all members of the Turn2Flex project for their support and valuable input during this work. In particular, I am grateful to Dr. Jonas Holmberg (RISE IVF AB) for his guidance and discussions on surface integrity. I also thank Wolfgang Neuhs, Hirotsugu Iwasaki (Sumitomo Electric Hardmetal Corp.), and Stefan Kimming (AB SKF) for their help with the hard turning experiments. I am thankful to Dr. Thomas Bjork (Ovako AB) for providing the Hybrid 60 samples.

I would like to acknowledge the support of the research engineer Dr. Antonio Mulone for his training and in-depth discussions on the use of STEM-in-SEM, TKD, and FIB techniques. My thanks also extend to Dr. Thorsten Meiners (Oxford Instruments NanoAnalysis) for his training in the TKD pattern matching technique. I am grateful to Micro Materials Ltd. (UK) for their support with nanoindentation measurements, as well as to Dr. Mohammad Hoseini Athar for his valuable training in nanoindentation at the Hultgren Laboratory (KTH). I also acknowledge the Axel Hultgren Foundation and the ÅForsk Foundation for the scholarships that helped me attend international conferences.

I sincerely thank Prof. Mattias Thuvander and Dr. Severin Jakob from the Department of Physics at Chalmers for their support with APT measurements. I am also grateful to Dr. David Mayweg for his valuable insights into the characterization of nanocrystalline grains, Dr. Olof Bäcke for his guidance on FIB sample thinning, and Dr. Stefan Gustafsson from the Chalmers Materials Analysis Laboratory (CMAL) for his support during FIB work and assistance with TEM analysis.

I would like to thank my friends and colleagues at the Division of MM and EM for their support and for making my time at Chalmers both productive and enjoyable. I am especially grateful to Anok, Bala, Vishnu, Daniel, Erika, Plinio, Fardan, Charlie, Angelica, Rasmus, Satya, and many others for the memorable moments and shared experiences.

To my close friends Reddy, Rahul, Sukesh, Kalyan, Vardan, Vishnu, Diwakar, Srikanth, Nithin, and others from the Netherlands and my hometown Ramagundam, thank you for always being there for me.

Finally, I wish to express my deepest gratitude to my family, who have always stood by me. I am deeply grateful to my parents and brother for everything they have done. Meghana and Bhavana – thanks for always being there. Above all, I would like to thank my fiancée, Sophia, for her love, patience, and encouragement throughout this journey.

Sahith Kokkirala
February, 2026

References

[1] I.S. Jawahir, E. Brinksmeier, R. M'Saoubi, D.K. Aspinwall, J.C. Outeiro, D. Meyer, D. Umbrello, A.D. Jayal, Surface integrity in material removal processes: Recent advances, CIRP Ann. Manuf. Technol. 60 (2011) 603–626. https://doi.org/10.1016/j.cirp.2011.05.002.

[2] H.K. Tönshoff, C. Ardent, R. Ben Amor, Cutting of Hardened Steel, CIRP Ann. Manuf. Technol. 49 (2000) 1–19.

[3] S. Chinchanikar, S.K. Choudhury, Machining of hardened steel - Experimental investigations, performance modeling and cooling techniques: A review, Int. J. Mach. Tools Manuf. 89 (2015) 95–109. http://dx.doi.org/10.1016/j.ijmachtools.2014.11.002.

[4] D. Umbrello, J. Hua, R. Shivpuri, Hardness-based flow stress and fracture models for numerical simulation of hard machining AISI 52100 bearing steel, Materials Science and Engineering: A 374 (2004) 90–100. https://doi.org/10.1016/j.msea.2004.01.012.

[5] S.P.F.C. Jaspers, J.H. Dautzenberg, Material behaviour in metal cutting: Strains, strain rates and temperatures in chip formation, J. Mater. Process. Technol. 121 (2002) 123–135. https://doi.org/10.1016/S0924-0136(01)01227-4.

[6] A. Ramesh, S.N. Melkote, L.F. Allard, L. Riester, T.R. Watkins, Analysis of white layers formed in hard turning of AISI 52100 steel, Materials Science and Engineering: A 390 (2005) 88–97.

[7] J. Barry, G. Byrne, TEM study on the surface white layer in two turned hardened steels, Materials Science and Engineering: A 325 (2002) 356–364.

[8] S. Akcan, W.I.S. Shah, S.P. Moylan, P.N. Chhabra, S. Chandrasekar, H.T.Y. Yang, Formation of white layers in steels by machining and their characteristics, Metall. Mater. Trans. A Phys. Metall. Mater. Sci. 33 (2002) 1245–1254.

[9] Y.K. Chou, C.J. Evans, White Layers and Thermal Modeling of Hard Turned Surfaces, ASME International Mechanical Engineering Congress and Exposition, Proceedings (IMECE) 1997-W (1997) 75–82. https://doi.org/10.1115/IMECE1997-1138.

[10] S.B. Hosseini, U. Klement, A descriptive phenomenological model for white layer formation in hard turning of AISI 52100 bearing steel, CIRP J. Manuf. Sci. Technol. 32 (2021) 299–310. https://doi.org/10.1016/j.cirpj.2021.01.014.

[11] Z. Chen, M.H. Colliander, G. Sundell, R.L. Peng, J. Zhou, S. Johansson, J. Moverare, Nano-scale characterization of white layer in broached Inconel 718, Materials Science and Engineering: A 684 (2017) 373–384. https://doi.org/10.1016/j.msea.2016.12.045.

[12] M. Brown, P. Crawforth, R. M'Saoubi, T. Larsson, B. Wynne, A. Mantle, H. Ghadbeigi, Quantitative characterization of machining-induced white layers in Ti–6Al–4V, Materials Science and Engineering: A 764 (2019) 138220. https://doi.org/10.1016/j.msea.2019.138220.

[13] H. Liu, J. Zhang, B. Xu, X. Xu, W. Zhao, Prediction of microstructure gradient distribution in machined surface induced by high speed machining through a coupled FE and CA approach, Mater. Des. 196 (2020) 109133. https://doi.org/10.1016/j.matdes.2020.109133.

[14] S.B. Hosseini, U. Klement, Y. Yao, K. Ryttberg, Formation mechanisms of white layers induced by hard turning of AISI 52100 steel, Acta Mater. 89 (2015) 258–267. http://dx.doi.org/10.1016/j.actamat.2015.01.075.

[15] D.W. Schwach, Y.B. Guo, A fundamental study on the impact of surface integrity by hard turning on rolling contact fatigue, Int. J. Fatigue 28 (2006) 1838–1844. https://doi.org/10.1016/j.ijfatigue.2005.12.002.

[16] Y.B. Guo, A.W. Warren, F. Hashimoto, The basic relationships between residual stress, white layer, and fatigue life of hard turned and ground surfaces in rolling contact, CIRP J. Manuf. Sci. Technol. 2 (2010) 129–134. https://doi.org/10.1016/j.cirpj.2009.12.002.

[17] K. Edalati, A. Bachmaier, V.A. Beloshenko, Y. Beygelzimer, V.D. Blank, W.J. Botta, K. Bryła, J. Čížek, S. Divinski, N.A. Enikeev, Y. Estrin, G. Faraji, R.B. Figueiredo, M. Fuji, T. Furuta, T. Grosdidier, J. Gubicza, A. Hohenwarter, Z. Horita, J. Huot, Y. Ikoma, M. Janeček, M. Kawasaki, P. Král, S. Kuramoto, T.G. Langdon, D.R. Leiva, V.I. Levitas, A. Mazilkin, M. Mito, H. Miyamoto, T. Nishizaki, R. Pippan, V. V. Popov, E.N. Popova, G. Purcek, O. Renk, Á. Révész, X. Sauvage, V. Sklenicka, W. Skrotzki, B.B. Straumal, S. Suwas, L.S. Toth, N. Tsuji, R.Z. Valiev, G. Wilde, M.J. Zehetbauer, X. Zhu, Nanomaterials by severe plastic deformation: review of historical developments and recent advances, Mater. Res. Lett. 10 (2022) 163–256. https://doi.org/10.1080/21663831.2022.2029779.

[18] P.W. Bridgman, Flow phenomena in heavily stressed metals, J. Appl. Phys. 8 (1937) 328–336. https://doi.org/10.1063/1.1710301.

[19] P.W. Bridgman, Studies in large plastic flow and fracture: with special emphasis on the effects of hydrostatic pressure, McGraw-Hill, 1952.

[20] Y. Saito, H. Utsunomiya, N. Tsuji, T. Sakai, Novel ultra-high straining process for bulk materials—development of the accumulative roll-bonding (ARB) process, Acta Mater. 47 (1999) 579–583.

[21] V.M. Segal, Materials processing by simple shear, Materials Science and Engineering A 197 (1995) 157–164. https://doi.org/10.1016/0921-5093(95)09705-8.

[22] L. Ke, L. Jian, Surface nanocrystallization (SNC) of metallic materials-presentation of the concept behind a new approach, J. Mater. Sci. Technol. 15 (1999) 193–197.

[23] N.R. Tao, Z.B. Wang, W.P. Tong, M.L. Sui, J. Lu, K. Lu, An investigation of surface nanocrystallization mechanism in Fe induced by surface mechanical attrition treatment, Acta Mater. 50 (2002) 4603–4616. https://doi.org/10.1016/S1359-6454(02)00310-5.

[24] G. Krauss, Microstructures, Processing, and Properties of Steels, Properties and Selection: Irons, Steels, and High-Performance Alloys 1 (2018) 126–139. https://doi.org/10.31399/asm.hb.v01.a0001008.

[25] P.D. Portella, R. Helmerich, Adolf Martens and his contribution to materials engineering, Eng. Fail. Anal. 43 (2014) 2–10. https://doi.org/10.1016/j.engfailanal.2014.03.001.

[26] H.K.D.H. Bhadeshia, C.M. Wayman, Phase Transformations: Nondiffusive, Fifth Edit, Elsevier, 2014. https://doi.org/10.1016/B978-0-444-53770-6.00009-5.

[27] H. Bhadeshia, R. Honeycombe, Formation of Martensite, 4th ed., Elsevier Ltd, 2017. https://doi.org/10.1016/b978-0-08-100270-4.00005-6.

[28] G. Krauss, Martensite in steel: Strength and structure, Materials Science and Engineering: A 273–275 (1999) 40–57. https://doi.org/10.1016/s0921-5093(99)00288-9.

[29] A. Gramlich, W. Hagedorn, K. Greiff, U. Krupp, Air Cooling Martensites—The Future of Carbon Neutral Steel Forgings?, Adv. Eng. Mater. 25 (2023) 1–6. https://doi.org/10.1002/adem.202201931.

[30] A. Gramlich, T. Schmiedl, S. Schönborn, T. Melz, W. Bleck, Development of air-hardening martensitic forging steels, Materials Science and Engineering: A 784 (2020) 139321. https://doi.org/10.1016/j.msea.2020.139321.

[31] S. Morito, H. Yoshida, T. Maki, X. Huang, Effect of block size on the strength of lath martensite in low carbon steels, Materials Science and Engineering: A 438–440 (2006) 237–240. https://doi.org/10.1016/j.msea.2005.12.048.

[32] C. Celada-Casero, J. Sietsma, M.J. Santofimia, The role of the austenite grain size in the martensitic transformation in low carbon steels, Mater. Des. 167 (2019). https://doi.org/10.1016/j.matdes.2019.107625.

[33] A. Shibata, S. Morito, T. Furuhara, T. Maki, Local orientation change inside lenticular martensite plate in Fe-33Ni alloy, Scr. Mater. 53 (2005) 597–602. https://doi.org/10.1016/j.scriptamat.2005.04.023.

[34] H. Bhadeshia, R. Honeycombe, Tempering of Martensite, 4th ed., Elsevier Ltd, 2017. https://doi.org/10.1016/b978-0-08-100270-4.00009-3.

[35] M. Perez, C. Sidoroff, A. Vincent, C. Esnouf, Microstructural evolution of martensitic 100Cr6 bearing steel during tempering: From thermoelectric power measurements to the prediction of dimensional changes, Acta Mater. 57 (2009) 3170–3181. https://doi.org/10.1016/j.actamat.2009.03.024.

[36] W.M. Garrison, M.S. Bhat, An approach to developing an alternative hot work die steel, Metallurgical Transactions A 19 (1988) 1751–1760. https://doi.org/10.1007/BF02645143.

[37] M. Hofinger, M. Staudacher, M. Ognianov, C. Turk, H. Leitner, R. Schnitzer, Microstructural evolution of a dual hardening steel during heat treatment, Micron 120 (2019) 48–56. https://doi.org/10.1016/j.micron.2019.02.004.

[38] W.M. Garrison, M.K. Banerjee, Martensitic Non-Stainless Steels: High Strength and High Alloy, Elsevier Ltd., 2018. https://doi.org/10.1016/b978-0-12-803581-8.02519-4.

[39] S. Kokkirala, K. Osman, J. Holmberg, S. Kimming, H. Iwasaki, U. Klement, S.B. Hosseini, The role of retained austenite on the formation of the nanostructured hard-turned induced white layer in AISI 52100 bearing steel, Procedia CIRP 123 (2024) 292–297. https://doi.org/10.1016/j.procir.2024.05.052.

[40] L.D. Barlow, M. Du Toit, Effect of austenitizing heat treatment on the microstructure and hardness of martensitic stainless steel AISI 420, J. Mater. Eng. Perform. 21 (2012) 1327–1336. https://doi.org/10.1007/s11665-011-0043-9.

[41] A. Jan-Erik, F. Lindberg, Ö. Patrik, Hybrid Steel Enhances Component Performance at Reduced Weight, Lightweight Design Worldwide 12 (2019) 34–39. https://doi.org/10.1007/s41777-018-0063-3.

[42] J.E. Andersson, F. Lindberg, S. Ooi, Hybrid steel and its potential for bearing applications, ASTM Special Technical Publication STP 1623 (2020) 436–454. https://doi.org/10.1520/STP162320190163.

[43] M. Hörnqvist Colliander, S. Ooi, K. Lindgren, T. Müller, M. Thuvander, In Situ Measurements of NiAl Precipitation During Aging of Dual Hardening Hybrid Steels, Metall. Mater. Trans. A

Phys. Metall. Mater. Sci. 55 (2024) 4146–4158. https://doi.org/10.1007/s11661-024-07536-z.

[44] Z. Zheng, M. Lei, C. Huang, M. Wan, Carbide precipitation during tempering of hybrid steel 60, Mater. Res. Express 11 (2024). https://doi.org/10.1088/2053-1591/ad2576.

[45] S. Jakob, M. Hörnqvist Colliander, J. Kawser, S. Rashidi, S.W. Ooi, M. Thuvander, Concomitant Precipitation of Intermetallic $β$-NiAl and Carbides in a Precipitation Hardened Steel, Metall. Mater. Trans. A Phys. Metall. Mater. Sci. 55 (2024) 870–879. https://doi.org/10.1007/s11661-023-07291-7.

[46] W. Grzesik, Mechanics of cutting and chip formation, Machining of Hard Materials (2011) 87–114. https://doi.org/10.1007/978-1-84996-450-0_3.

[47] V.P. Astakhov, Machining of hard materials - Definitions and industrial applications, Machining of Hard Materials (2011) 1–32. https://doi.org/10.1007/978-1-84996-450-0_1.

[48] W. Koenig, R. Komanduri, H.K. Toenshoff, G. Ackershott, Machining of Hard Materials., CIRP Annals 33 (1984) 417–427. https://doi.org/10.1016/s0007-8506(16)30164-0.

[49] F. Klocke, A. Kuchle, Manufacturing Process 1, 2011.

[50] W. Grzesik, Chapter Four - Cutting Tool Materials, in: W. Grzesik (Ed.), Advanced Machining Processes of Metallic Materials, Elsevier, Amsterdam, 2008: pp. 27–I. https://doi.org/https://doi.org/10.1016/B978-008044534-2.50006-0.

[51] L.N. López De Lacalle, A. Lamikiz, J. Fernández De Larrinoa, I. Azkona, Advanced cutting tools, Machining of Hard Materials (2011) 33–86. https://doi.org/10.1007/978-1-84996-450-0_2.

[52] W. Grzesik, 15.3 - Hard Part Machining, in: W. Grzesik (Ed.), Advanced Machining Processes of Metallic Materials, Elsevier, Amsterdam, 2008: pp. 245–259. https://doi.org/https://doi.org/10.1016/B978-008044534-2.50032-1.

[53] W. Grzesik, Chapter Twelve - Tool Wear and Damage, in: W. Grzesik (Ed.), Advanced Machining Processes of Metallic Materials, Elsevier, Amsterdam, 2008: pp. 163–VII. https://doi.org/https://doi.org/10.1016/B978-008044534-2.50028-X.

[54] S. Kokkirala, The Formation of White Layers and its Impact on Surface Integrity of Hard-Turned Tempered Martensitic Bearing Steels, Chalmers University of Technology, 2024. https://research.chalmers.se/publication/541260.

[55] J.-E. Ståhl, S.T. AB, Metal Cutting: Theories and Models, Division of Production and Materials Engineering, 2012.

[56] M. Field, J.F. Kahles, Review of surface integrity of machined components, CIRP Annals 20 (1971) 153–163.

[57] W. Grzesik, Chapter Twenty - Surface Integrity, in: W. Grzesik (Ed.), Advanced Machining Processes of Metallic Materials, Elsevier, Amsterdam, 2008: pp. 405–XVI. https://doi.org/https://doi.org/10.1016/B978-008044534-2.50039-4.

[58] A.M. Abrão, J.L.S. Ribeiro, J.P. Davim, Surface Integrity, in: Machining of Hard Materials, 2011: pp. 115–141. https://doi.org/10.1007/978-1-84996-450-0_4.

[59] P.J. Withers, H.K.D.H. Bhadeshia, Residual stress part 2 - Nature and origins, Materials Science and Technology 17 (2001) 366–375. https://doi.org/10.1179/026708301101510087.

[60] V.G. Navas, O. Gonzalo, I. Bengoetxea, Effect of cutting parameters in the surface residual stresses generated by turning in AISI 4340 steel, Int. J. Mach. Tools Manuf. 61 (2012) 48–57. https://doi.org/10.1016/j.ijmachtools.2012.05.008.

[61] P. Dahlman, F. Gunnber, M. Jacobson, The influence of rake angle, cutting feed and cutting depth on residual stresses in hard turning, J. Mater. Process. Technol. 147 (2004) 181–184. https://doi.org/10.1016/j.matprotec.2003.12.014.

[62] F. Gunnberg, M. Escursell, M. Jacobson, The influence of cutting parameters on residual stresses and surface topography during hard turning of 18MnCr5 case carburised steel, J. Mater. Process. Technol. 174 (2006) 82–90. https://doi.org/10.1016/j.jmatprotec.2005.02.262.

[63] S. Kokkirala, J. Holmberg, U. Klement, R. Lundstrom, H. Iwasaki, S.B. Hosseini, Effect of cutting parameters on the generated surface integrity of hard-turned martensitic AISI 52100 bearing steel, Procedia CIRP 115 (2022) 154–159. https://doi.org/10.1016/j.procir.2022.10.066.

[64] J. Hua, R. Shivpuri, X. Cheng, V. Bedekar, Y. Matsumoto, F. Hashimoto, T.R. Watkins, Effect of feed rate, workpiece hardness and cutting edge on subsurface residual stress in the hard turning of bearing steel using chamfer + hone cutting edge geometry, Materials Science and Engineering: A 394 (2005) 238–248. https://doi.org/10.1016/j.msea.2004.11.011.

[65] Y. Matsumoto, F. Hashimoto, G. Lahoti, Surface integrity generated by precision hard turning, CIRP Ann. Manuf. Technol. 48 (1999) 59–62. https://doi.org/10.1016/S0007-8506(07)63131-X.

[66] A.M. Abrão, D.K. Aspinwall, The surface integrity of turned and ground hardened bearing steel, Wear 196 (1996) 279–284. https://doi.org/10.1016/0043-1648(96)06927-X.

[67] M. Liu, J.I. Takagi, A. Tsukuda, Effect of tool nose radius and tool wear on residual stress distribution in hard turning of bearing steel, J. Mater. Process. Technol. 150 (2004) 234–241. https://doi.org/10.1016/j.jmatprotec.2004.02.038.

[68] W. König, A. Berktold, K.F. Koch, Turning versus Grinding - A Comparison of Surface Integrity Aspects and Attainable Accuracies, CIRP Ann. Manuf. Technol. 42 (1993) 39–43. https://doi.org/10.1016/S0007-8506(07)62387-7.

[69] P.I. Varela, C.S. Rakurty, A.K. Balaji, Surface integrity in hard machining of 300M Steel: Effect of cutting-edge geometry on machining induced residual stresses, Procedia CIRP 13 (2014) 288–293. https://doi.org/10.1016/j.procir.2014.04.049.

[70] G.C. Benga, A.M. Abrao, Turning of hardened 100Cr6 bearing steel with ceramic and PCBN cutting tools, 144 (2003) 237–241. https://doi.org/10.1016/S0924-0136(03)00346-7.

[71] J.D. Thiele, S. N. Melkote, Effect of cutting edge geometry and workpiece hardness on surface generation in the finish hard turning of AISI 52100 steel, J. Mater. Process. Technol. 94 (1999) 216–226. https://doi.org/10.1016/S0924-0136(99)00111-9.

[72] H.A. Kishawy, M.A. Elbestawi, Effects of process parameters on material side flow during hard turning, Int. J. Mach. Tools Manuf. 39 (1999) 1017–1030. https://doi.org/10.1016/S0890-6955(98)00084-4.

[73] J. Stead, Micro-metallography and its practical applications, Journal of Western Scottish Iron and Steel Institute 19 (1912) 169–204.

[74] M.C. Shaw, A. Vyas, Heat-Affected Zones in Grinding Steel, CIRP Ann. Manuf. Technol. 43 (1994) 279–282. https://doi.org/10.1016/S0007-8506(07)62213-6.

[75] A.M. Wusatowska-Sarnek, B. Dubiel, A. Czyrska-Filemonowicz, P.R. Bhowal, N. Ben Salah, J.E. Klemberg-Sapieha, Microstructural characterization of the white etching layer in nickel-based superalloy, Metall. Mater. Trans. A Phys. Metall. Mater. Sci. 42 (2011) 3813–3825. https://doi.org/10.1007/s11661-011-0779-8.

[76] J.G. Li, M. Umemoto, Y. Todaka, K. Tsuchiya, Nanocrystalline structure formation in carbon steel introduced by high speed drilling, Materials Science and Engineering: A 435–436 (2006) 383–388. https://doi.org/10.1016/j.msea.2006.07.036.

[77] D.M. Turley, The nature of the white-etching surface layers produced during reaming ultra-high strength steel, Materials Science and Engineering 19 (1975) 79–86. https://doi.org/10.1016/0025-5416(75)90010-5.

[78] S.B. Hosseini, U. Klement, J. Kaminski, Microstructure characterization of white layer formed by hard turning and wire electric discharge machining in high carbon steel (AISI 52100), Adv. Mat. Res. 409 (2012) 684–689. https://doi.org/10.4028/www.scientific.net/AMR.409.684.

[79] J. Ahlström, B. Karlsson, Microstructural evaluation and interpretation of the mechanically and thermally affected zone under railway wheel flats, Wear 232 (1999) 1–14. https://doi.org/10.1016/S0043-1648(99)00166-0.

[80] S.X. Li, P.C. Zhao, Y.N. He, S.R. Yu, Microstructural evolution associated with shear location of AISI 52100 under high strain rate loading, Materials Science and Engineering: A 662 (2016) 46–53. https://doi.org/10.1016/j.msea.2016.03.050.

[81] T. Loaiza, R.P. Babu, S. Ooi, P. Hedström, Refining the mechanistic understanding of microstructural decay during rolling contact fatigue in 52100 bearing steel tempered at high temperature, J. Mater. Sci. 58 (2023) 17093–17112. https://doi.org/10.1007/s10853-023-09088-w.

[82] D. Mayweg, L. Morsdorf, X. Wu, M. Herbig, The role of carbon in the white etching crack phenomenon in bearing steels, Acta Mater. 203 (2021). https://doi.org/10.1016/j.actamat.2020.11.022.

[83] Y.B. Guo, J. Sahni, A comparative study of hard turned and cylindrically ground white layers, Int. J. Mach. Tools Manuf. 44 (2004) 135–145. https://doi.org/10.1016/j.ijmachtools.2003.10.009.

[84] B.J. Griffiths, White layer formations at machined surfaces and their relationship to white layer formatins at worn surfaces., 107 (1984) 165–171.

[85] J.A. Bailey, S. Jeelani, S.E. Becker, Surface Integrity in Machining AISI 4340 Steel, J. Eng. Ind. (Trans. ASME) 98 (1976) 999–1007.

[86] F. Zemzemi, H. Khochtali, W. Ben Salem, B. Alzahrani, M.L. Bouazizi, Analytical multi-physics model of microstructure changes in hard turning of AISI 52100 steel: prediction of thicknesses of white and dark layers, International Journal of Advanced Manufacturing Technology 112 (2021) 2755–2771. https://doi.org/10.1007/s00170-020-06521-1.

[87] C. Cappellini, A. Attanasio, G. Rotella, D. Umbrello, Formation of white and dark layers in hard cutting: Influence of tool wear, International Journal of Material Forming 3 (2010) 455–458. https://doi.org/10.1007/s12289-010-0805-1.

[88] W. Zhang, K. Zhuang, Effect of cutting edge microgeometry on surface roughness and white layer in turning AISI 52100 steel, Procedia CIRP 87 (2020) 53–58. https://doi.org/10.1016/j.procir.2020.02.079.

[89] S. Han, S.N. Melkote, M.S. Haluska, T.R. Watkins, White layer formation due to phase transformation in orthogonal machining of AISI 1045 annealed steel, Materials Science and Engineering: A 488 (2008) 195–204. https://doi.org/10.1016/j.msea.2007.11.081.

[90] V. Bedekar, R. Shivpuri, R. Chaudhari, R.S. Hyde, Nanostructural evolution of hard turning layers in response to insert geometry, cutting parameters and material microstructure, CIRP Ann. Manuf. Technol. 62 (2013) 63–66.

[91] R. Hossain, F. Pahlevani, E. Witteveen, A. Banerjee, B. Joe, B.G. Prusty, R. Dippenaar, V. Sahajwalla, Hybrid structure of white layer in high carbon steel - Formation mechanism and its properties, Sci. Rep. 7 (2017) 1–12. https://doi.org/10.1038/s41598-017-13749-7.

[92] F. yuan Zhang, C. zheng Duan, M. jie Wang, W. Sun, White and dark layer formation mechanism in hard cutting of AISI52100 steel, J. Manuf. Process. 32 (2018) 878–887. https://doi.org/10.1016/j.jmapro.2018.04.011.

[93] F. Zhang, C. Duan, W. Sun, K. Ju, Effects of cutting conditions on the microstructure and residual stress of white and dark layers in cutting hardened steel, J. Mater. Process. Technol. 266 (2019) 599–611. https://doi.org/10.1016/j.jmatprotec.2018.11.038.

[94] T. Inoue, Tatara and the Japanese sword: The science and technology, Acta Mech. 214 (2010) 17–30. https://doi.org/10.1007/s00707-010-0308-7.

[95] G. Poulachon, A. Moisan, I.S. Jawahir, On modelling the influence of thermo-mechanical behavior in chip formation during hard turning of 100Cr6 bearing steel, CIRP Ann. Manuf. Technol. 50 (2001) 31–36. https://doi.org/10.1016/S0007-8506(07)62064-2.

[96] C. Zener, J.H. Hollomon, Effect of strain rate upon plastic flow of steel, J. Appl. Phys. 15 (1944) 22–32. https://doi.org/10.1063/1.1707363.

[97] S.B. Hosseini, R. Dahlgren, K. Ryttberg, U. Klement, Dissolution of iron-chromium carbides during white layer formation induced by hard turning of AISI 52100 steel, Procedia CIRP 14 (2014) 107–112. https://doi.org/10.1016/j.procir.2014.03.095.

[98] U. Takashi, H. Mahfudz Al, Y. Keiji, N. Kazuo, Temperature Measurement of CBN Tool in Turning of High Hardness Steel, Annals of the CIRP 48 (1999) 63–66.

[99] S.B. Hosseini, T. Beno, U. Klement, J. Kaminski, K. Ryttberg, Cutting temperatures during hard turning—Measurements and effects on white layer formation in AISI 52100, J. Mater. Process. Technol. 214 (2014) 1293–1300. https://linkinghub.elsevier.com/retrieve/pii/S0924013614000399.

[100] J. Orlich, H.-J. Pietrzeniuk, Atlas zur Wärmebehandlung der Stähle: Zeit-Temperatur-Austenitisierung-Schaubilder, 2. Teil, Verlag Stahleisen, 1976.

[101] D.A. Porter, K.E. Easterling, M.Y. Sherif, Phase transformations in metals and alloys, third edition, Taylor & Francis, 2009.

[102] A. Ramesh, S.N. Melkote, Modeling of white layer formation under thermally dominant conditions in orthogonal machining of hardened AISI 52100 steel, Int. J. Mach. Tools Manuf. 48 (2008) 402–414. https://doi.org/10.1016/j.ijmachtools.2007.09.007.

[103] M.J. Bibby, J.G. Parr, The martensitic transformation in pure iron, (1963).

[104] C.Z. Duan, L.C. Zhang, Adiabatic shear banding in AISI 1045 steel during high speed machining: Mechanisms of microstructural evolution, Materials Science and Engineering: A 532 (2012) 111–119. https://doi.org/10.1016/j.msea.2011.10.071.

[105] B. Zhang, W. Shen, Y. Liu, X. Tang, Y. Wang, Microstructures of surface white layer and internal white adiabatic shear band, Wear 211 (1997) 164–168. https://doi.org/10.1016/S0043-1648(97)00099-9.

[106] M. Sun, L. Hao, S. Li, D. Li, Y. Li, Modeling flow stress constitutive behavior of SA508-3 steel for nuclear reactor pressure vessels, Journal of Nuclear Materials 418 (2011) 269–280. https://doi.org/10.1016/j.jnucmat.2011.07.011.

[107] H.J. McQueen, C.A.C. Imbert, Dynamic recrystallization: Plasticity enhancing structural development, J. Alloys Compd. 378 (2004) 35–43. https://doi.org/10.1016/j.jallcom.2003.10.067.

[108] H.Q. Sun, Y.N. Shi, M.X. Zhang, K. Lu, Plastic strain-induced grain refinement in the nanometer scale in a Mg alloy, Acta Mater. 55 (2007) 975–982. https://doi.org/10.1016/j.actamat.2006.09.018.

[109] K. Zhang, Z.B. Wang, Strain-induced formation of a gradient nanostructured surface layer on an ultrahigh strength bearing steel, J. Mater. Sci. Technol. 34 (2018) 1676–1684. https://doi.org/10.1016/j.jmst.2017.12.012.

[110] N. Hansen, R.F. Mehl, New discoveries in deformed metals, Metall. Mater. Trans. A Phys. Metall. Mater. Sci. 32 (2001) 2917–2935. https://doi.org/10.1007/s11661-001-0167-x.

[111] N. Tsuji, R. Gholizadeh, R. Ueji, N. Kamikawa, L. Zhao, Y. Tian, Y. Bai, A. Shibata, Formation Mechanism of Ultrafine Grained Microstructures: Various Possibilities for Fabricating Bulk Nanostructured Metals and Alloys, Mater. Trans. 60 (2019) 1518–1532.

[112] D.A. Hughes, N. Hansen, D.J. Bammann, Geometrically necessary boundaries, incidental dislocation boundaries and geometrically necessary dislocations, Scr. Mater. 48 (2003) 147–153. https://doi.org/10.1016/S1359-6462(02)00358-5.

[113] D.A. Hughes, N. Hansen, High angle boundaries formed by grain subdivision mechanisms, Acta Mater. 45 (1997) 3871–3886. https://doi.org/10.1016/S1359-6454(97)00027-X.

[114] T. Yu, N. Hansen, X. Huang, A. Godfrey, Observation of a new mechanism balancing hardening and softening in metals, Mater. Res. Lett. 2 (2014) 160–165. https://doi.org/10.1080/21663831.2014.886308.

[115] T. Yu, N. Hansen, X. Huang, Recovery by triple junction motion in aluminium deformed to ultrahigh strains, Proceedings of the Royal Society A: Mathematical, Physical and Engineering Sciences 467 (2011) 3039–3065. https://doi.org/10.1098/rspa.2011.0097.

[116] O. Renk, P. Ghosh, R. Pippan, Generation of extreme grain aspect ratios in severely deformed tantalum at elevated temperatures, Scr. Mater. 137 (2017) 60–63. https://doi.org/10.1016/j.scriptamat.2017.04.024.

[117] O. Renk, A. Hohenwarter, S. Wurster, R. Pippan, Direct evidence for grain boundary motion as the dominant restoration mechanism in the steady-state regime of extremely cold-rolled copper, Acta Mater. 77 (2014) 401–410. https://doi.org/10.1016/j.actamat.2014.06.010.

[118] T.B. Yu, N. Hansen, X.X. Huang, Triple junction motion - A new recovery mechanism in metals deformed to large strains, Materials Science Forum 753 (2013) 485–488. https://doi.org/10.4028/www.scientific.net/MSF.753.485.

[119] T. Sakai, A. Belyakov, R. Kaibyshev, H. Miura, J.J. Jonas, Dynamic and post-dynamic recrystallization under hot, cold and severe plastic deformation conditions, Prog. Mater. Sci. 60 (2014) 130–207. https://doi.org/10.1016/j.pmatsci.2013.09.002.

[120] J.A. Hines, K.S. Vecchio, Recrystallization kinetics within adiabatic shear bands, Acta Mater. 45 (1997) 635–649. https://doi.org/10.1016/S1359-6454(96)00193-0.

[121] M.A. Meyers, Y.B. Xu, Q. Xue, M.T. Pérez-Prado, T.R. McNelley, Microstructural evolution in adiabatic shear localization in stainless steel, Acta Mater. 51 (2003) 1307–1325. https://doi.org/10.1016/S1359-6454(02)00526-8.

[122] M.E. Fitzpatrick, A.T. Fry, P. Holdway, F.A. Kandil, J. Shackleton, L. Suominen, Determination of residual stresses by X-ray diffraction., Teddington, 2005. https://eprintspublications.npl.co.uk/2391/.

[123] I. Noyan, J. Cohen, Residual Stress-Measurement by Diffraction and Interpretation, Springer-Verlag, 1987.

[124] R. Leach, Optical Measurement of Surface Topography, Springer, 2011.

[125] J.I. Goldstein, D.E. Newbury, P. Echlin, D.C. Joy, A. Romig, C.E. Lyman, C. Fiori, E. Lifshin, Scanning Electron Microscopy and X-Ray Microanalysis, Springer New York, NY, 1992. https://doi.org/https://doi.org/10.1007/978-1-4613-0491-3.

[126] R. Egerton, Physical Principles of Electron Microscopy-An Introduction to TEM, SEM, and AEM, 2nd ed., Springer Cham, 2016. https://doi.org/https://doi.org/10.1007/978-3-319-39877-8.

[127] L. Reimer, Scanning Electron Microscopy-Physics of Image Formation and Microanalysis, Springer Berlin, Heidelberg, 1998. https://doi.org/https://doi.org/10.1007/978-3-540-38967-5.

[128] I. Gutierrez-Urrutia, S. Zaefferer, D. Raabe, Coupling of electron channeling with EBSD: Toward the quantitative characterization of deformation structures in the sem, Jom 65 (2013) 1229–1236. https://doi.org/10.1007/s11837-013-0678-0.

[129] B.C. Carter, D.B. Williams, Transmission Electron Microscopy-Diffraction, Imaging, and Spectrometry, Springer Cham, 2016. https://doi.org/https://doi.org/10.1007/978-3-319-26651-0.

[130] M. Hugenschmidt, Scanning Transmission Electron Microscopy in a Scanning Electron Microscope : Electron-Beam Broadening , Contamination , and Investigation of ZIF-8 by Correlative Electron Microscopy, 2022.

[131] M.L. San Gabriel, C. Qiu, D. Yu, T. Yaguchi, J.Y. Howe, Simultaneous secondary electron microscopy in the scanning transmission electron microscope with applications for in situ studies, Microscopy 73 (2024) 169–183. https://doi.org/10.1093/jmicro/dfae007.

[132] J. Müller, B. Haas, W. Van den Broek, S. Shabih, C.T. Koch, Features of Our SEM Transmission Diffraction Sub-stage with 6-axis Sample Control and a Camera with Variable Camera Length, Microscopy and Microanalysis 26 (2020) 1906–1907. https://doi.org/10.1017/s1431927620019789.

[133] V. Morandi, P.G. Merli, Contrast and resolution versus specimen thickness in low energy scanning transmission electron microscopy, J. Appl. Phys. 101 (2007). https://doi.org/10.1063/1.2745333.

[134] A.J. Schwartz, M. Kumar, B.L. Adams, D.P. Field, Electron backscatter diffraction in materials science, Springer, 2009. https://scholar.google.com/scholar_lookup?title=Electron Backscatter Diffraction in Materials Science&author=A.J. Schwartz&publication_year=2010.

[135] M. Abbasi, D.I. Kim, H.U. Guim, M. Hosseini, H. Danesh-Manesh, M. Abbasi, Application of Transmitted Kikuchi Diffraction in Studying Nano-oxide and Ultrafine Metallic Grains, ACS Nano 9 (2015) 10991–11002. https://doi.org/10.1021/acsnano.5b04296.

[136] R.R. Keller, R.H. Geiss, Transmission EBSD from 10 nm domains in a scanning electron microscope, J. Microsc. 245 (2012) 245–251. https://doi.org/10.1111/j.1365-2818.2011.03566.x.

[137] P.W. Trimby, Orientation mapping of nanostructured materials using transmission Kikuchi diffraction in the scanning electron microscope, Ultramicroscopy 120 (2012) 16–24. https://doi.org/10.1016/j.ultramic.2012.06.004.

[138] G.C. Sneddon, P.W. Trimby, J.M. Cairney, Transmission Kikuchi diffraction in a scanning electron microscope: A review, Materials Science and Engineering R: Reports 110 (2016) 1–12. https://doi.org/10.1016/j.mser.2016.10.001.

[139] V. Bedekar, R. Shivpuri, A. Avishai, R.S. Hyde, Transmission Kikuchi Diffraction study of texture and orientation development in nanostructured hard turning layers, CIRP Ann. Manuf. Technol. 64 (2015) 73–76. https://doi.org/10.1016/j.cirp.2015.04.073.

[140] A. Avishai, K. Abbasi, D. Wang, N. Avishai, D. Wu, V. Bedekar, S. Hyde, S. Sitzman, A. Heuer, Tackling Characterization Challenges in High Deformation/Stress Steel Alloys Using Transmission Kikuchi Diffraction (TKD), Microscopy and Microanalysis 21 (2015) 2377–2378. https://doi.org/10.1017/s1431927615012660.

[141] K. Nikolic, V.M. Ferreira, L. Malet, T. Depover, K. Verbeken, R.H. Petrov, Uncovering the white etching area and crack formation mechanism in bearing steel, Mater. Charact. 197 (2023) 112659. https://doi.org/10.1016/j.matchar.2023.112659.

[142] P.W. Trimby, Y. Cao, Z. Chen, S. Han, K.J. Hemker, J. Lian, X. Liao, P. Rottmann, S. Samudrala, J. Sun, J.T. Wang, J. Wheeler, J.M. Cairney, Characterizing deformed ultrafine-grained and nanocrystalline materials using transmission Kikuchi diffraction in a scanning electron microscope, Acta Mater. 62 (2014) 69–80. https://doi.org/10.1016/j.actamat.2013.09.026.

[143] A. Winkelmann, B.M. Jablon, V.S. Tong, C. Trager-Cowan, K.P. Mingard, Improving EBSD precision by orientation refinement with full pattern matching, J. Microsc. 277 (2020) 79–92. https://doi.org/10.1111/jmi.12870.

[144] G. Nolze, M. Jürgens, J. Olbricht, A. Winkelmann, Improving the precision of orientation measurements from technical materials via EBSD pattern matching, Acta Mater. 159 (2018) 408–415. https://doi.org/10.1016/j.actamat.2018.08.028.

[145] G. Cios, A. Winkelmann, T. Tokarski, P. Bala, Pattern matching workflows for EBSD data analysis: Quartz chirality mapping, Mater. Charact. 224 (2025) 115076. https://doi.org/10.1016/j.matchar.2025.115076.

[146] J. Wu, E. Choo, L. Spasevski, Measuring nanograins of 50nm-thick metallization layer using a new approach of EBSD pattern matching, Proceedings of the International Symposium on the Physical and Failure Analysis of Integrated Circuits, IPFA 2023-July (2023) 1–5. https://doi.org/10.1109/IPFA58228.2023.10249056.

[147] B. Gault, M.P. Moody, J.M. Cairney, S.P. Ringer, Atom Probe Microscopy, Springer New York, NY, 2012. https://doi.org/https://doi.org/10.1007/978-1-4614-3436-8.

[148] M.K. Miller, Atom Probe Tomography-Analysis at the Atomic Level, Springer New York, NY, 2000. https://doi.org/https://doi.org/10.1007/978-1-4615-4281-0.

[149] M.K. Miller, R.G. Forbes, Atom-Probe Tomography-The Local Electrode Atom Probe, Springer New York, NY, 2014. https://doi.org/https://doi.org/10.1007/978-1-4899-7430-3.

[150] W.C. Oliver, G.M. Pharr, An improved technique for determining hardness and elastic modulus using load and displacement, J Mater Res 7 (1992) 1564–1583.

[151] M. Agmell, A. Ahadi, O. Gutnichenko, J.E. Ståhl, The influence of tool micro-geometry on stress distribution in turning operations of AISI 4140 by FE analysis, International Journal of Advanced Manufacturing Technology 89 (2017) 3109–3122. https://doi.org/10.1007/s00170-016-9296-7.

[152] D.Y. Jang, T.R. Watkins, K.J. Kozaczek, C.R. Hubbard, O.B. Cavin, Surface residual stresses in machined austenitic stainless steel, Wear 194 (1996) 168–173. https://doi.org/10.1016/0043-1648(95)06838-4.

[153] S. Kokkirala, U. Klement, J. Holmberg, H. Iwasaki, J. Manuel, B. Bermejo, S. Kimming, S.B. Hosseini, Understanding the development of mechanically and thermally induced white layers in AISI 52100 steel during hard turning : Process-microstructure-property relationship, Journal of Materials Research and Technology 38 (2025) 1185–1197. https://doi.org/10.1016/j.jmrt.2025.07.293.